MURDOCH
UNIVERSITY
PERTH, WESTERN AUSTRALIA

GROWTH AND CHARACTERIZATION OF SILICON NANOWIRES FOR SOLAR CELL APPLICATIONS

By

HANAA FLAYEH AL-TAAY

Thesis submitted in fulfillment of requirements for the degree of Doctor of Philosophy of
Murdoch University
2014

I declare that this thesis is my own account of my research and contains as its main content work which has not previously been submitted for degree at any tertiary education institution

Hanaa Flayeh Al-Taay

ABSTRACT

Silicon nanowires (SiNWs) have received considerable attention as base materials for third-generation photovoltaic (PV) devices because they lend themselves to large-scale production with enhanced light trapping and increased overall performance. Previous studies have grown SiNWs on indium tin oxide-coated glass substrates by the pulsed plasma-enhanced chemical vapour deposition method (PPECVD) using tin (Sn), aluminum (Al), gold (Au) and zinc (Zn) as catalysts.

Various catalysts (Sn, Zn, Au and Al) with thin film thicknesses from 10nm to 100nm, were used in this study of SiNW growth. Surface morphology analysis, by scanning electron microscopy (SEM) and transmission electron microscopy (TEM), of the grown SiNWs showed the influence of the catalyst type and thickness. The wires became thicker and shorter as the catalyst thickness increased. However, the SiNWs catalyzed by Al metal were thicker than those grown using Sn, Au and Zn metals. The density of the SiNWs decreased as the catalyst thickness increased. For example, the 10nm thick Al catalyst produced the greatest SiNW density of 20NW/μm^2, whereas the 100nm-thick Au resulted in the lowest density of 6NW/μm^2.

The effect of catalyst type and thickness on the structural properties of the grown SiNWs was investigated through X-ray diffraction (XRD). The XRD measurements showed that the SiNWs grown with Au catalysts had higher crystallinity than those grown using other catalysts. Moreover, the diffraction peaks became sharper with increasing wire diameter, indicating that the crystallinity of the grown SiNWs was enhanced. The optical properties of the prepared SiNWs were investigated by photoluminescence (PL) and Raman spectra. A red emission band was clearly observed in the PL spectra of all the prepared SiNWs. In the Raman spectrum, the first-order

transverse optical mode (1TO) was exhibited in all SiNWs catalyzed using Sn, Au, Al and Zn. However, the 1TO peak location depended on the catalyst type and thickness. Important results were observed at a catalyst thickness of 80nm for all catalysts because the 1TO Raman peak was closest to the crystalline Si peak location for all the prepared samples, except for the SiNWs prepared using 100nm of Au metal.

The crystal size of the grown SiNWs was calculated from the Raman spectra. In general, the crystal size of the grown SiNWs using 10, 20, 40, 60 and 100nm of Sn, Al and Zn metals decreased with increasing thickness of catalyst. However, the SiNWs prepared using 80nm thick Sn, Al and Zn catalysts had the largest crystal size. In contrast, the crystal size of SiNWs catalyzed by Au increased with increasing the catalyst thickness.

Several designs of solar cells based on SiNWs were fabricated by the PPECVD method at 400°C on an ITO-coated glass substrate using the two most promising catalysts, Zn and Au. The first one was a p-type SiNWs/i-amorphous Si/n-type amorphous Si (p-i-n) structure using the Zn catalyst. The photocurrent density of the fabricated device was 13.3mA/cm^2 and the open-circuit voltage was 0.5V. A high-performance nanowire solar cell fabricated in this work had 2.05% light conversion efficiency.

The other device structures were fabricated by doping SiNWs catalyzed with Zn and Au as p and n type to fabricate p-n homo-junction SiNW solar cells. The fabricated pn junction solar cell based on the Zn-catalyzed SiNWs showed a higher efficiency of 1.01% compared with the Au catalyzed SiNW solar cell with an efficiency of 0.67%. These promising results provide a basis for further studies aimed at optimizing the device designs.

DEDICATION

I would like to warmly dedicate this dissertation to my darling children whose love shines bright like beautiful candles upon my soul and sustains me…..

To my precious sister for all her support and encouragement and who has always been like a second mother to me……

To all those who continued to remember me in their prayers to make this PhD a success…….

Finally, to all those I love and all those who love me.

With appreciation and love.

Hanaa

ACKNOWLEDGEMENT

I would like to express my appreciation and sincerest words of thanks to my supervisor **Professor Philip Jennings** for his encouragement, kindness and motivation. It has been a great pleasure working with him. Who forever, is a source of knowledge and symbol of guidance for humanity as a whole. I want to give my deep gratitude to my co supervisor **Dr. David Parlevliet** for his guidance and support suggestions throughout the experimental and thesis works have contributed to the success of this research.

I am grateful to the support of the Government of Iraq for giving me this opportunity of PhD scholarship. Special and heartfelt thanks are extended to Dr Mazin Auny/University of Basrah for his support, guidance and encouragement throughout my research.

I would like to express my acknowledgements to all the staff members of the school of Engineering and Information Technology, Murdoch University. My appreciation to Mr Peter Fallon for his guidance with using the SEM at Murdoch University. Not forgotten, my acknowledgement also goes to all the staff of School of Physics / University Sains Malaysia/ Nano-Optoelectronics Research and Technology Laboratory (N.O.R) for their co-operation to do measurement.

My thank goes also to my friend Denise Smith and her family for supporting me through difficult times. Also, I would to thank the amazing woman Mrs Niki. I would additionally like to express my enormous gratitude to my family especially my sister for her constant and continuing emotional support at all times during my study. Finally, I thank my God, Who is entire source of knowledge and wisdom to mankind for provision, guidance, protection and grace.

TABLE OF CONTENTS

LIST OF FIGURES

LIST OF TABLES

LIST OF ABBREVIATIONS & ACRONYMS

Amorphous Silicon	**a-Si**
Crystalline Silicon	**c-Si**
Chemical Vapour Deposition	**CVD**
Current-voltage	**IV**
Current Density-Voltage	**JV**
Field Emission Scanning Electron Microscopy	**FESEM**
Hydrogenated Amorphous Silicon	**a-Si:H**
Hot Wire Chemical Vapour Deposition	**HWCVD**
Indium Tin Oxide	**ITO**
Molecular Beam Epitaxy	**MBE**
Microcrystalline Silicon	**µc-Si**
Nanocrystalline Silicon	**nc-Si**
Nanowire	**NW**
Plasma Enhanced Chemical Vapour Deposition	**PECVD**
Pulsed Plasma Enhanced Chemical Vapour Deposition	**PPECVD**
Quartz Crystal Microbalance	**QCM**
Radio Frequency	**RF**
Scanning Electron Microscope	**SEM**
Silane	**SiH_4**
Silicon Nanowire	**SiNW**
Solid Liquid Solid	**SLS**
Transmission Electron Microscope	**TEM**
Ultra High Vacuum	**UHV**
Vapour Liquid Solid	**VLS**
Very High Frequency Plasma Enhanced Chemical Vapour Deposition	**VHF-PECVD**

PUBLICATIONS

- ***H.F. Al-Taay***, M.A. Mahdi, D. Parlevliet , P.Jennings, *Controlling the diameter of silicon nanowires grown using a tin catalyst*, Materials Science in Semiconductor Processing 16 (2013) 15–22.

- ***H.F. Al-Taay***, M.A. Mahdi, D.Parlevliet, Z.Hassan, P.Jennings, *Preparation and characterization of silicon nanowires catalyzed by aluminium*, Physica E 48 (2013)21–28.

- ***H.F. Al-Taay***, M.A. Mahdi, D.Parlevliet, Z.Hassan, P.Jennings, *Structural and Optical Properties of Au-Catalyzed SiNWs Grown Using Pulsed Plasma-Enhanced Chemical Vapour Depositionm*, Superlattices and Microstructures, 61 (2013) 134–145.

- ***H.F. Al-Taay***, M.A. Mahdi, D. Parlevliet, P. Jennings, *Fabrication of Solar Cells- Based on Silicon Nanowires, Renewable Energy* (2013), under review.

- ***H.F. Al-Taay***, M.A.Mahdi, D.Parlevliet, Z.Hassan, P.Jennings, *Growth and Characterization of Silicon Nanowires Catalyzed by Zn Metal Via Pulsed Plasma- Enhanced Chemical Vapor Deposition*, Superlattices and Microstructures, 68 (2014) 90-100.

- ***H.F. Al-Taay***, M.A.Mahdi, D.Parlevliet, , P.Jennings, *The effect of catalyst type and thickness on the morphology and the optical properties of SiNW grown via PPECVD method*, International Conference on Physics and Engineering (ICPE), (2013)30-31/12.

CHAPTER 1

INTRODUCTION

1.1 Overview

There's plenty of room at the bottom," the famous lecturer Richard Feynman said in 1959 when he suggested the possibility of manipulating things at the atomic level (Feynman 1960). The real burst of nanotechnology did not come until the early 1990s and the discovery produced a paved way for the new and exciting field of nanoscience and nanotechnology. Furthermore, the increasing availability of methods for the synthesis of nanostructured materials and the tools for characterization contributed significantly to the breadth of this field.

Nano- materials have unique properties because of their nanometre sizes and are thus receiving considerable attention in nanotechnology applications. Moreover, the properties of such structures depend on their dimensionality, size and morphology, which are significantly different from their corresponding bulk counterparts (Koo 2006).

Nano-materials can be classified as zero-dimensional (0D), one-dimensional (1D), and two-dimensional (2D) materials depending on the quantum confinement (i.e., the number of nanoscale dimensions). Zero-dimensional (0D) structures have three nanoscale dimensions, such as nanoparticles, quantum dots, and so on. One-dimensional (1D) structures have two nanoscale dimensions, such as nanorods, nanobelts, nanowires, and so on. Two-dimensional 2D structures have one nanoscale dimension, such as nanosheets, nanowalls, nanoflowers, and nanocrystalline thin films (Xia et al. 2003).

In the past few decades, 1D nanomaterials including nanowires have attracted extraordinary attention, and as potential electronic components, because of their unique physical and chemical properties. Compared with conventional bulk phase or thin films, 1D nanomaterials have several unique advantages including high crystallinity, self-assembly, high surface-to-volume ratio, quantum confinement effects, as well as slow electron–hole recombination (Sattler 2011; David 2011). Given their fascinating properties, 1D nanostructures attract considerable attention and unique applications, especially in optoelectronic nanodevices (Chanda *et al.* 2009).

Nanowires offer new opportunities to explore the effects of surfaces, interfaces, strain, and quantum confinement on the properties of nanoscale materials, which are defined as structures with diameters of 100nm or less and lengths that are often in the tens of nanometres to tens of micrometres (Bhushan 2007).

Silicon (Si) is a common material and is the second most abundant element, exceeded only by oxygen. In addition, Si is nontoxic and makes up 25% of the Earth's crust, having an almost ideal band gap of 1.1eV, with long term stability (Gajovic *et al.* 2008). Thus, one of the most important 1D nanostructured materials is the Si nanowire (SiNW), which has unique physical properties, making it a popular choice for a variety of nanotechnology applications (Sato *et al.* 2012; Agarwa; *et al.* 2008; Kempa *et al.* 2008).

In 1960, the vapor–liquid–solid (VLS) mechanism of Si nanowire growth was proposed by Wagner and Ellis 1964. To date, this growth mechanism is the most common method for synthesizing SiNWs. Finding new alternative sources of energy has become urgent over the past few years for several reasons, including the foreseeable end of cheap oil supplies, the instability and sharply rising prices of fossil fuels (the price of crude oil has increased by a factor of 5 in the last few years), and the environmental pollution caused by burning oil (Jha 2010).

Global energy demand will more than double by 2050 and will triple by the end of the century. At the same time, an estimated 1.64 billion people, mostly in developing countries, are not yet connected to an electricity grid; thus renewable energy (RE) offers some hope for improving their quality of life (Jha 2010).

Among the REs available, solar power is arguably the most promising and probably the only one of the alternative fuels and nuclear sources that can provide our total energy needs. The average intensity of solar radiation that strikes the earth in one hour (4.3×10^{20} J) provides as much energy as we currently consume over an entire year (4.1×10^{20} J (~13 TW).

Covering 0.16% of the land on earth with 10% efficient solar conversion devices would provide 20TW of power (Lewies 2007). Solar electricity generation is now the fastest-growing electricity source, doubling its output every two years. The solar photovoltaic (PV) market has grown at an annual rate of about 50% over the past few years, growing to 3800 MW in 2007 from 2521 MW in 2006 (Mario *et al.* 2008).
Silicon solar cells are the most widely used PV technology because of the availability and relatively cheap price of the silicon, in addition to its desirable physical properties. However, the need for a large area to collect the solar energy is still one of the factors that constrain most users of solar energy. Using nanomaterials may possibly lead to higher efficiencies and lower cost designs of solar cells because of their high surface-to-volume ratio. However, the solar cell based on nanocrystalline materials could have low efficiencies due to increased carrier recombination at the surface.

Therefore, an enormous increase in interest in the development of thin film solar cell technologies has been observed in recent years and this is also known as the second generation of PV, It aims to transform the PV industry through cost reductions and increasing market penetration. The next stage in the nanotechnology revolution is the use of nanostructured materials to produce low cost, high yielding, and efficient solar

cells, known as the third-generation of PV cells (Sivakov *et al.* 2009). Nanostructured solar cells offer several advantages including the ability to improve on the single junction solar cell efficiency by implementing new concepts and the ability to overcome practical limitations in existing devices, such as tailoring the material properties of existing materials or using nanostructures to overcome constraints related to lattice matching. Moreover, there is also a potential for low cost solar cell structures using self-assembled nanostructures.

Producing high-efficiency and cheap solar cells has become an important goal of research. Therefore, SiNWs have acquired increasing attention for achieving the third generation solar cell, which would allow the reduction of device production and material costs, as well as for the development of the new generation of thin film Si solar cells with enhanced light trapping (Tsakalakos *et al.* 2007). Using Si nanowire array-based PV cells has great potential because of the proven track record of polycrystalline Si solar cells. In addition, Si nanowires have high absorbance of light because the band gap in SiNWs transforms from indirect into direct induced by the quantum confinement effect at the nanometre size (Feynman 1960; Honsberg *et al.* 2006).

Moreover, the optical band gap of SiNWs increases with the decrease in the wire diameter; thus, they are potentially more useful in optoelectronic applications than bulk Si (Ma *et al.* 2003). There are a number of advantages of applying SiNWs for fabricating solar cells. First is the quantum confinement effect. The optical band gap of bulk Si can be increased from an indirect band gap to a direct band gap as a result of dimensional confinement (Honsberg *et al.* 2006). The outcome of this process is to shift the photoresponse of Si closer to the maximum of the solar spectrum at the earth's surface, thereby improving the energy collection efficiency of the cell. Another advantage of SiNWs is that they are good absorbers of light; regular silicon is 20% to 40 % reflective, while SiNWs are only 4% reflective (Feynman 1960; Koo 2006).

1.2 Scope of the Study

Silicon nanowires were synthesized by the Pulsed Plasma Enhanced Chemical Vapor Deposition (PPECVD) method (Parlevliet 2008). Among the several growth mechanisms used to describe the synthesis of SiNWs, the VLS mechanism is the most widely used and gold is the most common metal used as a catalyst.

Cheaper alternative metals would be useful for producing similar densities of nanowires. Thus, different metal catalysts were tested in this project, such as aluminum, tin and zinc, in an attempt to improve the properties of the SiNWs for PV applications. The effects of the catalyst type and thickness on the morphological, structural, and optical properties of the grown SiNWs were also investigated.

Using SiNWs in PV devices has several advantages, including lower production costs, increased conversion efficiency, and good stability. Therefore, a new design was explored for producing PV devices using SiNWs to incorporate their novel properties into solar cells, thereby fabricating SiNW-based solar cells. Two structures of the solar cell were studied: the homojunction pn SiNWs and SiNWs/a-Si hybrids. The prepared solar cells were characterized and optimized.

1.3 Research Objectives

The overall Research Question was to determine whether the inclusion of suitable SiNWs in thin film solar cells could improve their efficiency and stability.

The current study aims to achieve the following:

1. Prepare SiNWs by the PPECVD process method.

2. Study the effect of metal catalyst type on the morphology, crystalline structure, and optical properties of the grown SiNWs.

3. Study the effect of metal catalyst thickness on the morphology, crystalline structure, and optical properties of the synthesized SiNWs.
4. Fabrication of hybrid SiNWs/a-Si solar cells and studying their characteristic.
5. Fabrication of homojunction *pn* SiNWs solar cells and studying their characteristic.

1.4 Outline of the Thesis

This thesis contains ten chapters. In Chapter 1, the general overview about the subject of the study has been provided. Chapter 2 contains the literature review about the growth of SiNWs catalyzed using different metals and various preparation parameters, as well as the fabrication of SiNW-based solar cell structures. This section also includes a theoretical background related to the study subject. Chapter 3 describes the methods used to fabricate, characterize and optimize the SiNWs and PV devices and the experimental techniques used to collect and analyze the properties of the grown SiNWs.

In Chapter 4, the effect of Sn catalyst layer thickness on the morphology, structural and optical properties of the prepared SiNWs is investigated. Varying thicknesses of Al catalyst are used to produce SiNWs and the physical properties of the grown SiNWs are discussed in Chapter 5. In Chapter 6, SiNWs were grown using varying thickness of Au metal as a catalyst and the surface morphology, crystalline structure and optical properties were studied. The preparation SiNWs catalyzed with different thickness of Zn and controlling the properties and diameter of SiNWs by controlling the thickness of the catalyst is reported in Chapter 7. Chapter 8 includes a comparison and discussion of the results of using different types and layer thicknesses of catalyst on the properties of the grown SiNWs. In Chapter 9, several prototype solar cell devices based on SiNWs are fabricated. The details of the design and characteristics of the devices are also discussed in this chapter. Chapter 10 includes the conclusions and suggestions for future work.

CHAPTER TWO

LITERATURE REVIEW AND THEORETICAL CONCEPTS

2.1 Introduction

This Chapter presents a literature review of the preparation of Si nanowires (SiNWs) catalyzed using different metal catalysts, as well as the various preparation parameters. A part of this section focuses on the fabrication of SiNW-based solar cells. Several theoretical backgrounds related to the study subject, such as the growth mechanism and techniques for the preparation of SiNWs, the properties of SiNWs, and the application of SiNWs are also discussed.

2.2 Preparation of SiNWs by PECVD and Pulsed PECVD methods

Hofmann *et al.* (2003) fabricated SiNWs via the PECVD method using silane (SiH_4) and gold (Au) as a catalyst under the following conditions: 13.6MHz of radio frequency (RF), temperature of 380°C, and pressures between 0.4 and 2.4mbar. They found that RF plasma significantly increased the growth rate without decreasing the crystallinity of the as-grown wire structures.

In addition, a microwave plasma reactor was used to synthesize single crystal SiNWs using SiH_4 with molten gallium (Ga) pools. The SiNWs grown under the conditions of 2% SiH_4/H_2, 40 torr of pressure, and 700W of plasma power consisted of a single crystalline NW grown along the <100> direction, with a diameter ranging from tens to hundreds of nanometres and a length ranging from tens to hundreds of micrometres (Sharma 2004). Iocopi *et al.* (2007) showed that the combined use of plasma enhancement with a low melting point catalyst, such as In, is a powerful method

for obtaining high yield growth of SiNWs. Very high frequency PECVD (VHF-PECVD) with 150MHz and 15W of power at a temperature range of 363°C to 230°C was used to carry out the SiNW growth. Notably, the SiNWs grew by the Vapour-Solid-Solid (VSS) mechanism at temperatures as low as 250°C, whereas no growth occurred when the temperature was around 230°C (Hamidinezhad *et al.* 2011).

Moreover, Rathi *et al.* (2011) noted that using plasma treatment to grow SiNWs by the PECVD method, with Sn as catalyst, can reduce the oxide layer on the Sn surface. The 20W of plasma power at 13.56MHz and temperatures ranging from 300°C to 400°C were applied to grow the SiNWs. Axial and radial growth rates were controllable through hydrogen dilution of the plasma which affects the concentration of the SiH_4 radicals in the plasma.

Garozzo *et al.* (2013) synthesized SiNWs by PECVD using SiH_4 as the Si gas source at 380°C. They investigated both 1D uncatalyzed and 2D catalyzed SiNWs by fixing the chamber pressure and changing the plasma power. They found that the growth rate of NWs depended on the plasma power, with a maximum at about 20W. A modification of the PECVD method is known as the pulsed PECVD (PPECVD).

Parlevliet (2008) determined the affect of using pulsed PECVD in the range of modulation frequencies. He noted that using the pulsed plasma with different modulation frequencies led to improve growth of SiNWs at low deposition temperature. Also, the average NWs density and the rate of deposition of the amorphous silicon (Si) layer both increased as the plasma modulation frequency increased towards 1000HZ. The PPECVD technique increased the deposition rate of a-Si, µc-Si, and nc-Si, while suppressing the dust formation that tended to occur when the deposition rate was increased by increasing the plasma power (Das *et al.* 2003).

2.3 Catalysts Used to Grow SiNWs

SiNWs grown by the vapor-liquid-solid (VLS) mechanism require the use of catalysts to increase the growth rate. Various types of catalysts have been used to grow SiNWs by the VLS mechanism, such as Ga, which has been used to grow SiNWs by the PECVD method (Boj 2010). Sharma and Sunkara (2004) synthesized single crystal SiNWs using large pools of molten Ga and a microwave plasma containing SiH_4 gas. Indium (In) has also been used to catalyze SiNWs using hydrogen radical treatment at a temperature of 400°C (Jeon and Kamisako 2008).

Copper (Cu) is another catalyst that has been used to synthesize SiNWs by the VLS mechanism using the CVD method (Demichel 2009). Titanium (Ti) has been used as a catalyst to grow SiNWs; however, the NW growth mechanism differs from the usual VLS mechanism, which depends on the eutectic temperature of Ti/Si (Kamins *et al.* 2000; Sharma *et al.* 2004). Iron (Fe) has also been used to catalyze SiNWs by laser ablation (Fukata 2005).

Moreover, gold (Au), tin (Sn), aluminum (Al) and zinc (Zn) have been used as catalysts to grow SiNWs. However, Au is the most common catalyst for the synthesis of SiNWs because of its advantages, such as a low temperature eutectic point with Si (363°C), it does not form silicate, and its resistance to oxidation in air (Hofmann *et al.* 2003). SiNWs can be synthesized using Au a as catalyst at lower temperatures than the Au–Si eutectic temperature by VHF-PECVD (Hamidinezhad *et al.* 2011).

Cui *et al.* (2001) prepared SiNWs by exploiting well-defined Au nanoclusters as the catalyst. They found that the Au catalyst thickness can control the growth of the NWs, indicating that the diameter distribution of the SiNWs mirrors that of the catalysts. Ho *et al.* (2012) grew vertically aligned SiNWs by HW-CVD using an Au catalyst. Au–Si alloy nanoparticles were formed by annealing the Au-coated Si

substrate in H_2 at 650°C. Then, ramp cooled precipitate epitaxial Si seeds were formed by the liquid phase epitaxy (LPE) mechansim and later the substrate was heated to 850^{o}C in $SiCl_4/H_2$ to grow the SiNWs. Meanwhile, Sn is a promising metal catalyst candidate for low-temperature synthesis because the Sn–Si alloy has a low eutectic temperature.

The low eutectic temperature provides new opportunities to lower the growth temperature of SiNWs produced by the VLS mechanism, which would also be favorable for device fabrication (Jeon and Kamisako 2008; Yu *et al.* 2009). In addition, Sn-catalyzed SiNWs, by a hydrogen radical assisted deposition method, were examined for solar cell application (Jeon and Kamisako 2010).

Meshram *et al.* (2013) formed the Sn catalyst by hot wire atomic hydrogen treatment of a 300nm thick Sn film in a thermal evaporator. They synthesized SiNWs by HW-CVD at a temperature range of 300°C to 400°C, and found that the diameters and lengths of the NWs depend on the Sn thickness and the growth time, respectively.

Recently, the use of Al as a catalyst for growing SiNWs has attracted significant attention. However, using Al as a catalyst has been found to be more challenging because of the reactivity of Al with O_2 and H_2O that leads to the formation an oxide layer (Wacaser *et al.* 2009). Moreover, Al metal can dope Si to form an acceptor level in the Si band gap; thus, using Al as a catalyst is promising for obtaining a p-type SiNW (Sze 2007b).

Wacaser *et al.* (2009) showed that although the Al temperature is below the Al/Si eutectic temperature, SiNW growth occurs with a super cooled liquid droplet by the VLS mechanism through ultra-high vacuum CVD. They also showed the effect of varying the Al layer thickness, which clearly influences the average diameters of the grown NWs.

Wang and co-workers (2006) used Al as a catalyst to grow SiNWs on Si(111) at temperatures ranging from 430°C to 490°C, which is lower than the eutectic temperature in the VSS mechanism. In addition, Ke *et al.* (2009) demonstrated that the Al-catalyzed growth of SiNWs is a promising approach for obtaining a high aspect ratio with a single crystal, p-type as-grown SiNWs for photovoltaic applications.

Moreover, several reports have been published on the use of zinc metal as a catalyst to grow SiNWs. Zn has been shown to be an effective catalyst material. Thus, Yu *et al.* (2000) and Chung *et al.* (2000) synthesized SiNWs using CVD, and demonstrated VLS SiNWs grown by the CVD process using SiH_4 at a partial pressure of 6.7mbar and temperatures between 440 and 500°C.

The Zn catalyst was created by the deposition of $ZnCl_2$/ethanol solution on a Si substrate and heating the substrate at 450°C. They obtained SiNWs with diameters between 15 and 35nm. The SiNW synthesis by the gas-phase reaction of $SiCl_4$ with Zn at 1000°C resulted in SiNWs with diameters ranging from 40nm to 80nm. Zn metal was likewise observed at the end of the NWs, indicating that SiNWs could be grown by the VLS mechanism (Uesawa *et al.* 2010).

2.4 Fabrication of Solar Cells based on SiNWs

The PPCVD method was used to produce SiNW-based photovoltaic devices, with a 13.56MHz RF source used to generate a 35W plasma and a modulation frequency of 1000Hz under 3torr (Parlevliet and Jennings 2011). A new doping process has been developed for fabricating low cost SiNW-based solar cells, which includes using a sol-gel method with phosphorus pentoxide (P_2O_5), combined with a screen printing method for the fabrication of electrodes. The photovoltaic characteristics showed good performance, which could be suitable for low cost, high efficiency solar cell, based on SiNWs (Huang et al. 2012).

Kumar *et al.* (2011) fabricated solar cells with highly improved antireflection properties and a n+-p-p+ structure, based on SiNW arrays, by a wet chemical etching process. Various substrates have been used to fabricate solar cells based on SiNWs. Odomell *et al*. (2011) used glass as a substrate to synthesize radial p-i-n junctions of intrinsic and n-type hydrogenated a-Si over p-type SiNWs by the PECVD method, with an efficiency of about 5.6%.

In addition, SiNW arrays have been produced on glass substrates by a wet etching process of microcrystalline p-/n-/n+ Si. The fabricated cells presented low reflectance and strong broadband optical absorption, and showed good performance as a PV material, with efficiencies of up to 4.4% (Sivakov *et al.* 2009). Yu and co-workers (2010) produced a SiNW-based thin film solar cell on a TCO/glass substrate by the PECVD method. Solar cells based on SiNWs have enhanced light trapping properties, exhibiting strong light trapping absorption effects because of the structures of the SiNWs.

Cho *et al*. (2013) also used a glass substrate covered with ZnO:Al to grow radial junction SiNW solar cell (pin) structure by the PECVD method. For the p-type SiNWs covered with intrinsic and n- type hydrogenated amorphous Si, the solar cells showed 4.9% efficiency, V_{oc} = 0.8V, and J_{sc} = 12.4mA/cm^2.

Single crystal Si wafers have been used as a substrate to synthesize SiNWs with a Sn catalyst by a hydrogen radical assisted deposition method. The structure of the synthesized SiNWs cells showed potential for photovoltaic applications (Jeon and Kamisako 2009). Fang *et al.* (2008) fabricated slanting-aligned SiNW arrays on a Si(111) substrate using wet chemical etching with dry metal deposition, and employed the prepared SiNW arrays in solar cell applications with high efficiency. Moreover, p-n junction SiNW solar cells on a metal foil substrate, fabricated by the CVD method exhibited an efficiency of 0.1%. They also found that the optical reflectance of the SiNW solar cells were reduced by one to two orders of magnitude compared with planar cells (Tsakalakos *et al.* 2007).

Investigations on PV properties at the single nanowire (NW) level could permit the determination of the intrinsic limits and potential benefits of nanoscaled devices and reveal the present flaws that require further improvement. Tian *et al.* (2007) synthesized individual coaxial p-type/intrinsic/n-type SiNWs with efficiencies up to 3.4%. The output of these devices can be increased either by increasing the light intensity or by using several coupled elements. Moreover, Yoo *et al.* (2013) demonstrated single crystalline doped and undoped Si radial p-n and p-i-n junctions grown on vertical SiNWs by low pressure CVD with J_{sc} of 40 mA/cm^2 and efficiency of 10%. Recently, the realization of a single NW tandem solar cell has been described, which is basically an axial p-i-n+–p+-i-n Si heterostructure. The device showed an average increase of 57% in its open-circuit voltage compared with the single p-i-n device.

The V_{oc} values of the single p-i-n radial and axial heterostructures were similar despite the very different diode junction geometries. This finding is most striking in comparison with the p-i-n axial versus coaxial Si (Kempa *et al*. 2008). Xie *et al*. (2012) used the PECVD method to produce radial n-i-p structure SiNW-based μc-Si:H thin film solar cells on stainless steel foil. Their cells initially showed a V_{oc} of 0.37V, J_{sc} of 13.36mA/cm^2, and an efficiency of 1.48%, which improved to 0.48V, 13.42mA/cm^2, and 2.25%, respectively, after acid treatment.

2.5 Mechanisms of SiNW Growth

Several physical and chemical methods are available for fabricating SiNWs, which depend on various mechanisms, such as super critical vapour-liquid-solid, oxide assisted growth, and metal assisted chemical etching (Holmes *et al.* 2000; Heitsch *et al.* 2008; *Shi et al.* 2000; Smith *et al.* 2013). The VLS mechanism offers the concrete possibility of SiNW growth, with controlled diameter, density, length, position, and doping characteristics, as well as the mass production of SiNWs for device applications (Peng *et al.* 2013).

2.5.1 VLS Mechanism

This mechanism is commonly used to grow 1D semiconductor. It was first described by Wagner and Ellis in the 1960s for growing Si whiskers. VLS is still the most popular synthesis technique for growing NWs. The validity range of this mechanism is astonishingly broad because wires with diameters from a few nanometres up to a few hundred micrometres can be synthesized.

The growth process of Si wires by the VLS mechanism consists of three steps. First is the adsorption and cracking of the gaseous Si precursor, providing atomic Si for the growth, followed by the incorporation of Si atoms into the droplet. Second is the diffusion of the Si atoms through the droplet.

Third is the condensation of Si onto the Si wire at the liquid–solid interface. The properties of the droplet surface play an important role for the unidirectionality of the Si wire growth in the VLS growth mechanism (Westwater *et al.* 1998). When Au was deposited on the Si substrate, and then heated to temperatures above 363°C, small liquid Au–Si alloy droplets were formed on the substrate surface. Gaseous Si precursors, such as silicon tetrachloride ($SiCl_4$) or silane (SiH_4), will crack on the surface of the Au–Si alloy droplets, whereupon Si is incorporated into the droplet. The Si supply from the gas phase causes the droplet to become supersaturated with Si until it freezes out at the Si/droplet interface, as shown in Figure. 2.1.

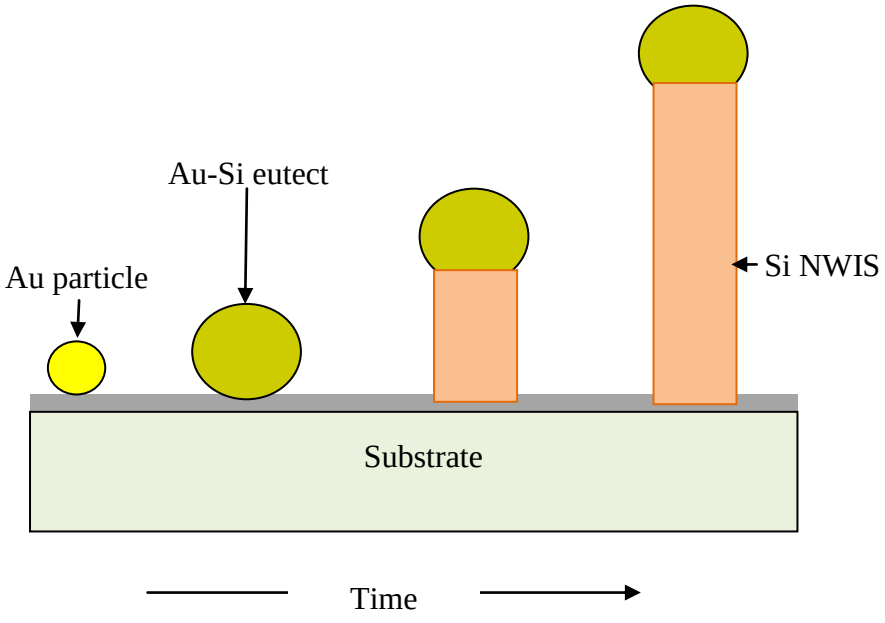

Figure 2.1: VLS of SiNWs with Au catalyst

Figure 2.2 shows the minimum temperature of certain metals required for the VLS growth of SiNWs and the respective impurity level energies in Si. The Figure shows that Ga metal had the lowest temperature required to grow SiNWs, while Ti had the highest. The nucleation, growth, oxidation, wire diameter, and position of the SiNWs grown by the VLS process with a Au catalyst, using SiH_4 as the Si gas source, have been determined by (Westwater *et al.* 1998).

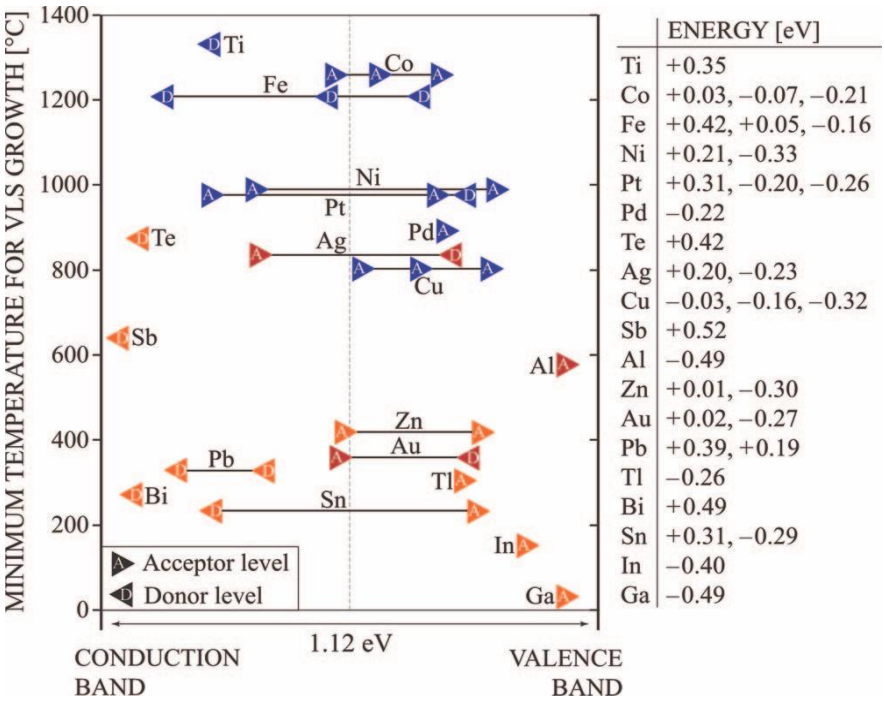

Figure 2.2: Minimum temperature of certain metals required for VLS growth of Si nanowires plotted versus their respective impurity level energies in Si. The energies of these impurity levels are given on the RHS with respect to the middle of the Si band gap (Schmidt *et al*. 2010).

2.5.2 VSS Mechanism

The growth of SiNWs can be carried out by a VSS mechanism rather than VLS when the growth temperature is less than the metal-Si eutectic point in the CVD (Wang et al. 2006). In the VSS mechanism, a solid catalyst particle instead of a liquid droplet is involved. The VSS mechanism is more likely to take place at lower temperatures (<363°C) **(**Falk *et al.* 2007; Zhang *et al.* 2007a; Li 2009)**.**

Figure 2.3 shows a schematic of the VSS mechanism for the growth of tapered NWs. First, SiH_4 species are decomposed and transferred to the Si substrate. The growth of the SiNWs below the nominal decomposition temperatures is possible because solid and liquid metal particles accelerate the decomposition of SiH_4. At the next step, the Si atoms are delivered to the growth interface by bulk or surface diffusion. Finally, the inclusion of atoms at the interface is preferred in VSS growth, as shown in Figure 2.3C (Wacaser *et al.* 2009). In the VSS mechanism, the catalyst remains solid as a spherical cap at the top of the wires during the growth of NWs, and then increases the adsorption and decomposition of the precursor gas (Molnar *et al.* 2013).

In contrast to the VLS growth mechanism, the growth through the VSS mechanism consumes more energy due to the diffusion of Si atoms into the NW through a solid catalyst. The precipitation of Si in the solid Au is much slower than in the liquid. Other catalysts, such as Cu and nickel, are used to grow SiNWs by the VSS mechanism. Other authors found that the mechanism of growth temperature was lower than the eutectic temperature Cu/Si and Ni/Si, so the size of the catalyst was still large to produce a massive drop in the melting temperature (Arbiol *et al.* 2007; Molnar *et al.* 2013). The NW growth rate by the VSS process is much slower because the rate of precipitation of the supersaturated Si in the solid Au catalyst is much lower than the rate in the liquid one (Hamidinezhad *et al.* 2011).

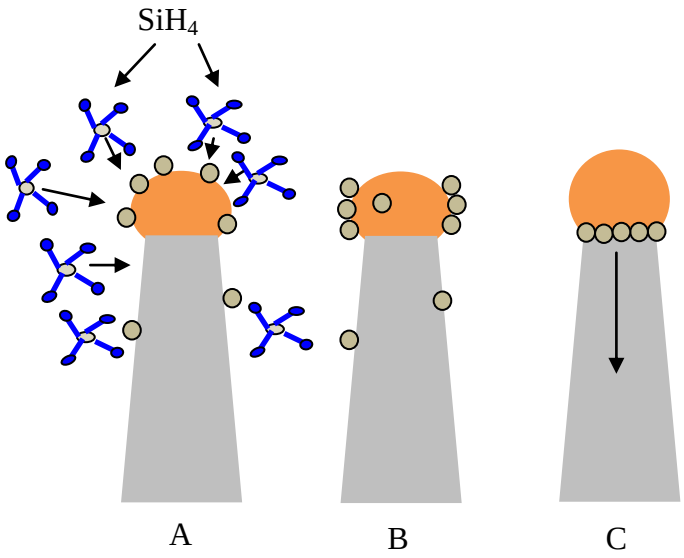

Figure 2.3: The process steps of the VSS mechanism of the NWs growth. (after Hamidinezhad et al. 2011).

2.6 Catalyst Effect on the NW Morphology

Catalyst type has an important role in the control of NW properties, including surface morphology, crystallinity, and the carrier concentration of the SiNWs. The effect of the catalyst is caused by the value of the eutectic point of the catalyst with Si, which can determine the most suitable temperature required to synthesize SiNWs by the VLS process.

One of the important things that is controlled by the catalyst type is the size of the nanoparticles and the wire diameter. The NW diameter is important for determining the growth direction, which affects the NW morphology. Thus, the diameter of the catalyst droplet determines the size of the wires produced (Wacaser *et al.* 2009). The SiNW properties are strongly size-dependent, in which NWs with larger diameters have properties that tend to approximate those of bulk Si (Schell *et al.* 2005).

The choice of catalyst depends on the type of NW that is to be produced, where the material to be used must be soluble in the catalyst (Mcllroy *et al.* 2004). Various types of metal catalyst have been used to grow SiNWs.

According to the study of Schmidt *et al*. (2009) the catalysts can be classified into three groups corresponding to the metal-Si phase diagram, as shown in the Figure 2.4. The phase diagram for group A, comprised of Au and Al, is dominated by a eutectic point at a Si concentration greater than 10%, and no metal-silicide phase is present.

Group B includes catalysts, such as Sn and In metals. The phase diagram for this group is dominated by a eutectic point at a low Si concentration (<1%), with the absence of silicide phases. The phase diagram for group C includes catalysts, such as Ti and Cu, and is characterized by the presence of one or more silicide phases with eutectic points at temperatures higher than 800°C. Each catalyst presents a different phase diagram, so their use should result in different growth phenomena and NW morphologies (Schmidt *et al*. 2010).

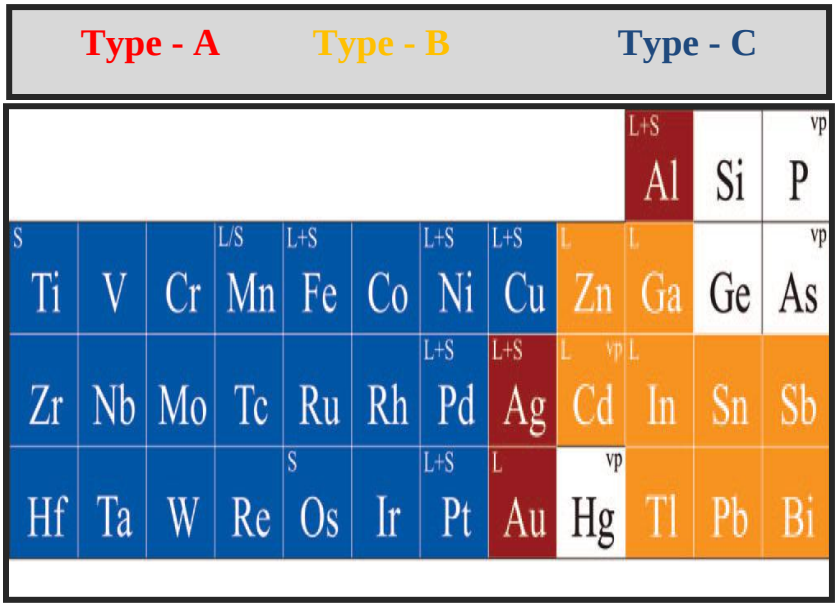

Figure 2.4: The periodic table classified according to the metal/Si phase diagram (Schmidt *et al.* 2010)

2.7 Growth Techniques

Different methods can be used to grow SiNWs. The properties of the grown wires (morphology, crystalline structure, optical, electrical, and so on) depend on the method of the growth. The various growth methods for preparing SiNWs are quite distinct in their characteristics, and the question of which method is most suitable depends, to a large extent, on the application.

2.7.1 Molecular Beam Epitaxy (MBE)

In MBE, a solid high-purity Si source is heated until Si starts to evaporate. A directional gaseous beam of Si atoms is aimed at the substrate, in which the atoms are adsorbed and crystallized. To reduce contamination, the base pressure of an MBE system is usually kept at ultrahigh vacuum, allowing for the monitoring of growth using reflection high-energy electron diffraction or other surface sensitive examination methods. MBE was initially designed for epitaxial layer-by-layer deposition only.

In MBE, two Si fluxes govern wire growth. First, the direct flux of Si from the Si source; and second, the flux of diffusing Si atoms from the Si substrate surface (Schemidt *et al*. 2010; Schemidt *et al.* 2009). MBE is a type of epitaxial growth, where the film and the substrate share the same or closely related orientations. This process requires a slow deposition rate, and thus an ultrahigh-vacuum environment. In a typical solid source MBE system, the target, such as Si, is heated in a separate cell until sublimation occurs. The vapour is then introduced into the main deposition chamber, and condenses on the substrate. Given the requirement for an ultrahigh vacuum and ultraclean substrate surface, the equipment system is usually very complicated and the deposition rate is very slow. However, the films deposited by MBE are usually high quality epitaxial films on single crystal substrates (Guo and Tan 2009).

The major difference between MBE and other epitaxial growth techniques stems from the fact that the growth is carried out in an ultrahigh vacuum environment. Therefore, the growth occurs far from thermodynamic equilibrium conditions, and is mainly governed by the kinetics of the surface processes. This finding is in contrast to the other growth techniques. Other advantages of MBE over other epitaxial growth techniques include excellent thickness control and low growth temperatures. Despite its technological advantages, MBE suffers from the high costs associated with maintaining the ultrahigh vacuum environment (Steiner 2004).

2.7.2 Thermal Evaporation Method (TE)

The thermal evaporation technique was developed by Lee *et al.* (2009), and has attracted much attention recently due to its advantages, as a low cost, simple, and effective method for preparing SiNWs (Zhao 2004). In thermal evaporation, the Si source is placed in quartz or alumina tube under high temperature. Thus various sources can be used for growing SiNWs, including Si powder mixed with Fe powder and hot pressed at around 1200°C (Yu *et al.* 1998).

Si powder and AuPd catalysts were used to grow SiNWs on Si(111) substrate at temperatures in the range of 800°C to 1000°C (Mohd *et al.* 2009). In addition, using this method can lead to the growth of SiNWs in the absence of a catalyst under high temperature (Pan *et al*. 2005; Qin *et al.* 2011). Another advantage of this technique is that the Si substrate can be used as a Si source to grow SiNWs using a catalyst, such as Ni or Au (Xing *et al.* 2002; Wong *et al.* 2005).

2.7.3 Laser Ablation (LA)

A high-power pulsed laser ablates material from a mixed Si–catalyst target, which is placed in a tube furnace held at high temperatures and purged with an inert gas.

The Si material ablated from the target cools by colliding with inert-gas molecules, and the atoms condense to form liquid nanodroplets with the same composition as the target. Thus, these nanoparticles contain both Si and the catalyst material.

According to the VLS mechanism, the SiNWs start to grow when the catalyst gets supersaturated with Si, and proceed as long as the catalyst nanoparticles remain liquid. This method does not need a substrate, and the composition of the grown NWs can be varied by changing the composition of the laser target (Schmidt *et al*. 2010; Schmidt *et al.* 2009). This method has been utilized for the deposition of films and nanoparticles, which involves laser ablation of a solid target, where the ablated material can be deposited on a substrate. Alternatively, the ablated material can be mixed with a reactive gas to make the appropriate material, and then carried by an inert gas through a nozzle into a vacuum chamber to produce a molecular beam, which is then deposited on a substrate with controlled temperature (Prasad 2004).

In this method, a laser source is focused to ablate onto the target which contains Si and a metal catalyst. This method is not common for the synthesis of NWs, with only a few research groups using it. The synthesized SiNWs exhibit different morphological characteristics, such curved, kinked, straight, and coiled shapes (Zhou *et al.* 1999). The use of various ambient gases, such as H_2, He and N_2, has a significant effect on the diameter of SiNW growth by laser ablation (Zhang 1999).

2.7.4 Chemical Vapor Deposition (CVD)

The industrial exploitation of CVD can be traced back to a patent by de Lodyguine in 1893 who had deposited W onto carbon lamp filaments through the reduction of WCl_6 by H_2 (Choy 2003). In CVD, a volatile gaseous Si precursor, such as SiH_4 or $SiCl_4$, is used as the Si source. Originally, CVD was devised for the deposition

of high-purity films. Verisons of CVD methods exist, which can be classified by parameters, such as the base and operation pressure or the treatment of the precursor.

Si oxidizes rapidly when exposed to oxygen at elevated temperatures; therefore, reducing the oxygen background pressure is critical to be able to epitaxially grow uniform SiNWs. In any case, it is useful to lower the base pressure of the CVD reactor down to high or even ultrahigh vacuum, which reduces unwanted contamination and enables growth at lowered temperatures. The pressure during growth depends mainly upon the gaseous Si precursor and its cracking probability at the catalyst surface.

The morphology and other properties of the nanowires grown by CVD method can be modified. CVD offers the opportunity of a controlled doping by intentionally introducing doping precursors. Doping profiles in the axial direction can be created by switching the doping precursors. One of the major problems of SiNWs grown by CVD is that they exhibit a certain variation in the growth direction, especially for diameters smaller than 50nm (Schmidt *et al*. 2010; Schmidt *et al.* 2009). CVD involves a chemical reaction at the substrate surface to form the thin film. The distinctive advantages of CVD outweigh its limitations.

In general, CVD is a versatile deposition technique, and has become one of the main processing methods for the deposition of amorphous, single-crystalline, polycrystalline thin films, and coatings for a wide range of applications (Choy 2003). The deposition rate of a CVD process is controlled by the slowest step in this serial process and is mainly determined by the competition between the mass transportation and the surface reaction rate. Mass transportation is usually a function of gas flow and its partial pressure. Therefore, this process can be increased by increasing the supply of the reactant such as gas or liquid precursor, thereby increasing the deposition rate (Guo and Tan 2009).

CVD is a widely used method for growing SiNWs using various gaseous sources silicon, such as silane (SiH_4) (Yu D.P et al. 1998), disilane (Si_2H_6) (Hannon 2006), and silicon tetrachloride ($SiCl_4$) (Usman 2013) . Moreover, using a mixture of high H_2 and SiH_4 partial pressures to epitaxial SiNWs by CVD method could led to show to be effective to reduce the NW nucleation and enabling growth of high aspect ratio (Ke 2009).

2.7.5 Plasma-Enhanced Chemical Vapor Deposition (PECVD)

In PECVD, as in the CVD processes, the reaction precursors are fed into the reactor in the form of gases. Plasma is produced in the reaction zone to activate the precursors. The substrate can be deposited either in or outside the plasma zone to enhance or avoid some plasma effects such as ion bombardment. PECVD can operate in a broad range of temperatures and pressure conditions, allowing for more freedom in preparation and proper control (Steiner 2004). By modifying the precursor prior to a reaction with the sample surface, the temperature of the substrate can be lowered. In cases where the thermal load is critical or where a high supersaturation of the droplet is necessary, NW growth can be enhanced using PECVD.

Moreover, in the PECVD process, the precursor gas is dissociated by the plasma into highly active radicals, which can be moderated for SiNW growth (Yu *et al.* 2008). In this method, DC or RF plasma is used in the CVD reactor. The plasma will help break down the precursors before they reach the substrate surface, significantly decreasing the surface temperature required for chemical reactions. However, high vacuum is required to ignite the plasma (Guo and Tan 2009). The properties of the thin films deposited by this technique depend on various parameters, such as electrode configuration, power, frequency, gas composition, pressure, flow rate, and substrate

temperature, and this technique is used to produce the amorphous and nanocrystalline Si thin films (Steiner 2004).

The RF plasma density is an important parameter that can affect the growth process and the surface morphology of the produced NWs. Thus, increasing RF power resulted in increased dissociation of SiH_4 gas into reactive species, whereas higher RF power might deactivate the catalytic effect (Chong *et al.* 2011).

2.8 Band Structure in Semiconductors

The bonding between atoms in semiconductors is usually covalent or ionic bonding. The energy band structures are formed when the atoms are periodically arranged in semiconductor crystals (Fukuda 1999). The valence and conduction electrons interact with the atoms in crystalline semiconductors, and this interaction slightly shifts the separate energy levels of the electrons to create different energies with different levels corresponding to the total atomic numbers in the crystal (Fukuda 1999). Figure 2.5 illustrates the band gap diagram in crystalline semiconductors.

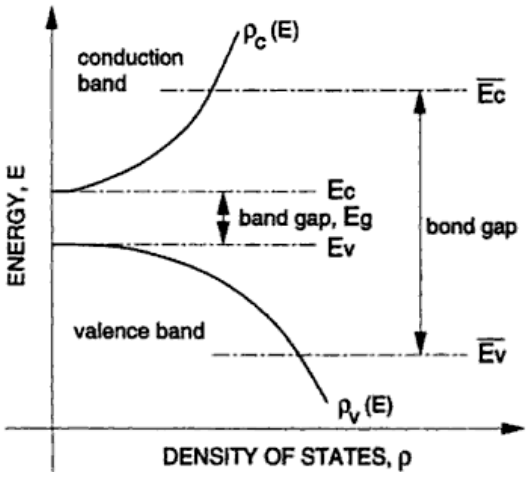

Figure 2.5: Valence band, conduction band and energy band gaps in the crystalline semiconductors (Fukuda 1999).

Where E_C and $\overline{E_C}$ are the edge and mean values of the conduction band, and E_V and $\overline{E_V}$ are the edge and mean values of the valence band, respectively. The energy band gap E_g is given by:

$$E_g = E_C - E_V \tag{2.1}$$

Semiconductors can be categorized into two types, namely, those with direct and indirect energy band gaps. In semiconductors with direct band gaps, the electron can transfer from the valence band to the conduction band when it absorbs energy equal to or exceeding E_g, whereas the valence electron in the indirect band gap cannot transfer to the conduction band without phonon assistance, as shown in Figure. 2.6 (Fukuda1999; Zhang 2009).

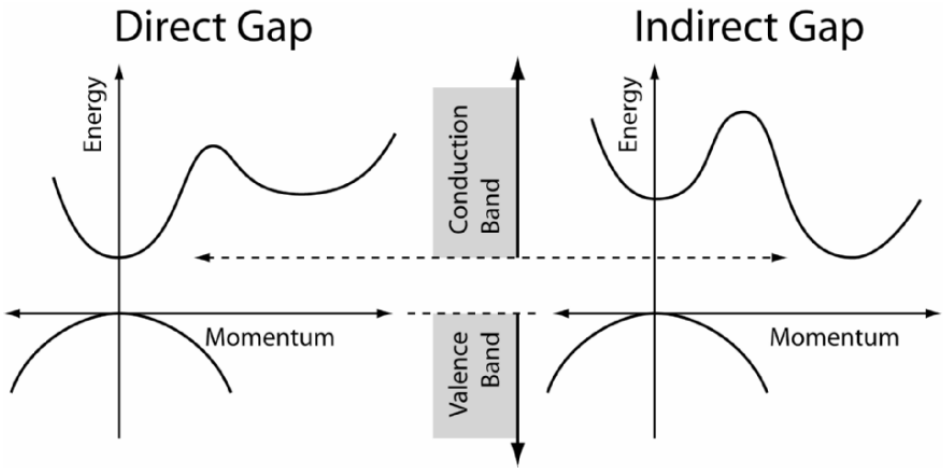

Figure 2.6: A schematic of the difference between a direct gap and an indirect gap Semiconductor (Rockett 2008).

The valence and conduction bands contain energy levels that can be filled by electrons or holes. The number of these allowed states per unit of energy is referred to as the density of states (DOS), which is given (for the electron in the conduction band) by the free electron formula as:

$$N(E) = \frac{1}{2\pi^2 h^3}\left(2m_e^*\right)^{3/2}\left(E - E_g\right)^{1/2} \tag{2.2}$$

DOS for the holes in E_V is expressed by the formula:

$$N(E) = \frac{1}{2\pi^2 h^3}\left(2m_h^*\right)^{3/2}\left(E\right)^{1/2} , \tag{2.3}$$

where $N(E)$ is the DOS at energy E; m_e^*, m_h^* is electron effective mass, and h is Planck's constant. The probability of electrons occupying a particular electronic state in the conduction band is given by the Fermi- dirac formula (Zhang 2009):

$$f(E) = \frac{1}{\exp\dfrac{\left(E - E_F\right)}{kT} + 1} , \tag{2.4}$$

where E_F is the Fermi energy, k is Boltzmann's constant, T is the absolute temperature and $f(E)$ represents the probability of finding the electron at energy E. The probability of holes occupying an electronic state in the valence band is given by:

$$1 - f(E) = \frac{1}{\exp\dfrac{\left(E_F - E\right)}{kT} + 1} \tag{2.5}$$

Semiconductors have several optical absorption processes, such as fundamental absorption, free carrier absorption, and absorption by the energy levels in the band gap (Fukuda 1999). Fundamental absorption occurs when the semiconductor is illuminated by light with higher energy than the band gap, thereby exciting the electrons in the valence band into the conduction band, and holes are formed. Furthermore, other absorption types occur because of the presence of impurities inside the band gap. In the absorption process, the electrons transfer to another level of impurity, from a donor level to the conduction band, from the valence band to the acceptor level, and so on.

The absorption coefficient (α) is given by the formula (Tarey and Raju 1985):

$$\alpha = \frac{1}{d}\ln\left(\frac{1}{T}\right), \tag{2.6}$$

where d is the sample thickness and T is the light transmission coefficient. The optical band gaps E_g of direct and indirect semiconductors can be estimated by using the following relationships:

$$\alpha = A\left(h\nu - E_g\right)^{1/2} \tag{2.7}$$

$$\alpha = B\left(h\nu - E_g \pm E_{phonon}\right)^2, \tag{2.8}$$

where ***A*** and ***B*** are constants, $h\nu$ is the energy of the illuminating photon, and E_{phonon} is the phonon energy. For the direct band gap, E_g, which can be calculated from the linear portion of the curve, is extrapolated to $(\alpha h\upsilon)^2=0$ when $(\alpha h\upsilon)^2$ is plotted as a function of $h\upsilon$. Figure 2.7 shows the absorption processes in direct and indirect semiconductors.

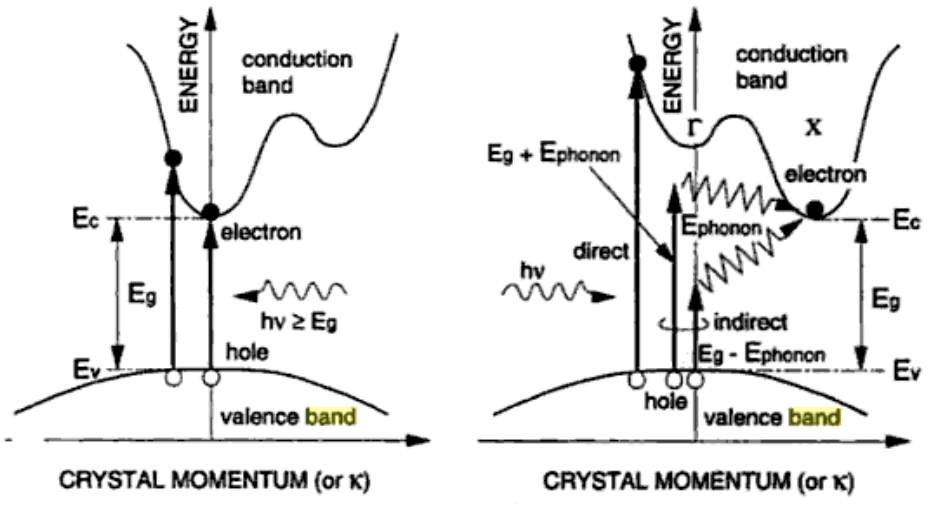

(a) (b)

Figure 2.7: (a) Absorption in direct band gap semiconductors, and (b) absorption in indirect band gap semiconductors (Fukuda 1999).

2.9 Optical Properties of Nanocrystalline Materials

Nanomaterials have very high surface-to-volume ratio, which increases the number of surface atoms because of the resulting large surface area. The surface atoms are chemically unsaturated, or are in a different bonding environment compared with atoms in the interior. Thus, the surface atoms have different energy levels from those in the interior (Zhang 2009). The surface atoms have electronic states, referred to as trap states, inside the band gap. In nanosized materials, energy levels and DOS are functions of particle size. The divergence of the energy level increases with decreasing particle size, which is known as the quantum confinement effect. The energy gap becomes a function of the particle dimensions, as described by the effective mass model or Burs model (Iiz-Marzan and Kamat 2003):

$$E_g(nano) = E_g(bulk) + \frac{\hbar^2 \pi^2}{2R^2}\left(\frac{1}{m_e^*} + \frac{1}{m_h^*}\right) - \frac{1.8e^2}{\varepsilon R}, \qquad (2.9)$$

Where m_e^* and m_h^* are the electron and hole effective masses, respectively, ε is the bulk optical dielectric constant, and R is the particle radius (assuming that the particle shape is spherical). The second term in the equation is the kinetic energy of the electron and hole, and the third term is the Coulomb energy.

The Burs model (Eq. 2.9) indicates that the optical band gap increases with decreasing particle size. The quantum confinement effect is significant when the particle size approaches the Bohr exciton radius. The effect of confinement on energy state in 0-D (quantum dot), 1-D (NW), and 2-D (nanosheet) nanostructures is given by the following equations, respectively (Ashby *et al.* 2009):

$$E_n = \left[\frac{\pi^2 \hbar^2}{2m_e^* L^2}\right]\left(n_x^2 + n_y^2 + n_z^2\right) \text{ (for 0-D nanostructure)} \qquad (2.10A)$$

$$E_n = \left[\frac{\pi^2 \hbar^2}{2m_e^* L^2}\right]\left(n_x^2 + n_y^2\right) \qquad \text{(for 1-D nanostructure)} \qquad (2.10B)$$

$$E_n = \left[\frac{\pi^2 \hbar^2}{2m_e^* L^2}\right]\left(n_x^2\right) \qquad \text{(for 2-D nanostructure)} , \qquad (2.10C)$$

where L is the particle width and n_x, n_y, and n_z are the quantum numbers.

Thus, the DOS (=dN/dE) is highly dependent on the size and dimensions of the nanoparticles, as shown in Figure. 2.8. Figure 2.9 shows the energy diagram for atoms, bulk semiconductors, and quantum dot particles (Alferove 2002).

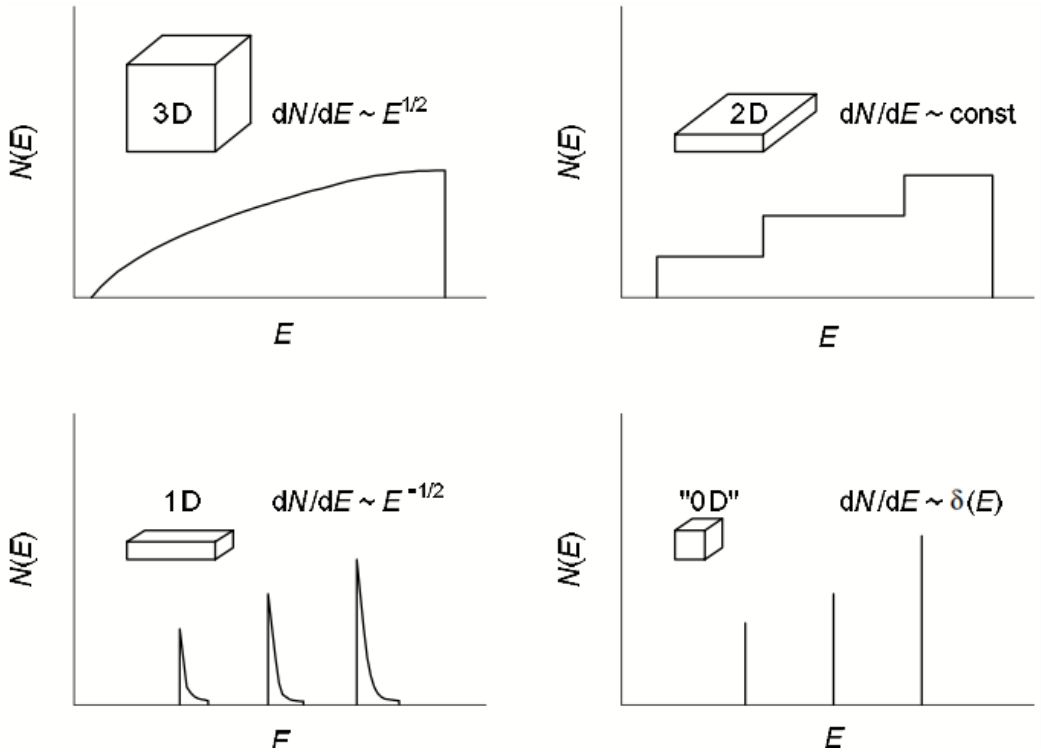

Figure 2.8: DOS for charge carriers in a bulk, 2-D, 1-D, and 0-D nanostructures (Gusev and Rempel 2004).

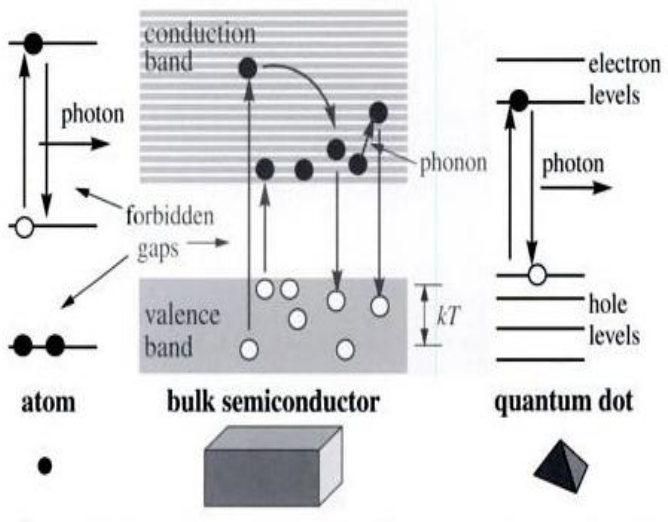

Figure 2.9: Energy level diagrams for atoms, bulk semiconductor and quantum dots particle (Alferove 2002).

2.10 Nanowires (NWs)

A NW is a quasi one-dimensional nanostructure with a diameter of the order of a nanometre. Quantum wires can be defined as structures having a diameter equal or less than 10nm and an unconstrained length. Quantum mechanical effects are important at this scale. In comparison with other low dimensional systems, two confined quantum directions for NWs exist, whereas in the case of electrical conduction, one unconfined direction remains (Bhushan 2007).

Small-diameter NWs have significantly different electrical, optical, and magnetic properties compared with their bulk (3D) crystalline counterparts. This is due to the unique electronic density states of small-diameter NWs (Sattler 2011). The size and form of the NWs affect their overall properties causing variation from those of the corresponding bulk materials. NWs differ from their counterpart bulk materials because of various reasons, including increased surface area, diameter-dependent band gap, very high density of electronic states, enhanced exciton binding energy, and increased surface scattering of electrons and phonons (Grassian 2009).

In small-diameter NWs, some specialized properties can be nonlinear by exploiting the singular aspects of the 1D electronic density of states. In contrast to crystalline bulk materials, this review focuses on the properties of NWs, possible applications resulting from their unique properties, and future studies in this area (Ismail *et al.* 2013).

2.10.1 SiNWs

SiNWs have received much attention, as shown by the increased number of publications investigating SiNWs since 1993. Thus, various synthetic methods have been established for developing SiNWs after the initial discovery of high aspect ratio Si micro- and nanostructures in the 1964s by Wagner's group. SiNWs with unique properties are significantly different from bulk Si, and these properties vary according to the NW morphology. The morphology of SiNWs depends on the deposition methods, growth conditions, and growth mechanisms, which affect the SiNWs properties and applications.

2.10.2 Optical Properties of SiNWs

SiNWs have unique properties because of variations in the morphology of the NW. These include the diameter, length, crystallinity, growth orientation, and the presence of features such as the tip of the catalyst, the number of kinks (growth defects) present in the NWs, and the density of the grown NW. These NW parameters can also affect other properties, such as the optical and electrical characteristics. SiNWs and other nanostructures tend to differ from bulk phase materials because of these properties. The broadband optical absorption properties of SiNW thin films have been investigated and were higher than those of solid thin films of Si of equivalent thickness.

The observed behavior is explained by light scattering and trapping, although the observed absorption is due to a high density of surface states in NW films. Moreover, the reflectance of the solid film shows typical behavior, whereas the reflectance of the NW film is less than 5% for the majority of the spectrum from the UV to the near IR, and begins to increase at ~700 nm to a value of ~41% at the Si band edge (1100 nm), similar to the solid film sample. NWs have a significant reduction of the reflectance compared with the corresponding solid film (Tsakalakos *et al*. 2007; Hasan *et al.* 2013). Since the band gap increases with the decrease of NW diameter, NWs can emit visible light with high efficiency (Jeon *et al.* 2009). The NW band gap is also affected by the surface chemistry because of the high surface-area-to-volume ratio.

The band gap or energy gap is an important property of SiNWs, which is dependent on the NW diameter. The band gap increases with a decrease in diameter from 7 nm to 1.3 nm leading to an increase in the band gap of SiNWs from 1.1 eV to 3.5 eV (Ma *et al.* 2003). The increase in band gap indicates the quantum confinement effect in the SiNWs at low diameters.

2.11 Solar Cells

Solar energy such as photovoltaic energy is the most available renewable energy source and can provide for energy needs on a global scale. A solar photovoltaic (PV) cell converts sunlight into electricity. The history of photovoltaic energy began in 1839 when Alexandre–Edmond Becquerel discovered the photovoltaic effect. Nowadays, Si solar cells represent over 80% of the world's solar cell production, and the yield efficiencies are higher than 15%. In solar technology, the main technological challenge is to improve solar cell efficiency. Several investigations are usually carried out to characterize solar cells. Information on several key is important for estimating the quality of the Si solar cells (Brendel 2003).

A conventional solar cells comprise of two layers of semiconductors, one positive (p-type) and the other negative (n-type), sandwiched together to form a p/n junction. When sunlight is absorbed by a solar cell, the photons generate electron-hole pairs that contribute to the electrical current if they are successfully collected by the electrodes.

When a p/n junction diode is illuminated, photons having higher energy than the band gap of the semiconductor create electron hole pairs. Minority carriers, which are generated within the diffusion length, are swept by the electric field of the space charge region to their respective majority carrier junction sides.

Light-generated current in quasi-neutral regions is created by diffusion of minority carriers; and the current flows in the opposite direction compared with a current flowing in a forward biased p/n junction without illumination (Pagliaro *et al*. 2008). The efficiency of a solar cell is measured by the ratio of the electrical output power and the incident optical power, and is usually expressed in terms of short circuit current, open circuit voltage, and fill factor (Fonash 2010).

$$\eta = \frac{J_m V_m}{P_{in}} \times 100\% \quad , \tag{2.11}$$

where J_m is the maximum current density, V_m is the maximum voltage, and P_{in} is the power of the incident light. The Fill Factor *FF* is the ratio between the power of the maximum operation point and the product of the short circuit current and open circuit voltage (Fonash 2010).

$$FF = \frac{J_m V_m}{J_{SC}\, V_{OC}} \tag{2.12}$$

The Fill Factor is reduced by series resistance, leakage current over the edges of the solar cell, or leakage current caused by recombination. The electrical parameters of the solar cell are depicted in a schematic current-voltage characteristic, as shown in Figure. 2.10.

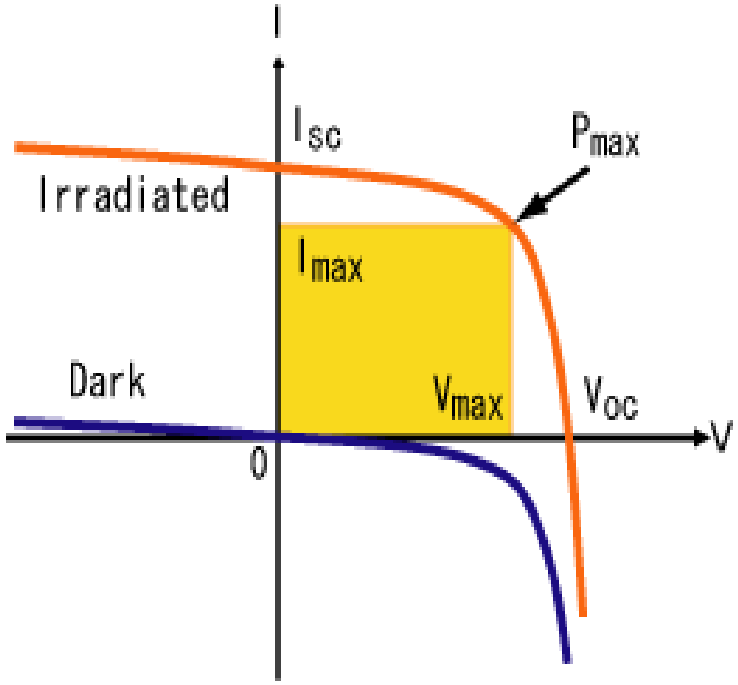

Figure 2.10: Current-voltage characteristic of the solar cell under dark and illumination conditions (Fonash 2010).

In real cells, power is dissipated through the contact resistance and through leakage currents around the sides of the device. Electrically, these effects are equivalent to two parasitic resistances in series (R_s) and one in parallel (R_{sh}), as shown in Figure. 2.11. Series and parallel resistances reduce the fill factor. Hence, for an efficient cell, a small R_s and a large R_{sh} are necessary. The series resistance arises from the cell material resistance to the current flow, particularly current flowing through the front surface to the contacts, which is a serious problem at high current densities under concentrated

light. The parallel, or shunt, resistance is a problem of poorly rectifying devices and arises from leakage of current through the cell (Pagliaro *et al.* 2008).

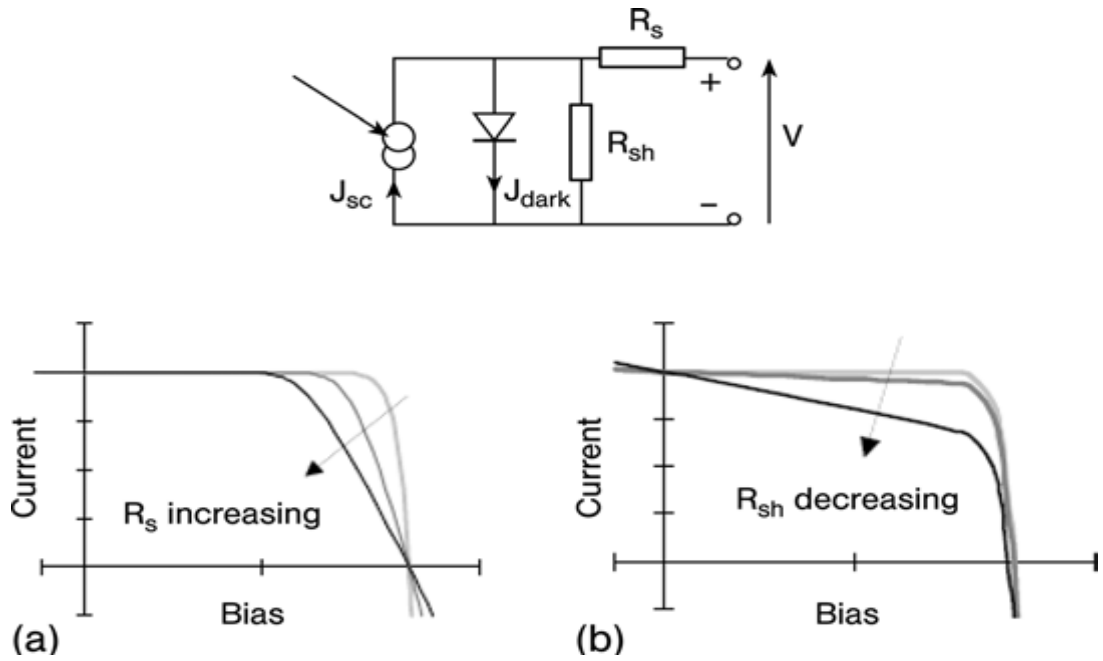

Figure 2.11: The effect of (a) series resistance and (b) parallel resistance on the I-V characteristic curve of the solar cell (Pagliaro *et al*. 2008).

2.11.1 Si Solar Cell

Si is one of the most commonly occurring materials on earth, and is usually in the form of SiO_2 in quartz and sand. Si is a Group IV element, many of which are semiconductors. The most common crystal structure of Si is the covalent-bonded diamond structure. Basic information on elemental Si is listed in Table 2.1 (Sze 2007a). Si source material is extracted from quartz, processed until very high purity is obtained, and subsequently melted. From the melted Si, a large single cylindrical crystal is drawn and sliced into wafers of typically 500 microns thickness.

This process is also known as the Czochralski (CZ) process, which remains a key technology in photovoltaics because of the higher energy conversion efficiency of single crystalline Si (sc-Si), and approximately 45% of Si is grown by this method (Nakajima 2009).

Table 2.1: Basic information on elemental Si

Property	Value
Atomic number	14
Melting point	1410 ^{o}C
Density at 293K	2.329 cm^{-3}
Energy gap, E_g, at 300K	1.12 eV
Color	Dark gray with bluish tinge
Crystal structure	Cubic-diamond Fd-3m
Lattice constant	0.54309 nm

2.11.2 Crystalline Si Solar Cells

Crystalline Si (c-Si) is the basis for most integrated circuits (ICs) as it is a readily available semiconductor. It is easily processed and doped to form semiconductor devices. It is used in many optical and electronic devices such as ICs, diodes, and solar cells. The earliest photovoltaic devices or solar cells were made from c-Si. It is still commonly used for these devices because it contributes to high efficiency of the devices, and crystalline Si solar cells are the main constituents of first generation photovoltaic devices (Solanki 2011).

First-generation photovoltaic cells are currently the dominant technology in the commercial production of solar cells, accounting for more than 86% of the solar cell market. The major drawback is that crystalline Si is an indirect band gap material, and at least 30μm-thick devices are required to absorb 80% of the incident sunlight. The primary objective of the PV industry should be to reduce the cost. Even with greatly increased production volume and significant reduction of cost, crystalline Si solar cells may not be able to meet the long-term cost of utility-scale power generation.

Increasing efforts to reduce Si consumption can be observed globally, and the industry is exploring solar modules from thin films of c-Si (Brendel 2003). Another type of Si is polycrystalline Si, which comprises a series of small crystallites grown together with an extremely high crystallinity or a proportion of crystalline materials. Polycrystalline Si typically has a grain size (crystallite diameter) ranging from 10μm to 30μm, and a crystalline fraction close to 100% (Ismail *et al*. 2013). The polycrystalline materials are synthesized by the CVD method (Cabarrocas 2004).

Microcrystalline Si (μc-Si) consists of crystalline and amorphous phases, and it has a grain size between 10nm and 200nm, and a crystalline fraction ranging from 10% to 100%. The μc-Si is an attractive material for electronic device applications because of its higher carrier mobility than a-Si, and hence, high electrical conductivity. Usually, μc-Si thin films are prepared by PECVD and HWCVD (Carius *et al.* 2003).

2.11.3 Amorphous Si Solar Cell

In the early 1970s the semiconductor properties of a new form of Si, amorphous Si (a-Si), were discovered. This type of Si does not have long-range order, and it has a random orientation. The light absorption coefficient in a-Si is much higher than that of c-Si because it is a direct band gap material. The thin film devices fabricated from a-Si can absorb more of the light than the thicker c-Si slices.

One of the main uses of a-Si is the fabrication of cheap thin film solar cells. a-Si is a randomly structured glass-like material. Amorphous solar cells made of a-Si fairly unique properties, regardless of their disadvantages, which include the presence of numerous dangling bonds in a-Si, caused by the lack of order, that trap the charge carriers and accordingly reduces the efficiency of the cell (Kitai 2011). a-Si is probably one of the most widely researched materials in thin film technology, and it offers a variety of advantages such as a band gap around 1.7eV, in which the maximum solar energy efficiencies are expected, and also a high absorption coefficient in this region of more than $10^5 cm^{-1}$.

The a-Si solar cells can easily be fabricated at low deposition temperatures over large areas. The defect densities are usually very large in a-Si, which leads to several limitations. One of the main disadvantages of a-Si is that the performance of a-Si solar cells degrades from 10% to 30% with prolonged exposure to sunlight. This has led to efforts to combine a-Si with µc-Si in order to improve the quality of the solar cells.

CHAPTER 3
METHODOLOGY AND CHARACTERIZATION TOOLS

3.1 Introduction

This chapter describes the pulse plasma enhanced chemical vapor deposition (PPECVD) technique used for the synthesis of silicon nanowires (SiNWs). In addition, this chapter discusses the theory of the major experimental measurement tools. The fabrication and characterization of SiNW PV devices are also described in this chapter. The methodology of device fabrication and characterization is shown in Figure 3.1.

3.2 Substrate Preparation and Metal Catalyst Coating

Indium tin oxide (ITO)-coated glass was used as a substrate to grow SiNWs. The substrate dimensions were 1.5cm wide and 5cm long. The substrates were cleaned in an ultrasonic bath using decon-90, ultra-pure water, and 2-propanol sequentially for 5min for each step. The substrates were then dried using high purity nitrogen flow before being held in the evaporating equipment. The substrates were fixed onto the holder of the thermal evaporation system (Bell Jar) to deposit the catalyst thin films. Gold (Au), tin (Sn), aluminum (Al) and zinc (Zn) were used as catalysts to grow the SiNWs. The metal was placed in either a tungsten boat or on a coiled tungsten filament attached to the two electrodes within the system.

The chamber of the system was evacuated to a pressure of 10^{-5} torr during the film deposition process. Varying thicknesses of metal thin films from 10nm to 100nm were synthesized. The thin film thickness was controlled by a quartz crystal microbalance (QCM) connected to the substrate holder. After the required thickness of metal was deposited, the shutter was closed and the system was turned off. To avoid the oxidation

of Al or Zn metals, the samples were kept under vacuum over night and carried directly to the PPECVD system to prepare SiNWs. Figure 3.2 shows the Bell jar thermal evaporation equipment.

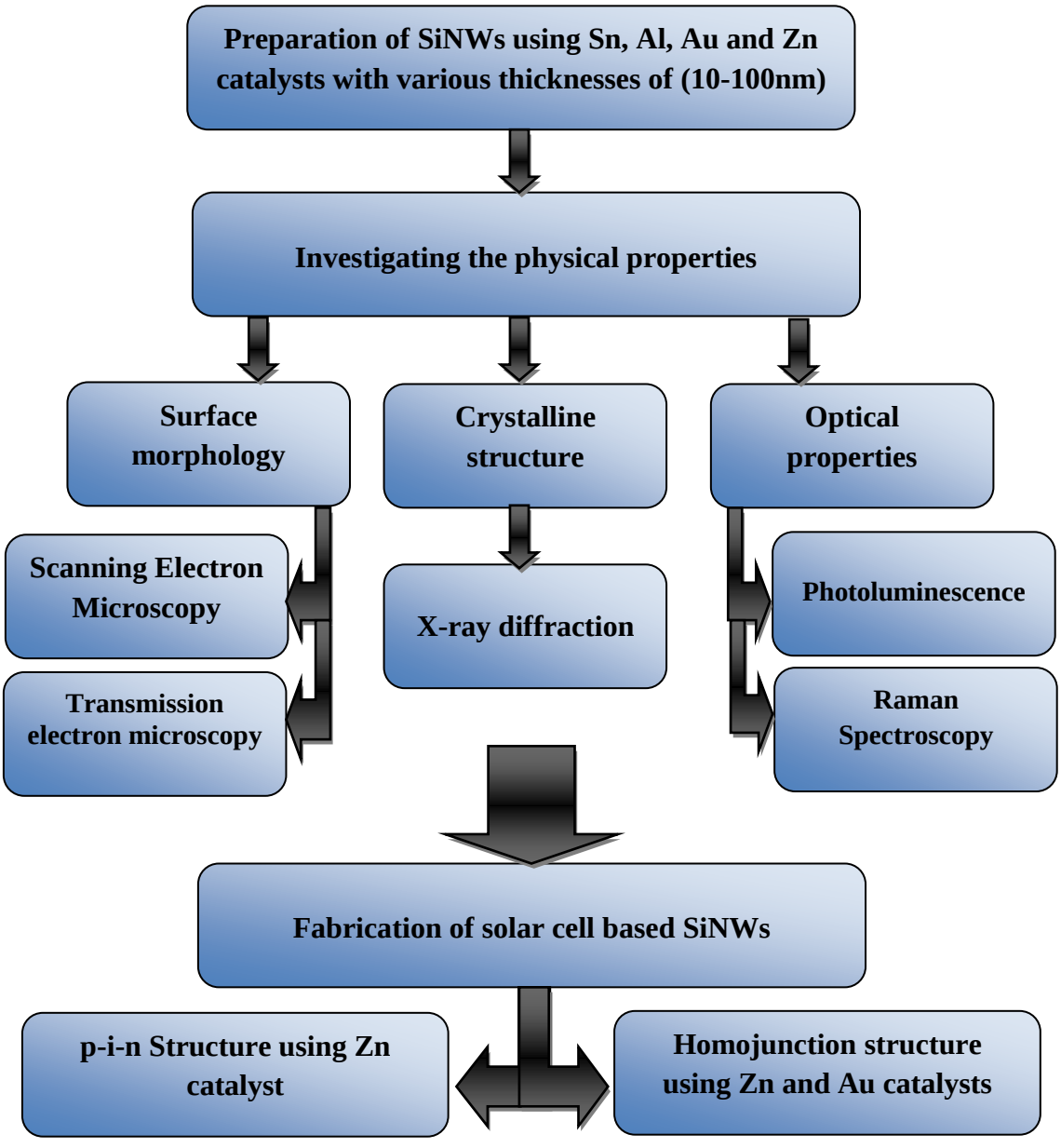

Figure 3.1: The methodology, device fabrication and characterization.

3.3 Pulsed PECVD Deposition System

PPECVD is a technique widely used to produce SiNWs. The wires are synthesized in a plasma medium to promote the decomposition of precursor into reactive species. The deposition temperature can be lowered in order to reduce thermal damage to the device. The equipment used for PPECVD is shown in Figure 3.3. It consists of a stainless steel chamber 20.2cm in diameter and 20.5cm high.

The chamber is connected to rotary and diffusion pumps to evacuate the system until a pressure of 10^{-6} torr is obtained. The silane rotary pumps are backfilled with argon to prevent oxidation of silane with the pump. There is a range of reactant gases that can be connected to the deposition system which includes silane, diborane, phosphine and argon.

The proportions and flow rates of the various gasses are controlled by the mass flow controllers (MFC) into the common manifold. Each MFC is colour coded to the appropriate gas line e.g. white for silane, yellow for phosphine and for each controller (1 to 5) there is a switch (valve control) which can be either closed, controlled flow rate or open. In addition, each of the gas lines and the manifold can be individually evacuated and purged using argon gas.

Before and after each deposition the chamber and gas lines should be flushed and purged to prevent contamination. Modifications have been made to extend the capabilities of the PECVD system to incorpate pulsed PECVD (PPECVD) and to include pulsed capabilities was fairly straightforward due to the use of a consumer CB radio. A pulse generator (SRS model DG535) was attached to the microphone input of the CB transceiver which is then switched to AM mode when PPECVD is used.

A 13.56MHz signal is generated by a commercially CB radio transceivers which used to produce a plasma. The signal then passed through a RF wattmeter (Bird 43) to measure the signal power. Figure 3.4: shows a schematic diagram of the reactor chamber (Steiner 2004).

Figure 3.2: Bell jar thermal evaporation equipment.

Figure 3.3: The PPECVD equipment.

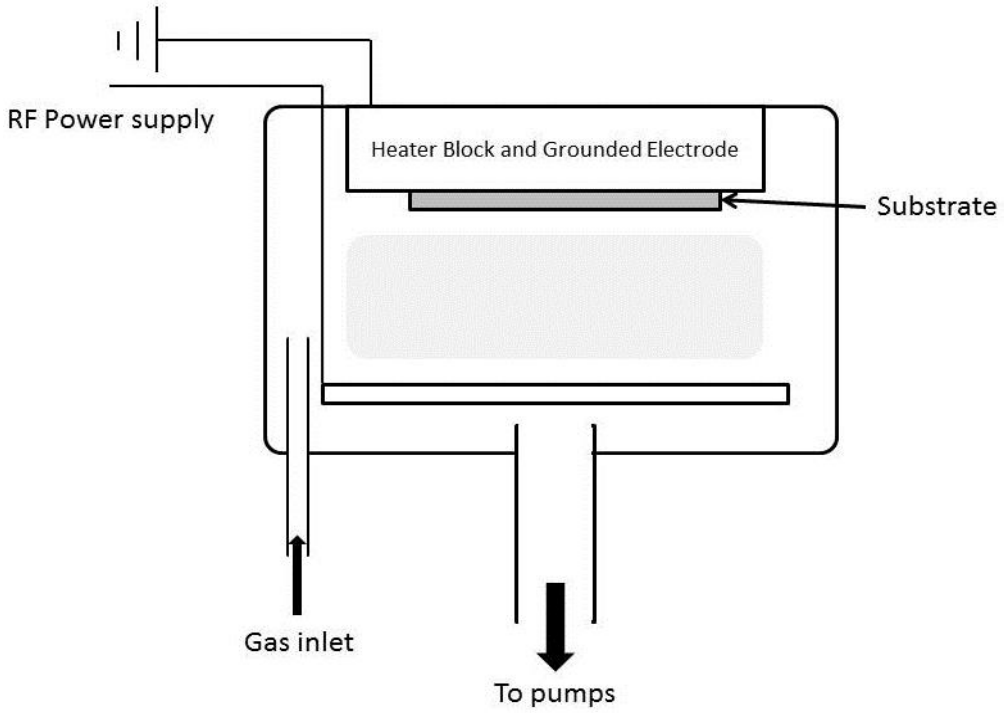

Figure 3.4: Schematic diagram of a PECVD.

3.3.1 Synthesis of Silicon Nanowires via PPECVD

Silicon nanowires were grown successfully using the deposition system at Murdoch University as show in Figure (3.3) that which allows producing of amorphous Si, microcrystalline and also nanostructure Si. Silicon nanowires were grown by the Pulsed PECVD method using varying thicknesses of metal catalyst thin films ranging from 10nm to 100nm deposited on indium tin oxide (ITO)/glass substrates. The catalyst-covered substrates were loaded into the PECVD chamber and heated in the presence of 3torr argon to approximately 350°C for 35min. Afterwards, silane (SiH_4) gas was allowed to flow into the chamber as the Si source, and the temperature was increased to approximately 400°C. The growth process was conducted under pulsed plasma with a frequency of 13.56MHz supplied by a square wave pulse generator using a modulation frequency of 1,000Hz and approximately 30W of power for 45min. After the deposition process was completed, the system was purged with argon and cooled to near room temperature. Finally, the samples were removed and prepared for analysis.

3.4 Measurements Tools

3.4.1 Scanning Electron Microscopy

The scanning electron microscope (SEM) is one of the most powerful tools used to investigate the surface morphology of materials**.** Since the appearance of the first commercial instrument in the 1960s, the design of the SEM has been constantly improved (Khursheed 2011). Field emission scanning electron microscopy (FESEM) uses a field emission gun instead of typical electron gun sources used in an SEM system. The electron beam passes through electromagnetic lenses, focusing onto the sample, resulting in the reflection of different types of electrons.

The high-energy electrons (backscattered electrons) are caused by the elastic collisions deep inside the sample, whereas the secondary electrons are produced from the inelastic collision on the sample surface or close to the surface (Khursheed 2011). The secondary electrons are then collected by the detector to obtain an image of the sample surface. In addition, choosing a suitable accelerator voltage is important for generating a high-resolution image. Moreover, the interaction of the primary electrons with the sample generated photons with the X-ray wavelength range. With the detection of this radiation, the elemental ratio in the sample can be analyzed through energy dispersive spectroscopy (EDS).

3.4.1.1 Experimental Procedure

The grown SiNWs were analysis and characterized using two scanning electron microscopes; most of prepared samples were examined using high resolution imaging (FEI Nova NanoSEM 450 FESEM) located in University Sains Malaysia as shown in Figure3.5. The second instrument was based a Philips XL 20 SEM at Murdoch university.

The SiNWs catalyzed by varying thickness of Au, Al, Sn and Zn metals were produced on ITO coated glass substrates. The samples were mounted directly to the FESEM system to take different magnifications of micrographs. Moreover, some samples are cut and fixed vertically on the stage of FESEM equivalent for cross sectional images. Cross section FESEM was measured for three thickness of each catalyst that was used to catalyze SiNWs, and the NWs length were measured.

The NWs diameter distribution as well as the density (number of NWs per square micrometer) of the samples was collected from FESEM images. The EDX measurement was operated during the FESEM observation and the EDX analysis carried out for one catalyst thickness was used to confirm the elemental ratio and type. An FESEM system (FEI Nova NanoSEM 450) was used to study the morphology of this research (Figure 3.5).

Figure 3.5: FEI Nova NanoSEM 450 FESEM equipment.

3.4.2 Transmission Electron Microscopy

As a result of the experiment of Ruska and Knoll, the first transmission electron microscope was built in 1931 with a magnification of 16 times (Wang N et al. 2003). After that, extensive efforts were made to enhance the resolution of the transmission electron microscope (TEM). The principle behind the TEM is similar to that of the SEM except that in TEM, the electron beam passes (transmits) through the specimen, requiring the detector to be fixed behind the sample holder. The electron density distributed behind the sample is focused onto a fluorescent screen by lenses. Given the strong interaction between the electron beam and the atoms of the samples by elastic and inelastic scattering, the specimen should be very thin, with thickness ranging from 5nm to 100nm for a TEM at 100 keV (Reimer L 2008). Thus, the TEM sample should be deposited onto a Cu grid and allowed to dry before measurement.

3.4.2.1 Experimental Procedure

TEM images gives information about the morphology (e.g size, shape and crystallography). Thus, TEM was carried out for several thicknesses of catalysts to confirm the wire diameter that calculated from FESEM images. The prepared SiNWs samples were tested using Philips CM 100 TEM equipment at Murdoch University (Figure: 3.6). The TEM sample were prepared by placing the SiNWs in a beaker containing ethanol and placing the beaker in an ultrasound bath for 2min to remove the wires from the substrate. Then the solution of nanowires was deposited on a Cu grid and allowed to dry before the measurement.

3.4.3 X-ray Diffraction

X-ray technology has been used for more than a century. Its discovery and development has revolutionized many areas of modern science and technology (He B.B 2009). X-rays were discovered in 1895 by the German physicist Wilhelm Conrad Röntgen, who was honoured with the Nobel Prize for Physics in 1901. In 1912, Lawrence Bragg suggested a mathematical formula for the diffraction condition, known as Bragg's Law,

$$n\lambda = 2d_{hkl}\sin\theta \ , \qquad (3.1)$$

where n is an integer representing the order of reflection (its value is usually taken as 1), λ is the wavelength in angstroms, d is the inter-planar spacing in angstroms, hkl represents Miller indices, and θ is the diffraction angle in degrees. X-ray diffraction is based on the elastic scattering of X-ray from matter.

Given the wave nature of X-ray, the scattered X-rays from a sample can interfere with each other such that the intensity distribution is determined by the wavelength, the

incident angle of the X-ray, and the atomic arrangement of the sample structure, particularly the long-range order of crystalline structures.

The distribution of the scattered X-rays is referred to as an X-ray diffraction pattern. The atomic level structure of the material can then be determined by analysing this pattern. Figure 3.7 shows the diffraction of X-ray waves from two planes of a crystalline material. The lattice constant (a) of the crystalline material can be calculated using a formula that depends on the structure type. However, the simples crystalline structure are cubic and hexagonal. The lattice constant (a) of cubic structures is given by (Cullity B.D 1972):

$$a = d_{hkl}\sqrt{h^2 + k^2 + l^2} \tag{3.2}$$

High-resolution X-ray diffraction equipment (PANalytical X'Pert PRO MRD PW3040) was used in this study (Figure 3.8). The X-rays were generated by a copper (Cu) target with CuKα wavelength of 1.5443 Å. The voltage and current used were 40 kV and 35mA, respectively.

Figure 3.6: Philips CM 100 TEM equipment.

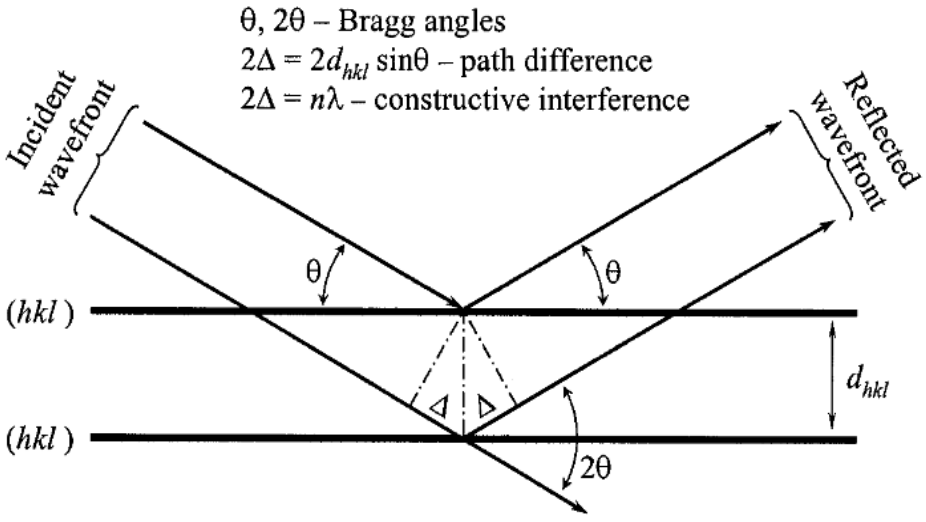

Figure 3.7: Geometrical illustration of Bragg's Law (Recharsky and Zavalij 2003).

Figure 3.8: High resolution X-ray diffraction equipment.

3.4.5 Photoluminescence (PL) System

When a semiconductor is exposed to electromagnetic radiation, a portion of this radiation will be absorbed leading to the excitation of an electron to a higher energy level. When the excited electron returns to a lower energy level it results in photon emission. Studying the PL spectrum of materials is important because of the potential information it provides about optical properties of materials.

Room temperature PL was measured using a Jobin Yvon HR 800 UV system which uses 325 nm 20 mW HeCd laser light for excitation. The PL and Raman system is shown in Figure 3.9.

3.4.6 Raman spectroscopy

The Raman effect, named after Chandrasekhara Venkat Raman (1888 - 1970), involves the change in the frequency of light when it is scattered by polyatomic molecules (Robert B 2009). Since the first observation of Raman scattering by Raman and Krishnan in 1928, Raman spectroscopy has been widely used in characterizing materials (Khan *et al.* 1963). When the specimen is irradiated by laser light, the Raman effect occurs, resulting in inelastically scattered light with shifted frequency because of the interactions with the vibrational modes of the chemical specimen (Czichos *et al.* 2006).

The effectiveness of the bond toward Raman scattering is directly dependent on the polarizability, which decreases as the electron density increases or the length of the bond decreases. As a result, symmetric vibrational bond stretches are typically Raman-active (Khan *et al.* 1963). Raman spectroscopy is an effective tool to provide information on doping concentration, lattice defect identification, and crystal orientation of materials socially nanostructured via the effect of phonon confinement (Wu *et al.* 1996; Mahdi *et al.* 2012). Raman measurements were carried out using an Ar ion laser (514.5nm and 20 mW light) for the excitation.

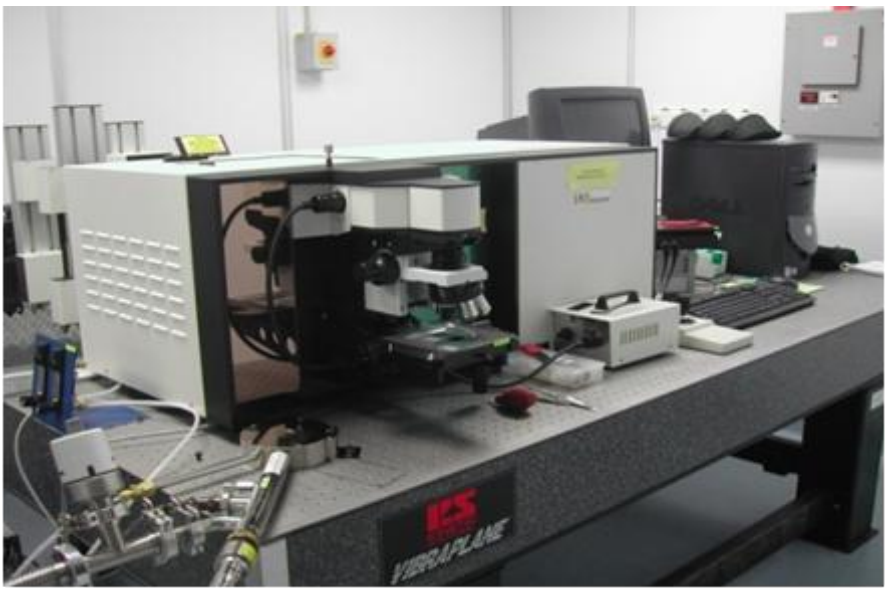

Figure 3.9: Raman and PL spectroscopy system.

3.4.7 Current–voltage (I–V) characteristic

Current-voltage (I-V) measurements refer to D.C. characterization of devices for the purposes of performance analysis and parameter extraction. The I-V characteristic of the prepared devises (solar cells) was investigated in dark and under illumination by white light supplied by a 120 V/300 W halogen lamp, which was calibrated using standard crystalline silicon solar cells. All the device parameters such as efficiency, fill factor, series resistance, shunt resistance, etc, and can be calculated from the I-V characteristic. The contact grid was deposited as a finger-finger type with area of 0.5×0.5 cm^2 using Al metal. Figure 3.10 shows the schematic diagram of the I-V characterization system that used in our work, the samples were placed in a box to ensure they were exposed to the lighting conditions. The I-V data of the solar cell was analyzed using Labview software. The solar cell parameters of the fabricated solar cell were calculated.

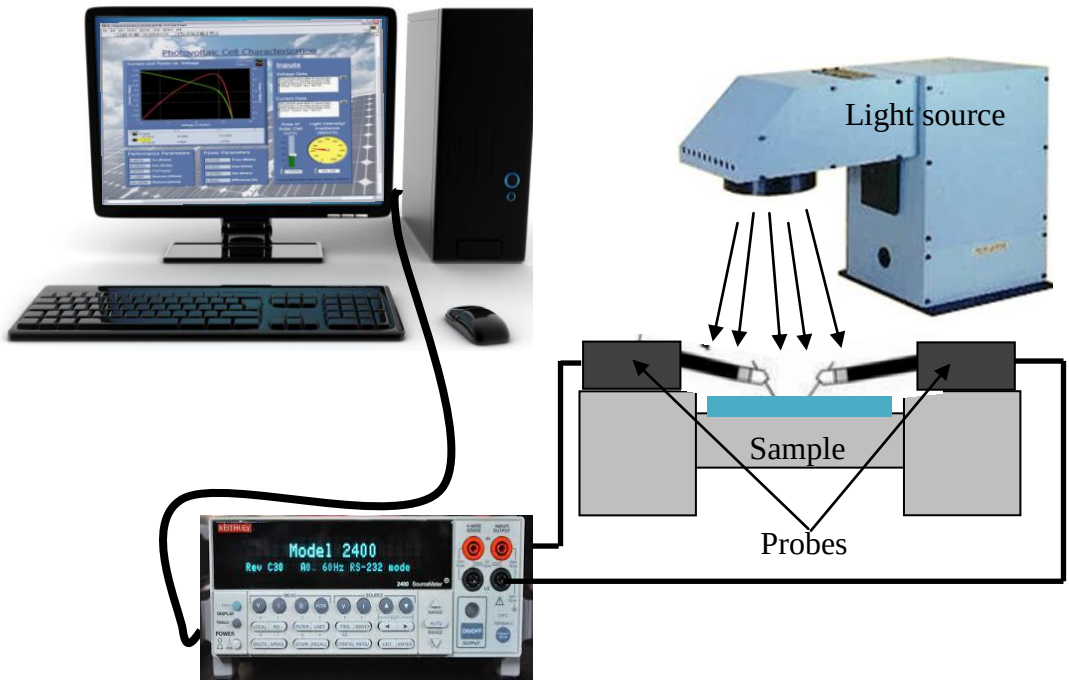

Figure 3.10: Schematic of the current-voltage characterisation system.

CHAPTER 4
PREPARATION AND PROPERTIES OF Sn CATALYZED SiNWs

4.1 Introduction

Varying thicknesses of Sn catalyst in the range of 10nm to 100nm were used to produce SiNWs. The Pulsed PECVD method was used to synthesize high density NWs on ITO substrates at 400^{o}C. This Chapter describes how to control the diameter of the SiNWs by controlling the thickness of the Sn catalyst and how it can affect the morphology, structure and optical properties of the grown NWs. An investigation of the morphology of the prepared SiNWs with Field Emission Scanning Electron Microscopy (FESEM) and Transmission Electron Microscopy (TEM) are presented. In addition, the crystalline structure of SiNWs is explored via X-ray diffraction (XRD). The optical properties which include the photoluminescence (PL) and Raman spectra are also reported.

4. 2 Synthesis of SiNWs catalyzed with Sn

4.2.1 Surface morphology

Figure 4.1 shows the FE-SEM images of the SiNWs grown on ITO-coated glass substrates with Sn thin film catalysts having different thicknesses. The SEM images show that the SiNWs are tapered when thinnest catalyst used. For the SiNWs grown using the 10nm thin film Sn catalyst, the SiNWs appear to be inhomogeneous in diameter and the wires are tapered at the end (Figure 4.1A). Using a Sn catalyst thin film with 20nm thickness, resulted in the prepared SiNWs having a more homogenous

diameter. The tapered end occurred in some wires (Figure 4.1 B) and completely disappeared when a film thickness of 40nm was used (Figure 4.1C).

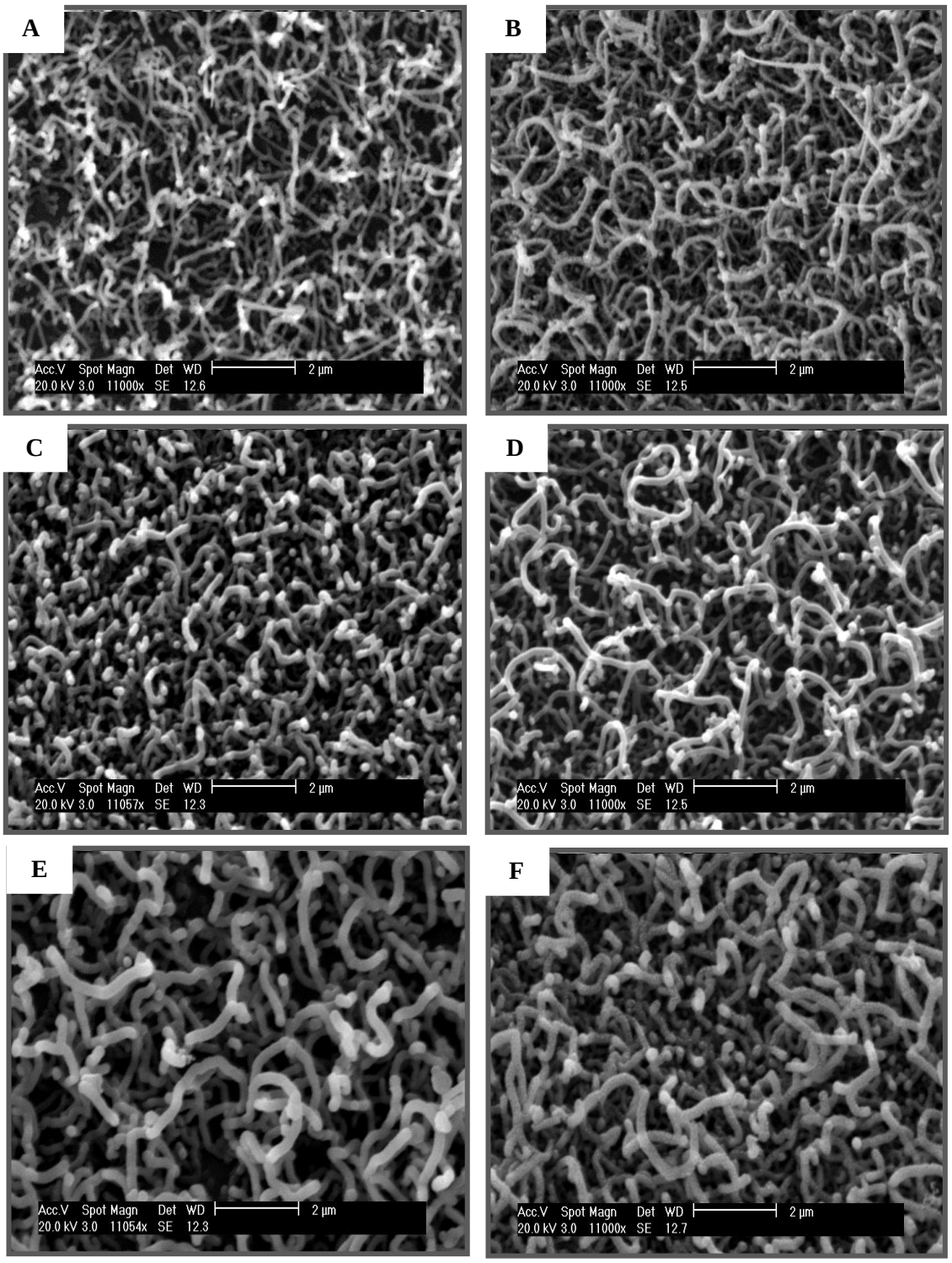

Figure 4.1: FE-SEM images for SiNWs prepared using Sn catalyst thickness of (A) 10nm, (B) 20nm, (C) 40nm, (D) 60nm, (E) 80nm and (F) 100nm.

The droplet sizes with 10 and 20nm catalyst thin films are relatively small compared with the other thicknesses used, thus the small droplets apparently didn't control the growth of the wires, due to the loss of Sn into the SiNWs. The SiNWs grown using 60, 80 and 100nm film thicknesses, showed significant improvements in the morphology of the wires, especially in terms of the diameter homogeneity (Figures 4. 1D- F). To identify the optimal Sn thin film thickness for growing SiNWs, the diameter distribution was calculated using image analyzer software. About 100-120 wires on average were selected randomly to determine the diameter distribution of the grown SiNWs with an error ratio of about ±5%. Figure 4.2 shows the wire diameter increased with the increase in the thickness of the catalyst thin films (Figure 4. 2). The diameters of the SiNWs ranged from 60 - 110nm with a catalyst thickness of 10nm and increased to a range of 80 - 130nm with use of 20nm Sn thin film catalysts. Furthermore, the range of diameters of the SiNWs for the samples prepared using a Sn thin film thickness of 100nm were 160 to 220nm. From the FESEM images, the density (number of nanowires per μm^2) of SiNWs grown using the Sn catalyst was measured and found to decrease from 15NW/μm^2 to 6NW/μm^2 when the Sn catalyst thickness increased from 10nm to 100nm, respectively as shown in Figure 4.3. Also the model wire diameter increased from 75nm to 195nm when the catalyst thickness increased from 10 to 100nm.

Moreover, the mode of the average diameters was found to increase linearly as the Sn catalyst film thickness increased. In addition, it was observed that an increase in the thickness of the Sn thin films led to an increase in droplet diameter as presented in Figure 4.1, which in turn led to the increase in the diameter of the grown SiNWs. This allows the average diameter of the nanowires to be selected by using the appropriate catalyst layer thickness.

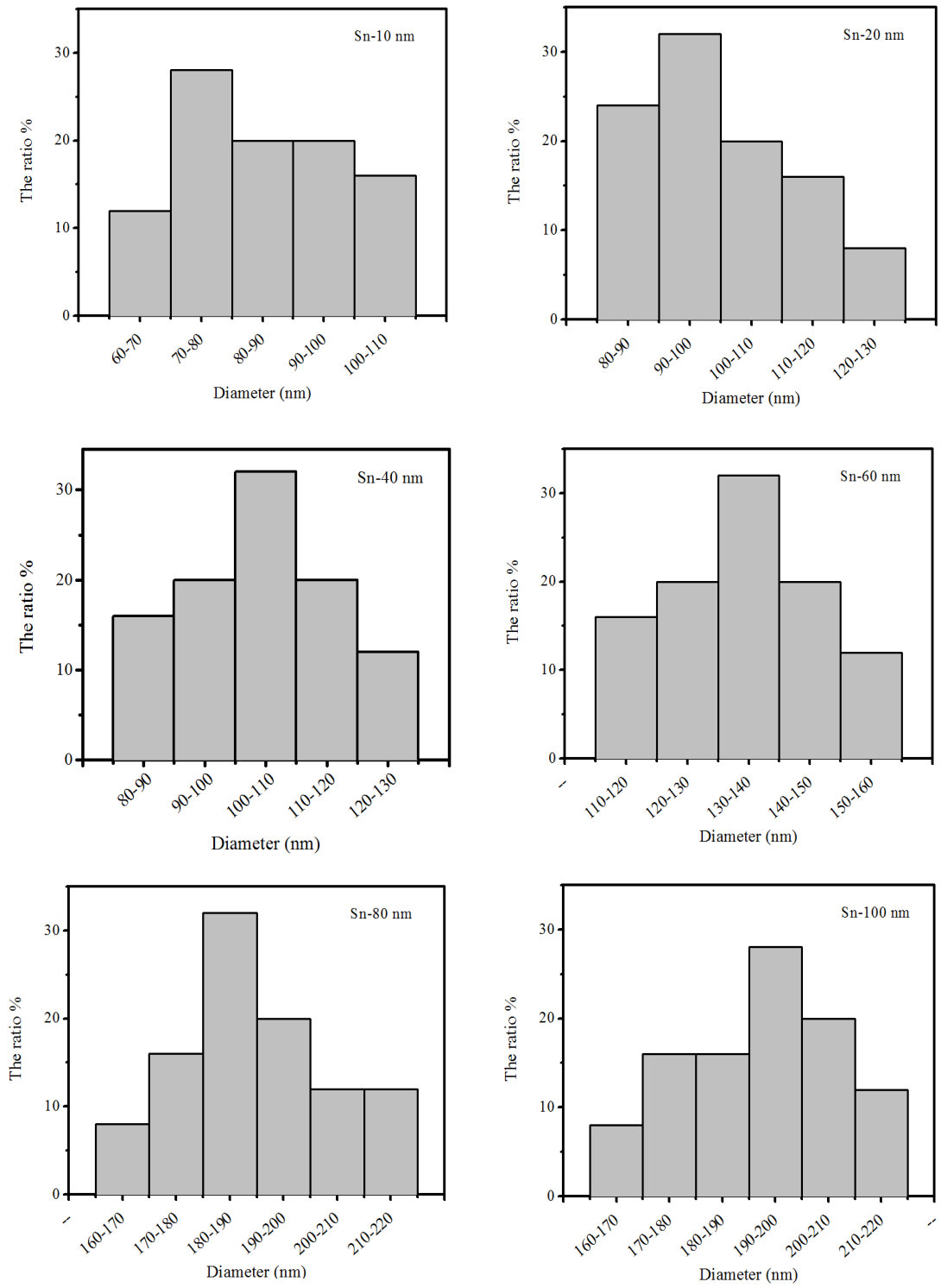

Figure 4.2: Diameter distribution of the grown SiNWs.

The cross sectional FESEM images of SiNWs prepared using 20, 60 and 100nm Sn thin film thicknesses are shown in Figure 4.4. The average lengths of SiNWs catalyzed by 20 and 100nm Sn thin films were 4.1 and 3.7μm, respectively.

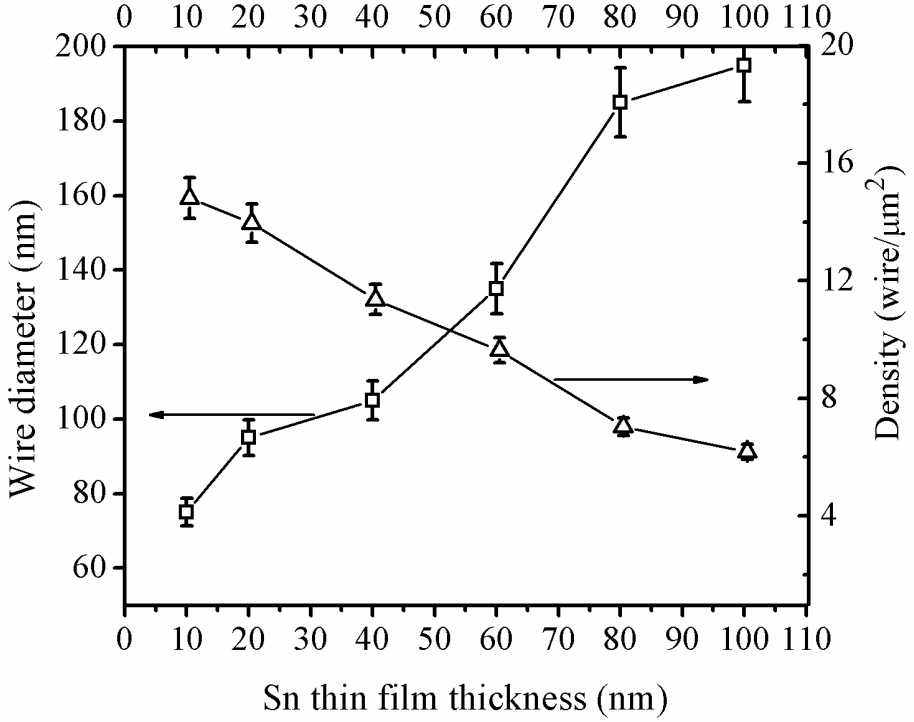

Figure 4.3: The catalyst thin film thickness vs. wire diameter and density.

Figure 4.5 shows the TEM images of SiNWs prepared using Sn catalyst thin film thicknesses of 20, 60, 80 and 100nm, respectively. The TEM images confirm that the grown wire diameters increase as the catalyst film thickness increases. As shown in Figure 4.5, the diameters of SiNWs prepared using 20 and 60nm Sn thin film thicknesses ranged from 95 to 105nm while it ranged from 170 to 195nm for the SiNWs catalysed by 100nm Sn thickness. The Sn droplets didn't show up clearly on the wire tip except for one wire in the 20nm Sn catalyst sample, showing that the growth mechanism producing SiNWs was the VLS mechanism.

The metal Sn has a different coefficient of the thermal expansion than to Si that could led to the separation the Sn droplets from SiNWs during the cooling process of the samples. The surface tension value of Sn liquid is 0.6 J m^{-2} (Schmidt 2009), which is lower than the required value (0.85 J m^{-2}) to make the droplets sit on the wire end (Schmidt 2009) thus, the Sn droplets mostly fell off when the TEM samples were prepared using ultrasonic treatment.

The Sn-Si phase diagram (Figure 4.6) (Bhushan 2007) shows that the Sn melting point is about 232^{o}C. During the growth process, at a temperature of 400^{o}C, and before the SiH_4 gas is introduced into the PECVD chamber, the Sn particles melted and aggregated to form large droplets due to surface tension. Furthermore, when the Sn droplets were exposed to SiH_4 gas, the gas molecules disintegrate at the surface of the Sn droplets and the Si dissolves in the Sn and forms the Sn-Si liquid phase.

The eutectic point of Sn-Si is very low at about 232^{o}C with a silicon ratio less than 1% compared with other catalyst metals such as Au (363^{o}C, Si of 19%) and Al (577^{o}C, Si of 12%) (Schemidt et al 2009). Thus, the Sn-Si liquid phase formed at very low Si concentration, and thus a low pressure of Si atoms was required when using Sn to grow SiNWs which is potentially very cost effective. Furthermore, during the growth processes the length of the wires increases and when two wires or more meet they can make a shape like loop or a kink.

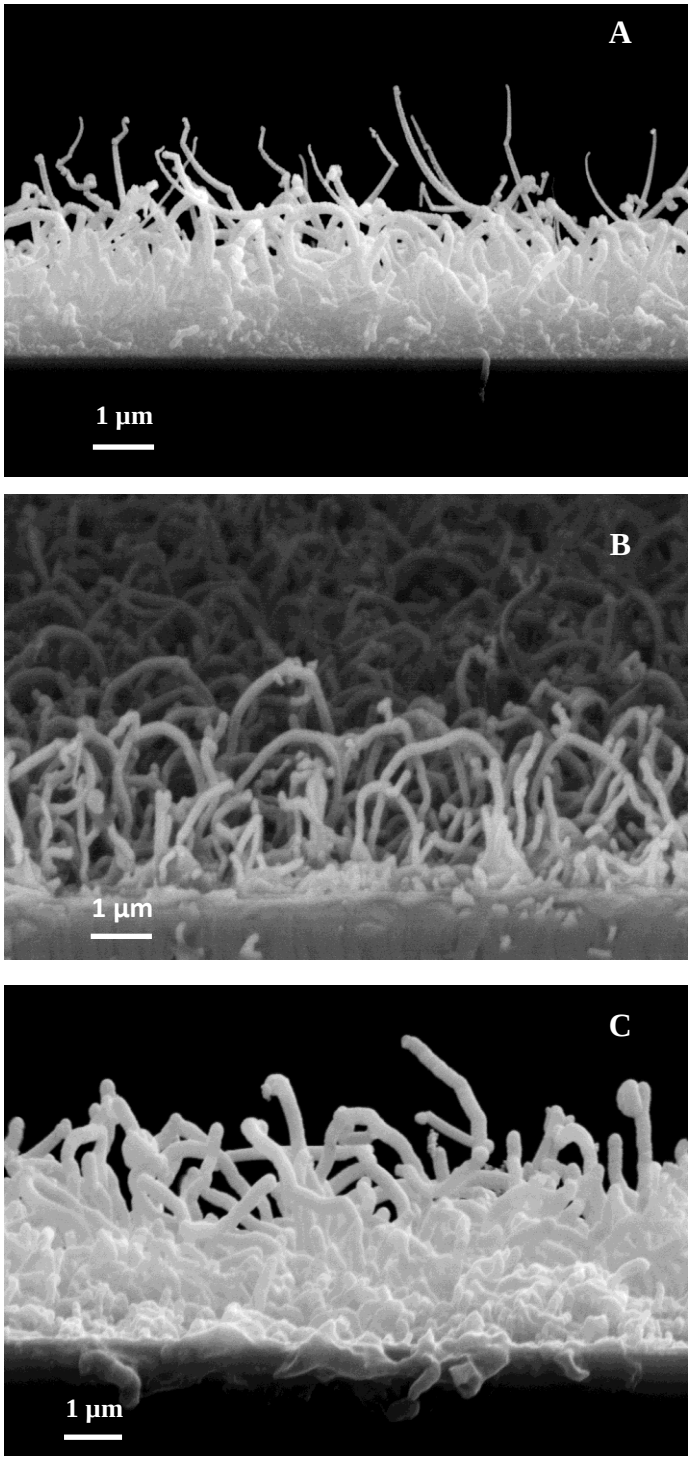

Figure 4.4: Cross-sectional FE-SEM images for SiNWs synthesized using Sn catalyst thicknesses of (A) 20nm, (B) 60nm and (C) 100nm.

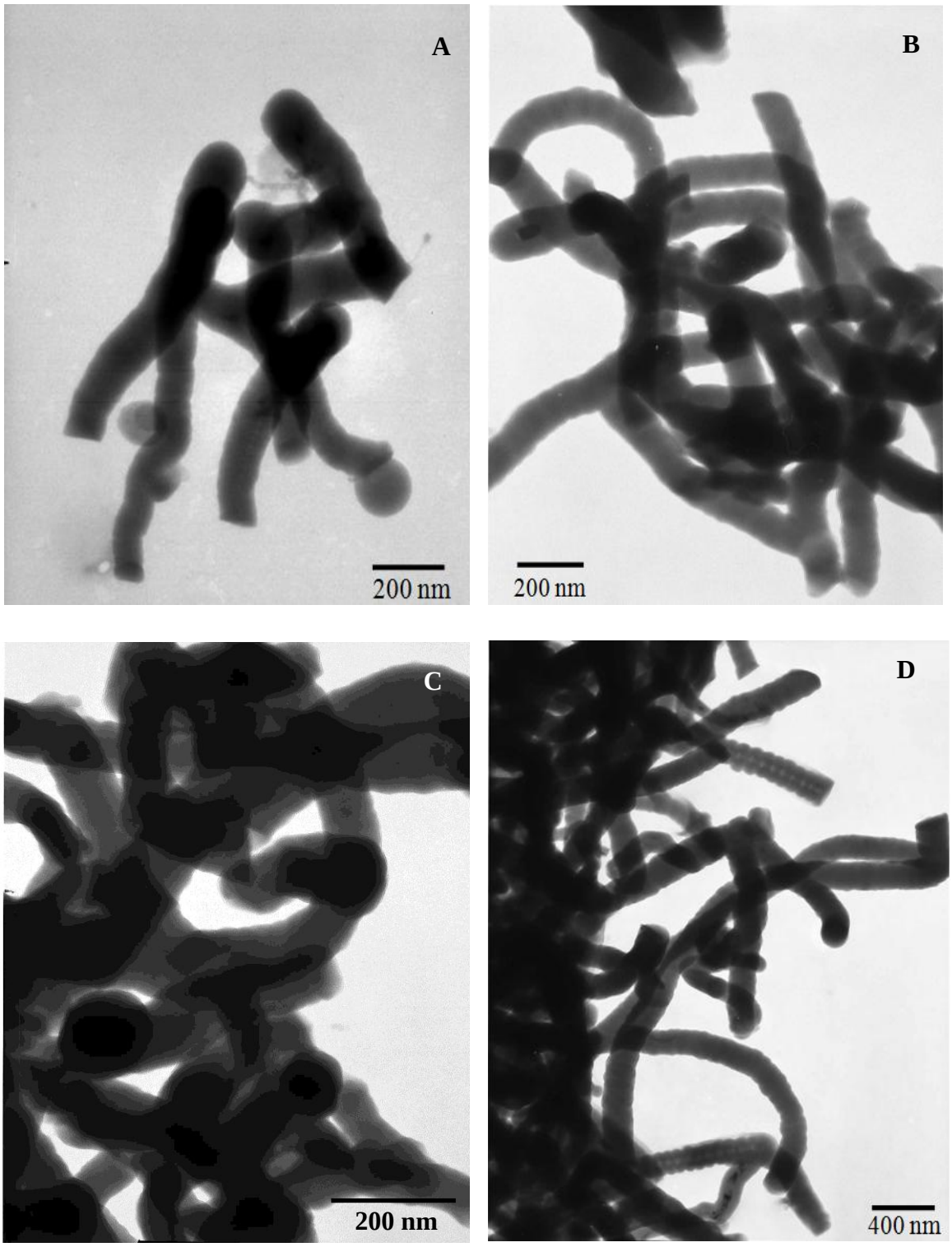

Figure 4.5: TEM images of SiNWs prepared by Sn catalyst thin film thicknesses of (A) 20nm, (B) 60nm, (C) 80nm and (D) 100nm.

A few preliminary studies have been reported for Sn-catalyzed SiNWs. Yu *et al.* (2009a) used hydrogen radical-assisted deposition method to synthesize SiNWs for the studies of the effects of metal catalyst thickness. They studied the effect of the Sn thin films thickness on the morphology of the grown SiNWs and found that the nanowire diameter is determined by the size of the catalyst droplet which nucleates the nanowire. The findings show that SiNWs produced using a relatively thin layer (30nm thick) of Sn catalyst are better arranged and controlled than those produced on relatively thick Sn-coated catalysts (100nm thick). However, we found that increasing the Sn catalyst thickness to 60, 80 and 100nm led to the growth of more homogenous SiNWs.

Jeon and Kamisako (2009) used a 7nm thick Sn catalyst at 400°C to grow SiNWs by VLS and also obtained a homogenous diameter. Other types and thickness of catalyst have also been used to grow SiNWs. Cui *et al.* (2001) found that the diameter of the catalyst droplet determines the size of the nanowire, because the diameter of SiNWs increases with the thickness of Au nanoclusters. They also found that the Au-Si alloy droplet diameter is consistently smaller than the diameter of the nanowire during the formation. Wacaser *et al*. (2009) also show the effect of varying the thickness of the Al layer. They also showed that the average diameter of the nanowire increases with the thickness of the Al layer.

The Energy Dispersive X-ray (EDX) spectrum recorded for the SiNWs catalyzed with a 40nm thick Sn catalyst is shown in Figure 4.7. The compositions details of the as-grown SiNWs present in the nanoparticles comprises of Si and Sn with atomic ratios of 66.5 % and 2.95 % respectively. The Sn nanoparticles are located on the top of the as-grown NWs which indicates that the Sn catalyst is essentially involved in the mechanism of growth of the SiNWs. In addition, the EDX spectra in Fig. 4.7 show

peaks corresponding to oxide and the element indium coming from the SiO_2 layer and ITO substrates.

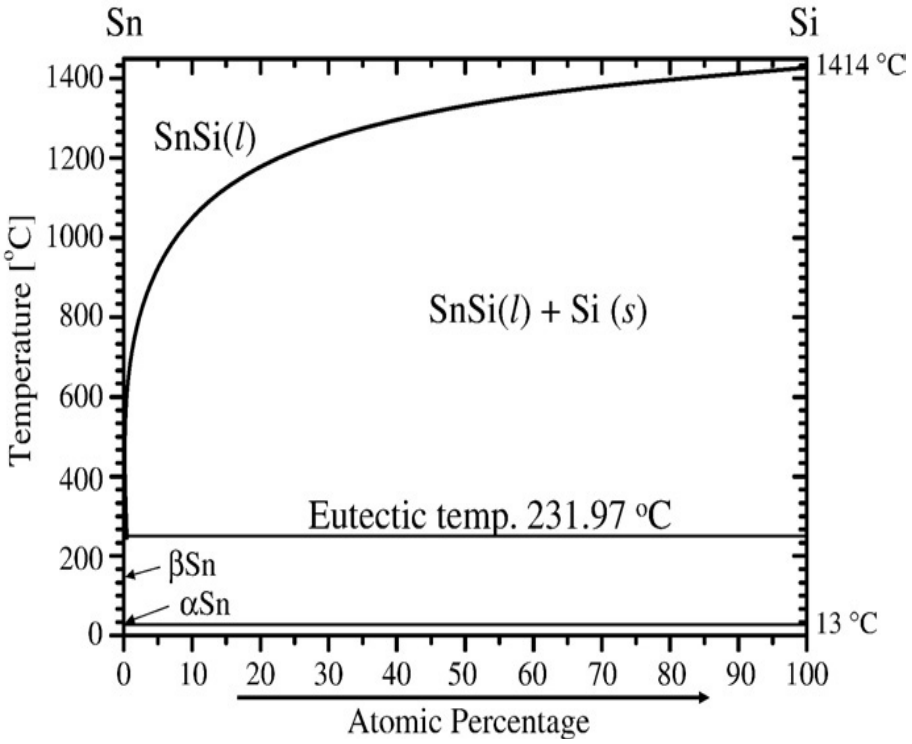

Figure 4.6: The Sn- Si alloy binary phase diagram (Schmidt et al. 2010).

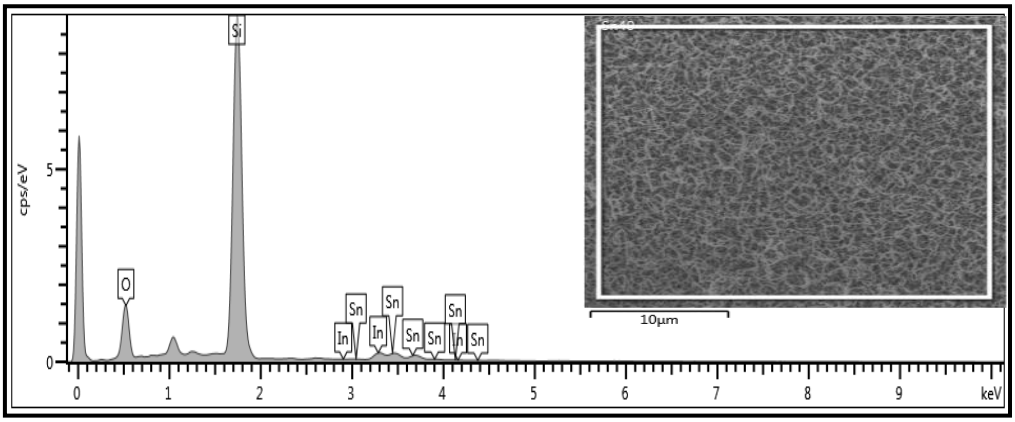

Figure 4.7: EDX spectrum of SiNWs catalyzed using a 40nm thick Sn film.

In most cases of catalyzed growth of NWs, prepared by the VLS mechanism, the diameter of the catalyst droplet (D_c) exceeds the diameter of the nanowire (D_w). The relationship between the radius of the catalyst droplet (R) and the wire radius (r) depends on two parameters, the surface tension of the liquid catalyst (σ_L) and the tension of the liquid/solid interface (σ_{LS}) as shown in the equation below (Schmidt *et al.* 2009):

$$R = r\sqrt{\frac{1}{1-\left(\frac{\sigma_{LS}}{\sigma_L}\right)^2}} \quad , \qquad (4.1)$$

where $R = D_c/2$ and $r = D_w/2$.

Eq. (4.1) can be rewritten as:

$$(\frac{r}{R})^2 = 1-\left(\frac{\sigma_{LS}}{\sigma_L}\right)^2 \qquad (4.2)$$

From Eq.4.2, the wire radius approaches the value of the catalyst radius when the σ_L value is much larger than σ_{LS}. The radius of the Sn catalyst droplets used to produce the silicon nanowires in this work are calculated from SEM images and listed in Table 4.1. The σ_L value of Sn is 0.6 (Schmidt *et al.* 2009), which is more than the σ_L values of Bi, Sb and Pb, but less than those of Ag, Au, and Al (Schmidt *et al.* 2009 ; Goloechen 1992). The liquid/solid interface tension of the grown SiNWs is calculated from Eq. 4.2. The SiNWs prepared with a 10nm catalyst thin film thickness have the biggest σ_{LS} of 0.37 while the wires grown using a 60nm thickness had the lowest σ_{LS} value of 0.11 because the radii of the wires and catalyst are very close (Table 4.1). The contact angle ß is expressed by the following equation (Schmidt *et al.* 2009):

$$\sigma_L \cos(\beta) = -\sigma_{LS} \quad (4.3)$$

Comparing Eq. (4.3) and (4.2), the contact angle between the catalyst metal and the wire surface can be calculated using Eq. 4.4:

$$(\frac{r}{R})^2 = 1-[-\cos(\beta)]^2 = 1-\cos^2(\beta) \quad (4.4)$$

The minimum β value was 101^o for SiNWs catalysed by 60nm thick Sn thin films and the maximum value was 129^o for the wires prepared with 10nm thin film thickness. Figure 4.8 shows the surface tension of the liquid catalyst and the direction of the surface tension at the liquid/solid interface, in addition to the contact angle. At a high substrate temperature, the molten droplets increase in diameter, which leads to the readjustment of the chemical composition of the droplets so that they can cope with the material change at the liquid-solid interface. This process leads to the surface curving out and taking a spherical shape.

The droplets take an ellipsoidal shape, with a radius that is larger than that of the wire, depending on the degree of its stability and surface energy (Mohammad 2009). Moreover, there is some change in the contact angle due to the difference in shape between the droplets on the substrate surface and those on the top of the Si wire. Thus, this transition in droplet shape during the growth process will lead to some expansion of the wire base. However, there is no observed change in the prepared SiNW's diameter along the wire length, which could mean no effective change in droplet shape during the growth process. The average wire density per unit area was calculated from SEM images and found to decrease from 17 to 8 NW/(μm)^2 as the thickness of the catalyst thin films increased from 10 to 100nm (see Table 4.1).

4.2.2 Crystalline Structure

Figure 4.9 shows the XRD patterns of SiNWs prepared using different Sn catalyst thin film thicknesses. All of the XRD patterns show a diffraction peak at an angle of 30.66^{o} corresponding to the ITO-coated glass substrate (Figure 4.9B). The absence of Si diffraction peaks indicated that the samples did not have a crystalline structure. Parlevliet and Jennings (2011) have shown previously that SiNWs synthesized by PPECVD with a Sn catalyst are entirely amorphous. Moreover, SiNWs grown by PECVD using Al as a catalyst on Si at 600^{o}C were also amorphous in structure (Iacopi *et al.* 2007). However, the crystal size of the grown SiNWs could be very small and that makes it difficult to identify them by the XRD method.

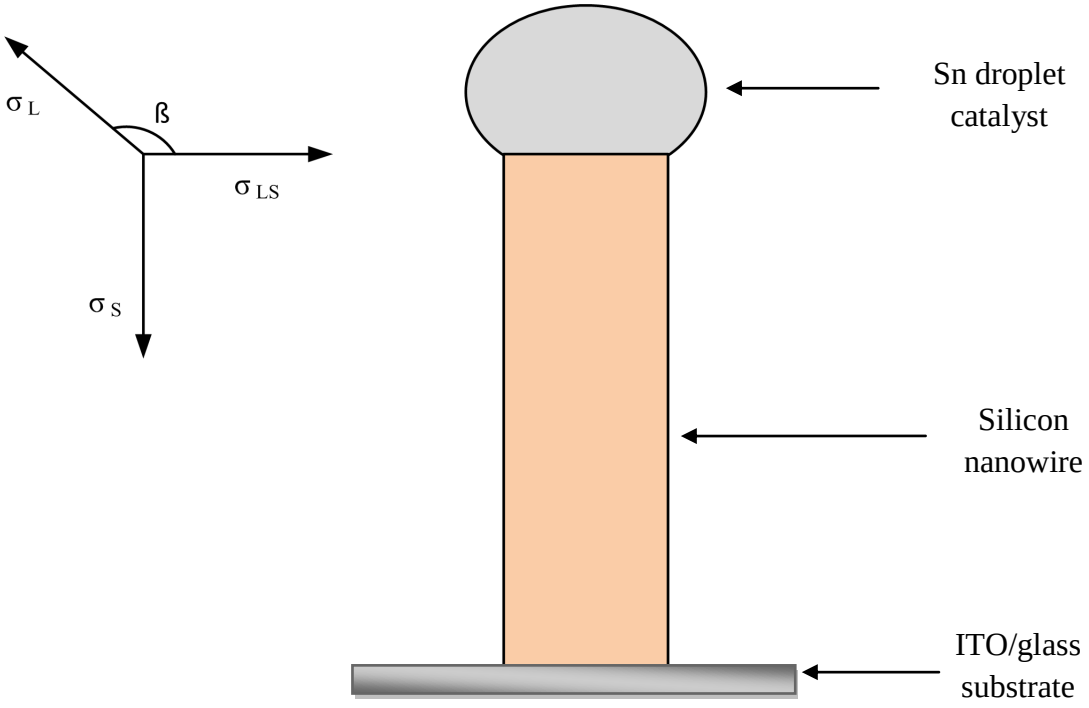

Figure 4.8: Schematic of the surface tension and contact angle of the liquid/wire interface.

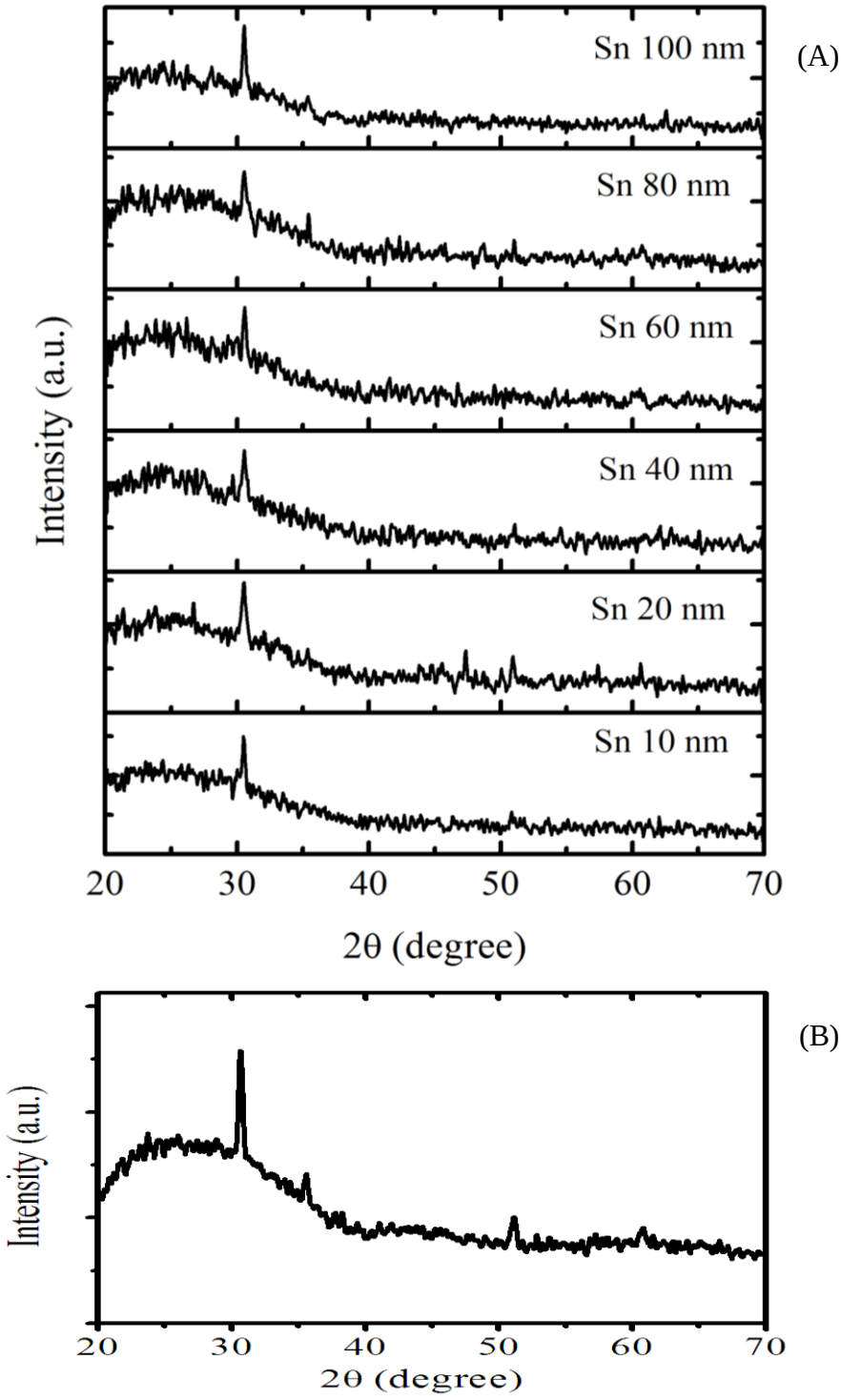

Figure 4.9: XRD patterns of (A) SiNWs prepared using Sn catalyst thin films with thicknesses of 10-100nm, (B) ITO-coated glass substrate.

Table 4.1: The crystal size, diameter, contact angle, surface tension and the density of the grown SiNWs by Sn catalyst.

Sn film thickness (nm)	Average catalyst diameter D_c (nm)	SiNWs diameter D_w (nm)	(D_c/D_w)	Metal/Wire contact angle (ß^o)	Surface tension σ_{LS} (J/m ^{2})	SiNWs density wire/(µm) ^{2}
10	96	75	1.28	129	0.37	17
20	105	95	1.1	115	0.25	15
40	120	105	1.14	119	0.29	13
60	138	135	1.02	101	0.11	11
80	201	185	1.09	113	0.23	8
100	211	195	1.08	112	0.22	8

4.2.3 Optical Properties

4.2.3.1 Photoluminescence Spectra (PL)

PL spectroscopy is a useful optical technique for studying the band gap and it reflects the electronic transition from the excited state to the valence band. PL is a sensitive probe which is used to analyze the structure quality, impurities and defects in nanostructure materials. PL spectra at room temperature of the SiNWs grown using different Sn catalyst thicknesses in the range of 10nm to 100nm are displayed in Figure 4.10. The prepared SiNWs produce red emission bands in the PL spectra. The PL spectra of the SiNWs catalyzed with 10nm Sn thickness produce a broad emission band that peaks at 744nm, while 20nm thick Sn produced two emission bands centered at 747nm and 903nm respectively. In addition, a broad emission band at 742nm was observed in the PL spectra for the NWs catalyzed with 40nm thick Sn. The SiNWs grown using 60nm thick catalyst emitted a band at 608nm that could arise from the

oxide related defects in the surface and oxygen deficiency. Table 4.2 lists the PL emission bands for SiNWs catalyzed by 60, 80 and 100nm thick Sn. The red band was emitted from recombination at the interface between the amorphous sheath layer and the crystalline core (Shi *et al.* 2009). These results agree with other studies that found red PL emission peaks for SiNWs synthesized using Au as a catalyst (Colli *et al.* 2006; Pham *et al.* 2011). Furthermore, specific red PL bands at 744, 747, and 742nm were observed for the SiNWs grown using 10, 20, and 40nm thicknesses of Sn catalyst. These PL bands may originate from the Si–O–Si bridge bonds along the crystalline direction (111) based on the theoretical calculation. This red peak is not observed from other structures such as (110) or (112) SiNWs, implying its dependence on the crystalline configurations (Kang *et al.* 2011). So far, it is not clear whether the nanostructures at the rough SiNW sidewalls are due to the localized nanocrystal-like features surrounded by oxide shells or because of the semilocalized Si structures, which are still connected to the SiNW core by crystalline Si material. The as-grown SiNWs had diameters of 75nm which are relatively large compared with the Bohr radius of the bulk Si. Thus the PL emission cannot be caused by the quantum confinement effect, according to the theoretical prediction of Sanders and Chang (1992). However, the grown SiNWs almost is not single crystal specially when the temperature of preparation is low, thus every wire is contains a small Si crystals. In this case, the explanation of band-gap widening due to quantum confinement is not straight forward. A confined electron-hole pair could easily diffuse into the bulk of the SiNW, thereby losing its confinement-related surplus energy. One would therefore expect PL at the band edge of c-Si to dominate in this case. Band-gap widening is only explainable, here, if one of the charge carriers, e.g., the hole, is trapped at the SiNW surface. Consequently, the other carrier would experience confinement. Confinement surplus energy in this case has to exceed the trapping energy of the hole (50 meV necessary at RT) and the exciton

binding energy (19 meV for c-Si) (Sivakov et al. 2010). The PL spectra of the SiNWs grown using 60nm thickness of Sn show an emission band centered at 608nm. The PL emission in the visible region could be attributed to the oxide related defects in the surface and oxygen deficiency while the second emission is attributed to the quantum confinement effect (Chong *et al.* 2013). Moreover, the quantum confined elemental Si structures of the order of nm and are capped by SiO_2 and emit broad photoluminescence bands from 330 to 470nm for SiNWs fabricated via thermal evaporation of Si monoxide with diameter 20-30nm (Zhao *et al.* 2013). Nevertheless, trapping of holes at the Si/SiOx interface is known to occur and the variety of available crystallographic planes at the rough SiNW surfaces make the trapping of holes at the Si/SiOx interface for SiNWs even more likely than for wafers with low index plane surfaces (Sivakov et al. 2010).

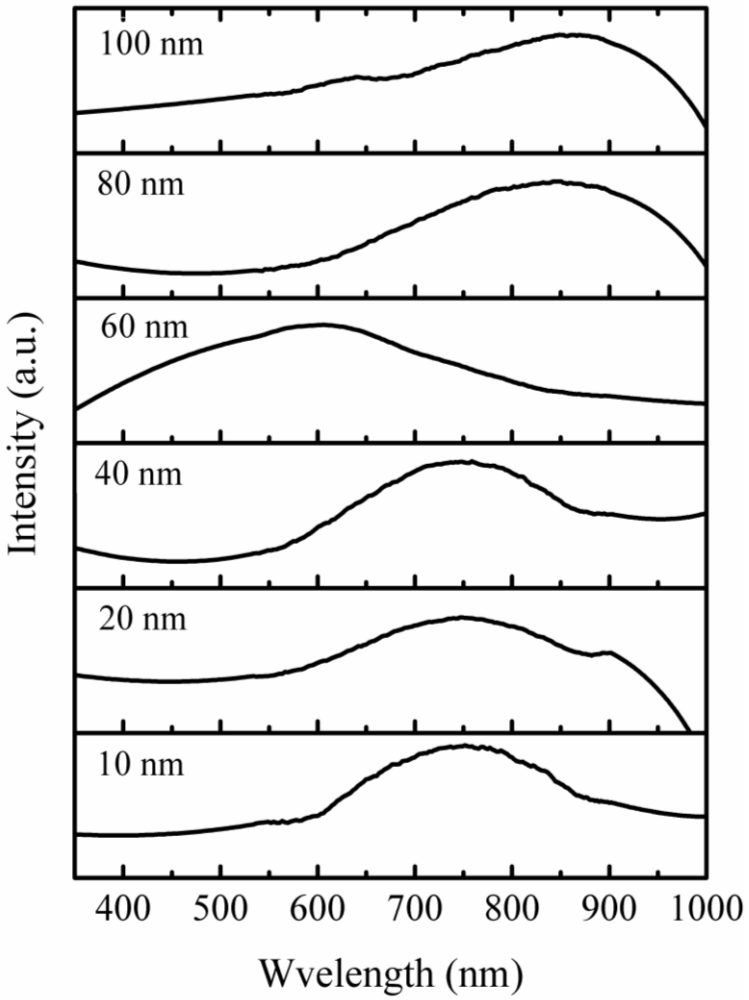

Figure 4.10: Room temperature PL spectra of the SiNWs grown using Sn catalyst layers with thicknesses of (A) 10nm, (B) 20nm, (C) 40nm, (D) 60nm, (E) 80nm and (F) 100nm.

4.2.3.2 Raman spectra

Raman spectroscopy provides much useful information about the material properties. That makes it a standard spectroscopic tool in many scientific areas and specifically to study and characterize semiconductor nanostructures. Raman spectroscopy is a powerful tool for investigating the doping concentration, lattice defect identification, and crystal orientation of materials (Mahdi *et al.* 2012). Raman spectra for SiNWs synthesized using varying thicknesses of Sn catalyst are presented in Figure 4.11. The SiNWs grown using 20nm and 80nm films of Sn exhibit sharp Raman peaks located at 506 and 513cm^{-1} respectively. Comparing with the first order transverse optical mode (1TO) of crystalline Si which appears at 520cm^{-1} (Li *et al*. 2005; Niu *et al*. 2004), the Raman band of the SiNWs catalyzed with 20nm and 80nm Sn films has downshifted by about 14 and 7cm^{-1}, respectively.

In addition, 10, 40 and 60nm thicknesses of Sn catalyst show Raman peaks at 497, 494 and 491cm^{-1}, respectively. Whereas, the Raman spectra for 100nm films of Sn have the peak location at 488cm^{1}. Moreover, all the prepared SiNWs show broad Raman peaks at 290 and 920cm^{-1} which are related to the second order transverse acoustic phonon mode (2TA) and the second order optical phonon mode (2TO), respectively.

The crystallinity, oxidation layer, size uniformity as well as the variation of crystal constants affect the location and curve shape of Raman bands (Niu *et al*. 2004). The red shift of the 1TO Raman peak indicates a decrease in the particle size or reduction in the crystallinity of the sample. Thus, a sharp Raman peak at 519cm^{-1} is related to crystalline Si while the peak at 480cm^{-1} indicates the existence of amorphous Si (Ge *et al.* 2003).

Poinern (2010) used a Sn catalyst with droplets sizes ranging from 85 to 140nm to catalyze SiNWs with estimated diameters of 76 and 86nm via PECVD method. The

Raman spectra of the synthesized SiNWs show a peak at 490cm^{-1}. Meshram *et al.* (2013) show that the Raman spectrum of the SiNWs grown by the hot wire CVD (HWCVD) method using a 300nm thick Sn catalyst present a mixture of amorphous and crystalline phases of Si. Two peaks appear at 480cm^{-1} and 515cm^{-1} which correspond to amorphous and crystalline Si. Moreover, (Pan *et al.* 2005) found a Raman peak at 512cm^{-1} and the spectra tail extended to low frequency due to the defects in the structure of SiNWs grown via the thermal evaporation method (Pan *et al.* 2005). The crystallite size D_r, can be estimated, depending on the value of the shift in TO phonon mode (Yu *et al.* 2009):

$$D_r = 2\pi\sqrt{\frac{B}{\Delta\omega}}, \qquad (4.5)$$

where B is 2.24cm^{-1} nm^2 for Si and $\Delta\omega$ is the shift of the TO peak from the c-Si peak. The crystal size was calculated using Eq.4.5 and listed in Table 4.2. The SiNWs which catalyzed by 20 and 80nm thickness of Sn had large crystal sizes of 2.5 and 3.55nm, respectively, compared with the other prepared samples which used 10, 40, 60 and 100nm thickness of Sn catalyst.

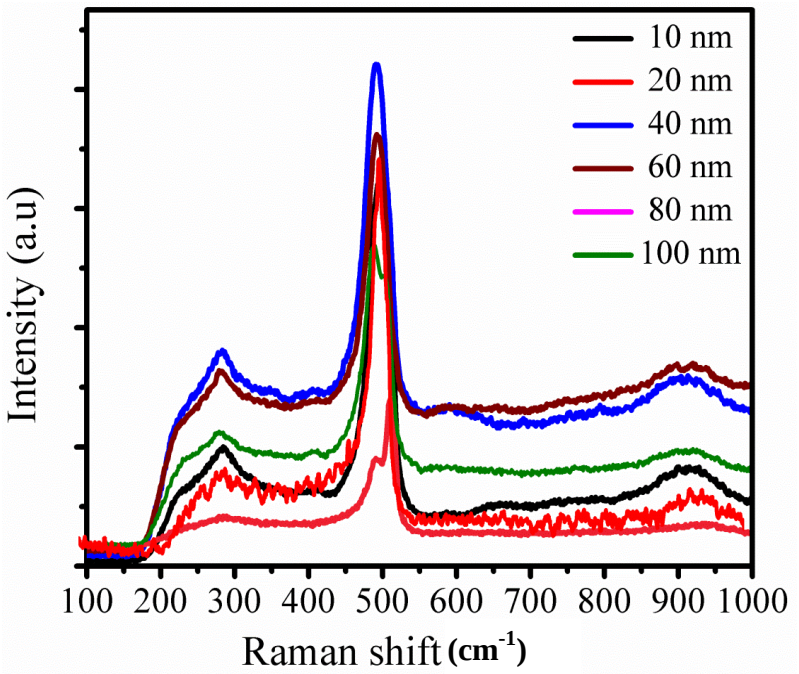

Figure 4.11: Raman spectra of SiNWs prepared using a Sn catalyst with thicknesses in the range of 10nm to100nm.

Table 4.2: Peak locations of the Raman and PL bands for SiNWs grown using different thicknesses of Sn catalyst.

Sn catalyst thickness (nm)	Raman band location (cm^{-1})	PL bands location (nm)	Crystal size D_r (nm)
10	497	744	1.95
20	506	747, 903	2.50
40	494	742	1.85
60	491	608	1.75
80	513	857	3.55
100	488	868	1.60

4.3 Conclusions

SiNWs were successfully synthesized on ITO/glass substrates using the PPECVD method with Sn droplets as catalysts. The SEM images showed that an increase in the thickness of the Sn catalyst thin films resulted in an increased diameter of the SiNWs.

The catalyst film thickness provided good control over the wire diameter, except for a thickness of 10nm. The catalyst thin film thickness of 60nm yielded a close match of the catalyst droplet size to the wire diameter with a value of 1.02. Other parameters, such as metal/wire contact angle and tension of the liquid/solid interface, had lower values when the catalyst thin film thickness of 60nm was used. Thus, the thin film Sn catalyst thickness of 60nm was judged to be optimal for controlling the growth of the wire diameter. Furthermore, the density of the SiNWs decreased from 18 to 8wires/$(\mu m)^2$ as the Sn catalyst thin film thickness increased from 10 to 100nm. XRD spectra of the prepared SiNWs showed the absence of diffraction peaks indicating the low crystallinity or very small particle size of the grown wires. All the prepared SiNWs produce red emission bands in the PL spectra. The PL spectra of the SiNWs catalyzed with 10nm Sn thickness produce a broad emission band that peaks at 744nm, while 20nm thick Sn produced two emission bands centered at 747nm and 903nm respectively. In addition, a broad emission band at 742nm was observed in the PL spectra for the NWs catalyzed with 40nm thick Sn. Due to the quantum size effect, the Raman spectroscopy for the grown SiNWs using 20 and 80nm thick Sn films show sharp peaks with downshifts of about 14 and 7cm^{-1}, respectively compared with the 1TO band of crystal Si. The crystal size that calculated depending Raman spectra showed that the SiNWs catalyzed by 80nm thickness of Sn metal, had the largest particle size of 3.55 nm, while the use of 100 nm thickness of Sn catalyst produced SiNWs with a smaller particle size of 1.6nm.

CHAPTER 5

PREPARATION AND PROPERTIES OF Al-CATALYZED SiNWs

5.1 Introduction

Thin films of the Al catalyst with thicknesses ranging from 10nm to 100nm were deposited on the ITO substrate by thermal evaporation. Then, SiNWs were synthesized via a pulsed plasma-enhanced chemical vapor deposition PPECVD method. This Chapter presents a study of the effect of using of a variety of thicknesses of the Al catalyst in SiNWs growth and explores the effect on the properties of the prepared SiNWs. The surface morphology and structure properties are reported. The photoluminescence (PL) and Raman spectra are also discussed. The surface morphology of the products was studied by FESEM and TEM images. The crystalline structure of the prepared SiNWs was investigated through x-ray diffraction (XRD) and the optical properties were measured at room temperature.

5. 2 Synthesis of SiNWs catalyzed by Al

5.2.1 Surface morphology

The surface morphology of the SiNWs, prepared using the Al catalyst, with different thin-film thicknesses of 10nm to 100nm, was analyzed through FESEM images (Figure 5.1). The SiNWs were significantly affected by the varying thicknesses of the thin-film catalyst. The SiNWs prepared using Al with thicknesses of 10 and 20nm were characterized by a high wire density, as shown in Figures 5.1A and 5.1B.

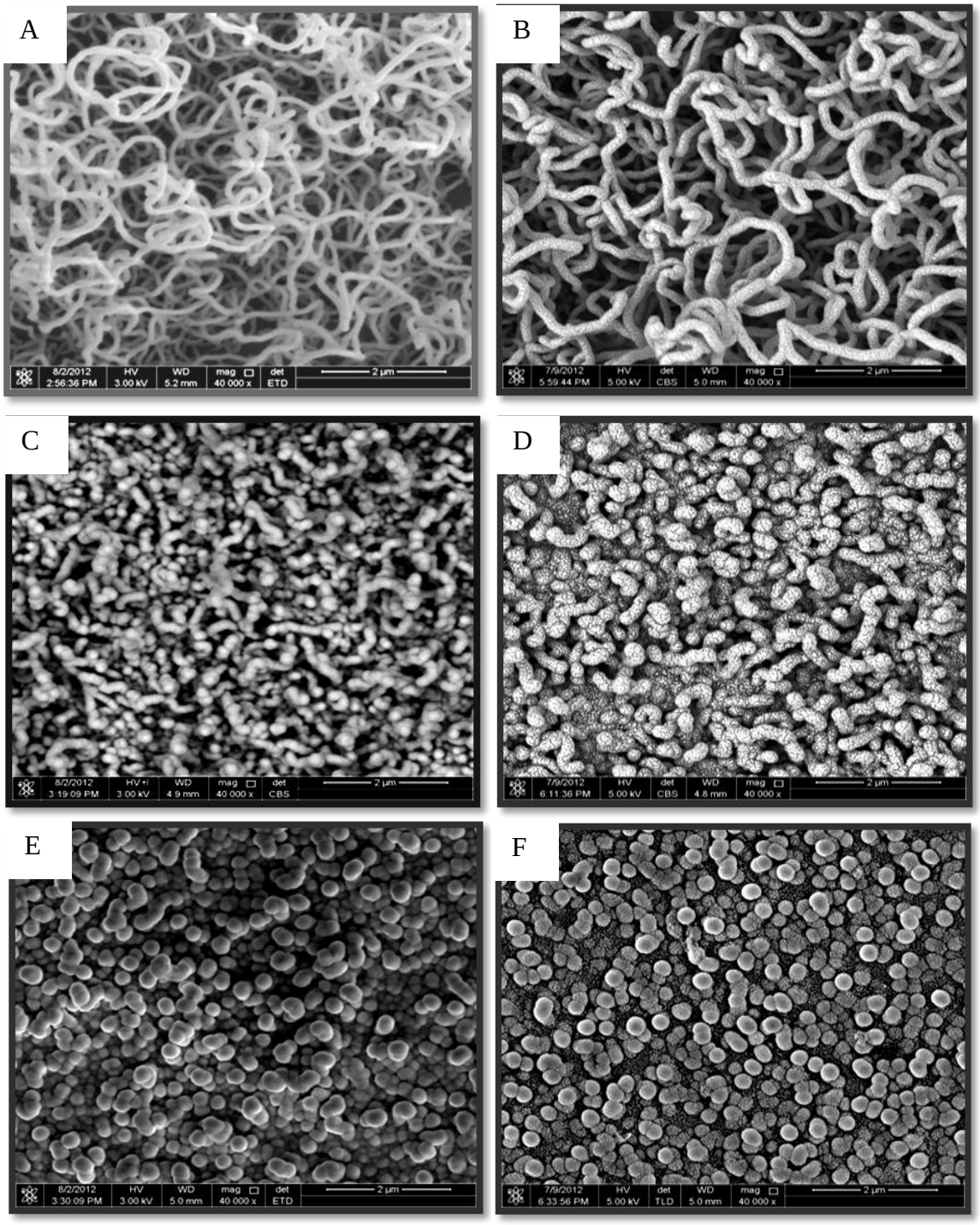

Figure 5.1: FESEM images for SiNWs prepared using Al catalyst thicknesses of (A) 10nm, (B) 20nm, (C) 40nm, (D) 60nm, (E) 80nm and (F) 100nm.

The nanowires became shorter in length and tended to aggregate when the Al thickness increased to 40 and 60nm (Figures 5. 1C and 5.1D). Moreover, an 80nm Al catalyst thickness resulted in the growth of short, aligned wires, as shown in the FESEM image in Figure 5.1E. Small, circular types of particles were observed with a catalyst thickness of 100nm, as shown in Figure 5.1F. Figure 5.2 shows the analysis of the diameter distributions of the SiNWs grown using different Al thin-film thicknesses. The modal wire diameter significantly increased when the Al thin-film thickness was increased. About 100-120 wires on average were selected randomly to determine the diameter distribution of the grown SiNWs with an error ratio about ±5%.The wire diameters of the SiNWs prepared using 10 and 20nm thick Al thin films ranged from 100nm to 160nm and from 110nm to 170nm, respectively (Figures 5.2A and 5.2B). The modal diameters of the SiNWs catalyzed by layer thicknesses of 10 and 20nm of Al were about 115 and 125nm, respectively.

As shown in the FESEM images, the grown wires became shorter with increased diameter as the catalyst film thickness increased. Thus, the SiNWs catalyzed by 40 and 60nm thick Al films, showed diameters ranging from 150nm to 210nm and 180nm to 240nm, respectively (Figures 5.2C and 5.2D). Using an 80nm Al catalyst thickness led to the formation of SiNWs with diameters reaching 270nm (Figure 5.2E). Furthermore, short wires with diameters ranging from 60nm to 100nm were also noticed in the sample which was prepared using the 80nm thick Al catalyst. The reason for the appearance of these wires with such a small diameter is unknown. The maximum diameter of the grown SiNWs increased to about 300nm as the Al catalyst thickness reached 100nm (Figure 5. 2F).

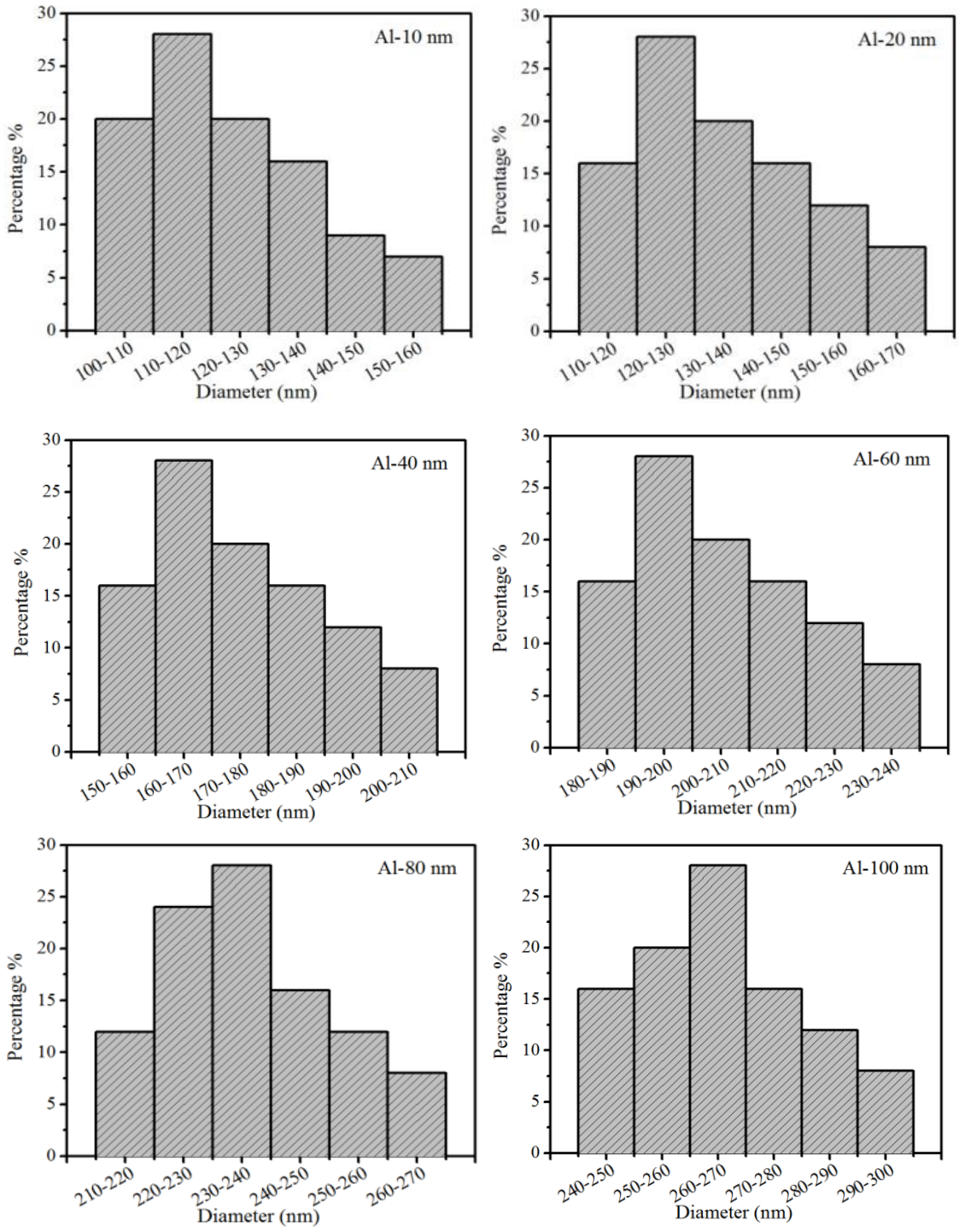

Figure 5.2: Diameter distribution of the SiNWs grown using an Al catalyst with various thin film thicknesses from 10-100nm.

From the FESEM images, the density (number of nanowires per μm^2) of SiNWs grown using the Al catalyst was measured and found to decrease from 20NW/μm^2 to 10NW/μm^2 when the Al catalyst thickness increased from 10nm to 100nm, respectively as shown in Figure 5.3. Figure 5.4 shows the cross-sectional FESEM of SiNWs synthesized using 20, 60 and 100nm Al catalyst thickness. The average length of the SiNWs catalyzed by a 20nm layer of Al ranged from 2 to 2.5μm and decreased when the thickness of the Al catalyst thin films increased. Moreover, short aligned wires are observed for SiNWs grown with an 80nm thick layer of Al catalyst.

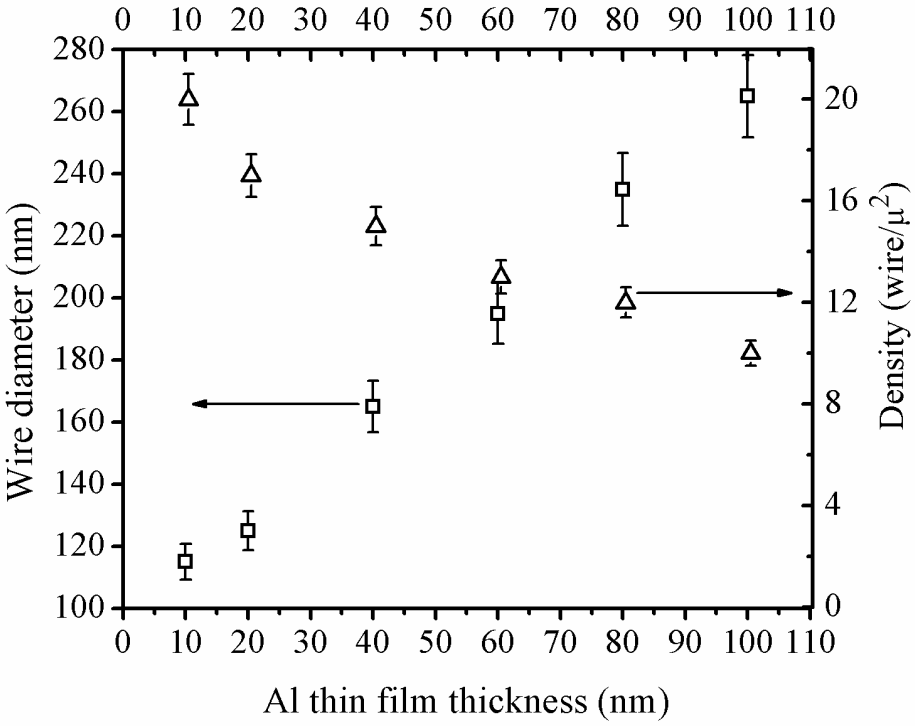

Figure 5.3: The catalyst thin film thickness vs. wire diameter and density.

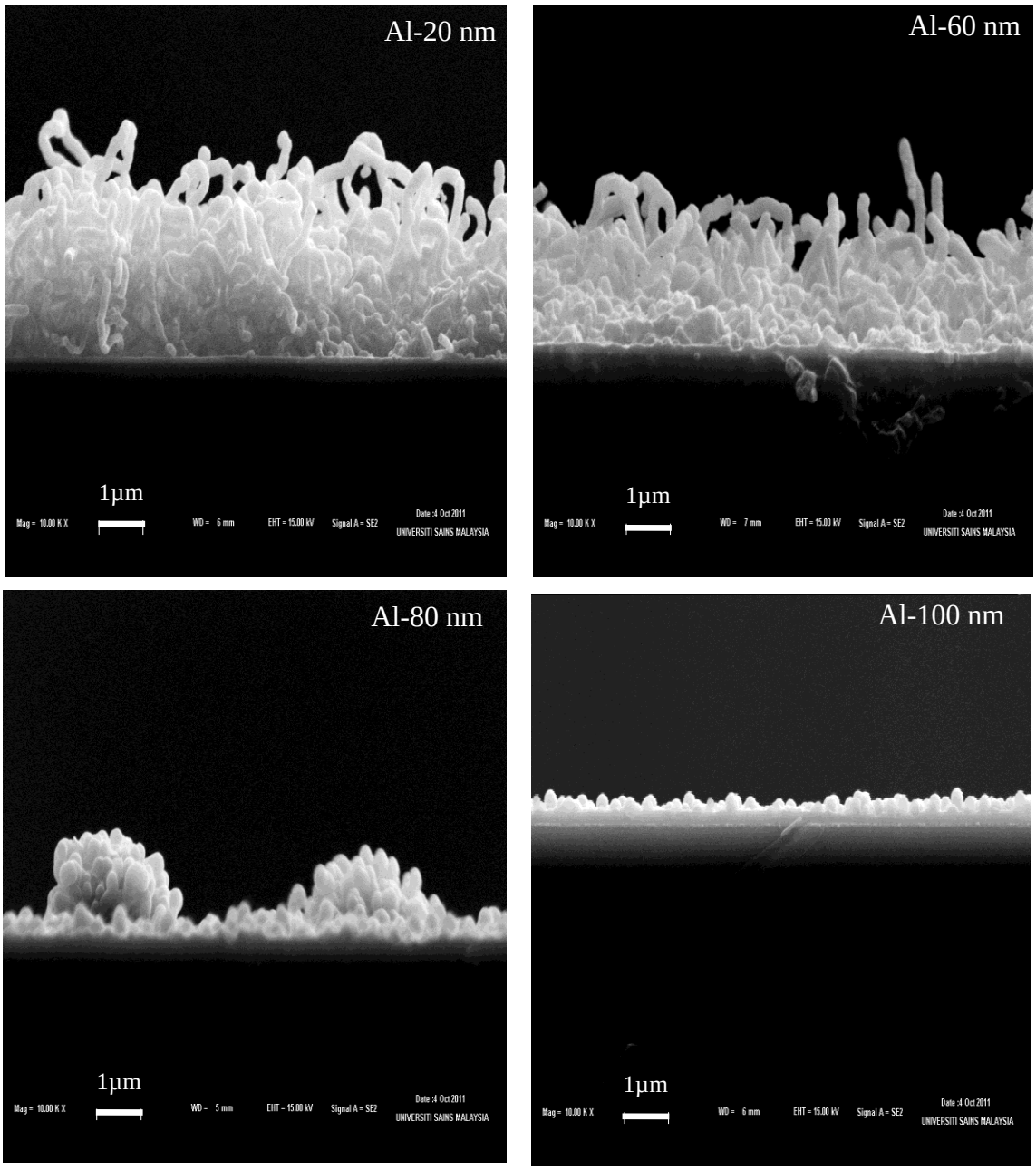

Figure 5.4: Cross-sectional images for SiNWs synthesized using Al catalyst thickness of (A) 20nm, (B) 60nm, (C) 80nm and (D) 100nm.

The liquid/solid interfacial tensions (σ_{LS}) of Al/Si for the SiNW catalyst with various Al thicknesses are calculated via Eq (4.2) and listed in Table 5.1. Where the liquid surface tension (σ_L) value of Al is 0.8 (Nebol'sin and Shchetinin 2003). Also, the Al catalyst diameter (D_c) that were used to synthesize the SiNWs are measured from

FESEM images. The SiNWs grown with 10nm Al thick have the biggest σ_{LS} value about 0.46, while the σ_{LS} value for SiNWs catalyzed using 80 and 100nm Al thick was zero. The contact angle β was also calculated from Eq. 4.4 (see Table 5.1), the NWs catalyzed with 10nm Al thick have the maximum β value of 125.5^{O} while the NWs catalyzed using 60nm Al thick show the minimum β value of 78.2^{O}.

Table 5.1: The diameter, contact angle and surface tension of the grown SiNWs by Al catalyst.

Al catalyst thickness (nm)	Al catalyst average diameter D_c (nm)	Diameter of SiNWs D_w (nm)	D_c/D_w	Metal/Wire contact angle ß ^{O}	Surface tension σ_{LS} (J/m^2)
10	99	115	0.86	125.5	0.46
20	136	125	1.08	66.8	0.31
40	166	165	~1.0	84	0.083
60	199	195	1.02	78.2	0.16
80	235	235	1.0	90	0
100	265	265	1.0	90	0

TEM images of the samples prepared using Al films of 20, 60, 80 and 100nm thickness are shown in Figure 5. 5. These show that the aspect ratio of the grown SiNWs decreased as the catalyst thickness increased. Moreover, the grown SiNWs were relatively short when the 80nm Al catalyst was used, compared with the wires grown using thinner Al films. In addition, the TEM image shows that the SiNWs, prepared using an Al film of 100nm thickness, consist of small circular particles which supports the observations of the FESEM image (see Figure 5.1F).

.

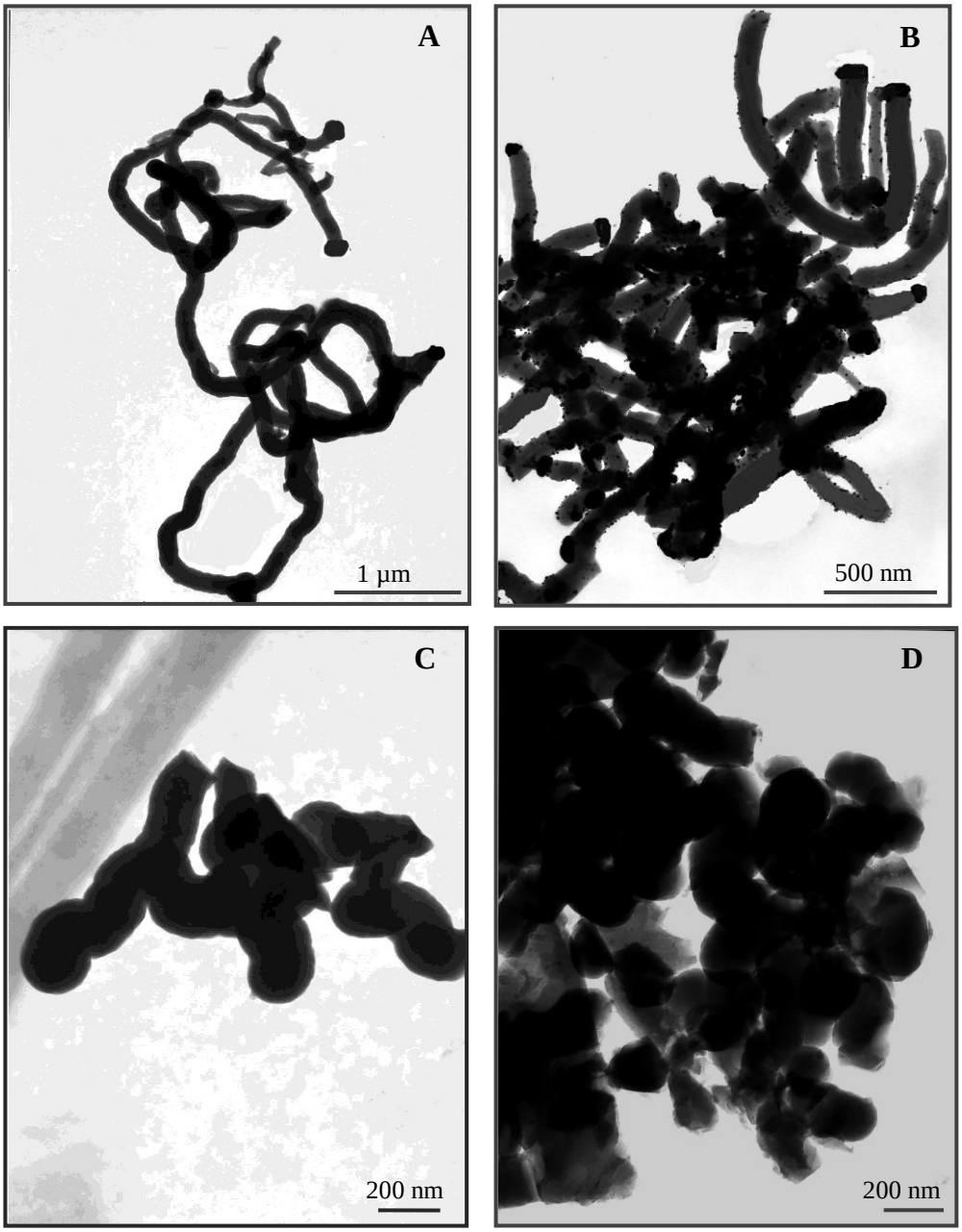

Figure 5.5: TEM images of SiNWs prepared by Al catalyst thin films with thicknesses of (A) 20nm, (B) 60nm, (C) 80nm and (D) 100nm.

The eutectic point of the Al-Si system at 577°C was at a low Si concentration of 12.6% (Schmidt *et al.* 2009; Massalski *et al.* 1998), as shown in the Al-Si phase diagram in Figure 5. 6. Two solid phases can be noted as the α and β regions in the Al-Si phase diagram. Thus, depending on the growth temperature, two different growth

mechanisms are possible when using Al metal to catalyze SiNWs, namely, VLS and VSS. In the VLS mechanism, the growth temperature should be higher than the eutectic point. Thus the growth temperature has to be higher than the eutectic temperature of 577^{o}C so that the Al–Si catalyst particle is a liquid (Wang *et a.l* 2006; Iacopi *et al.* 2007).

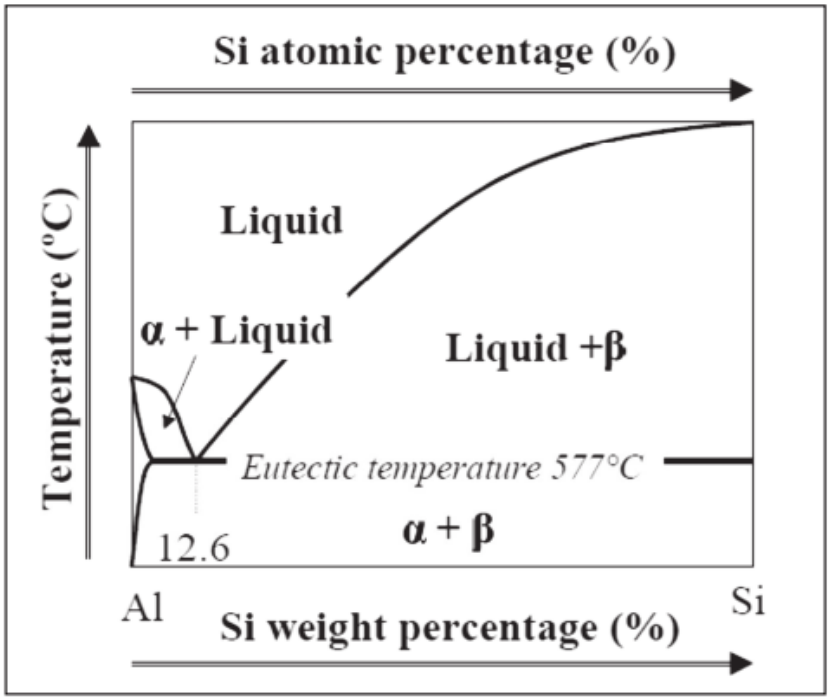

Figure 5.6: The Al- Si alloy binary phase diagram (Schmidt *et al.* 2009)

The growth temperature of SiNWs was 400°C and less than the eutectic point of Al-Si, which means that the growth mechanism was VSS. The SiNWs grown via the VSS mechanism bring two benefits: reducing the growth temperature and reducing the solubility of Si in the catalyst to about one order of magnitude. Wang *et al*. (2006) also synthesized SiNWs by the CVD method using Al as a catalyst at temperatures between 430°C and 490°C (below the Al-Si eutectic point), indicating that their SiNWs were grown via the VSS mechanism.

However, SiNWs were also grown via the VLS mechanism by Schmidt *et al.* (2009) using an Al catalyst at temperatures between 580°C and 700°C. The VSS growth mechanism has been reported for the growth of SiNWs using other catalysts such as Ti (Kamis *et al.* 2000).

Our results are in accordance with those presented by Wacaser *et al.* (2009), who showed that varying Al layer thicknesses have an influence on the average SiNW diameter. The average diameters of the SiNWs grown by the low pressure chemical vapor deposition (LPCVD) method using Al thicknesses of 3, 5 and 7nm increased to 58, 78 and 83nm, respectively. Moreover, the diameter of SiNWs, prepared with 6nm thick Al, ranged between 20nm and 100nm, and increased to about 100 - 120nm with a 10nm thick Al thin film (ChoiI *et al.* 2011).

Other studies also found that an increase in the catalyst thickness led to an increase in the diameters of the SiNWs (Cui *et al.* 2001; Fukata *et al*. 2005). Figure 5.7 shows the EDX spectra of a SiNW sample that was catalyzed by using a 40nm Al thin film thickness. The atomic ratio of Al metal in the sample was 2.81% while it was of 12.3% in the tip of a single SiNW. Moreover, the atomic ratio of Si in the tip was 72.7%. The EDX results confirmed that the SiNWs were catalyzed by Al metal.

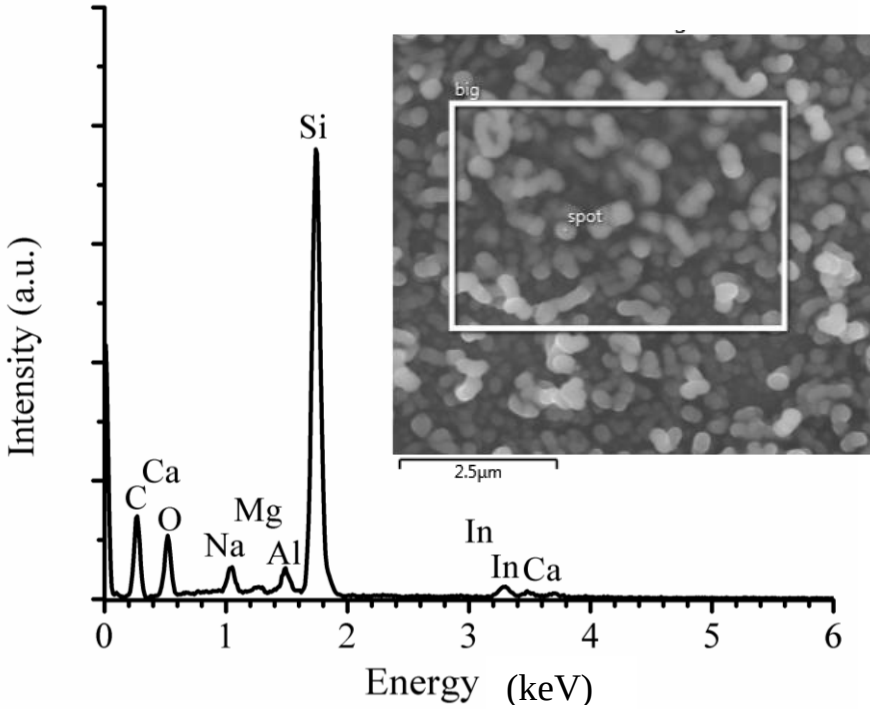

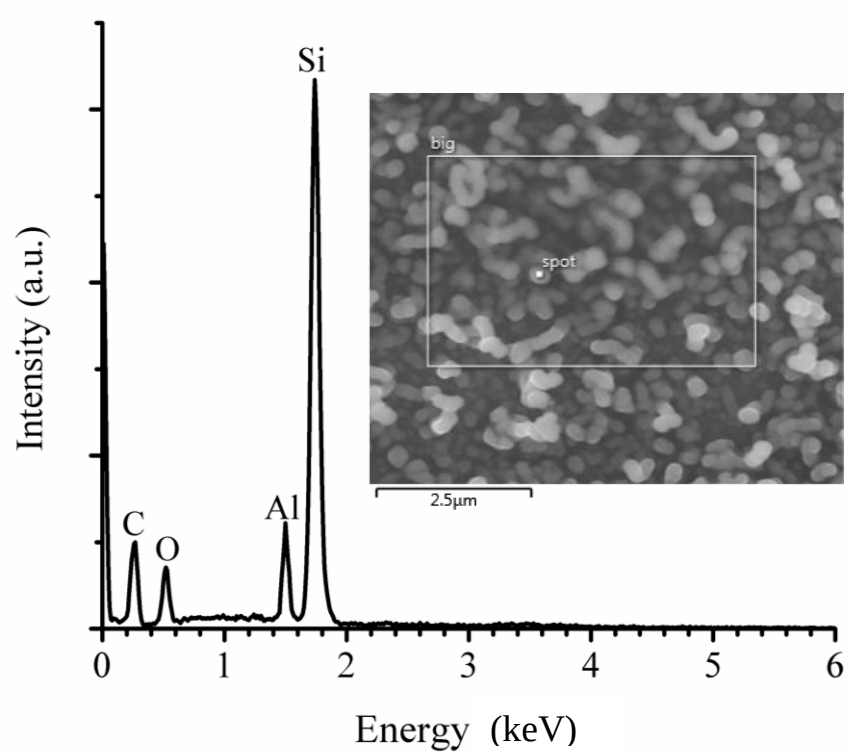

Figure 5.7: EDX spectra of SiNWs catalyzed using 40 nm Al measured at (A) wide area of the sample and (B) on the tip of the NW.

5.2.2 Crystalline Structure

The XRD patterns of SiNWs synthesized using various Al thin film thicknesses are shown in Figure 5.8. The diffraction peak at 30.4° is related to the (200) plane of the ITO coated glass substrate and it appeared conspicuously in the samples prepared using Al thin film thicknesses of 10, 20, 40 and 60nm. The ITO peak became weaker in the SiNWs grown using 80 and 100nm thick Al films. This could be because of the increase in the wire diameters of these samples and the greater Al thickness that covered the substrates as shown in cross sectional FESEM images in Figure 5.4. The Al diffraction peak was located at ~35° corresponding to the (110) plane of Al. This appeared clearly in the XRD patterns of the SiNWs prepared with 80 and 100nm thick Al films. This peak was weaker in the other samples catalyzed by 10, 20 and 40nm thick Al films. The strong peak at 24^{o}, for the 100nm thick Al film, may be due to SiO_2. Moreover, other diffraction peaks related to the (111), (200), and (222) planes of Al metal at 38.5^{o}, 44.8° and 65°, respectively, were observed in some of the XRD patterns.

The diffraction peaks corresponding to the crystalline Si phase which should occur around 28.5^{o}, were absent, indicating that the prepared SiNWs had low crystallinity or amorphous structure. Iacopi *et al.* (2007) used 10 nm Al particles, prepared via a PVD method, to grow SiNWs by PECVD. They found that the Si layer that covered the catalyst is amorphous. Moreover, the SiNWs synthesized by pulsed PECVD with a Sn catalyst were entirely amorphous (Parlevliet and Jennings 2011).

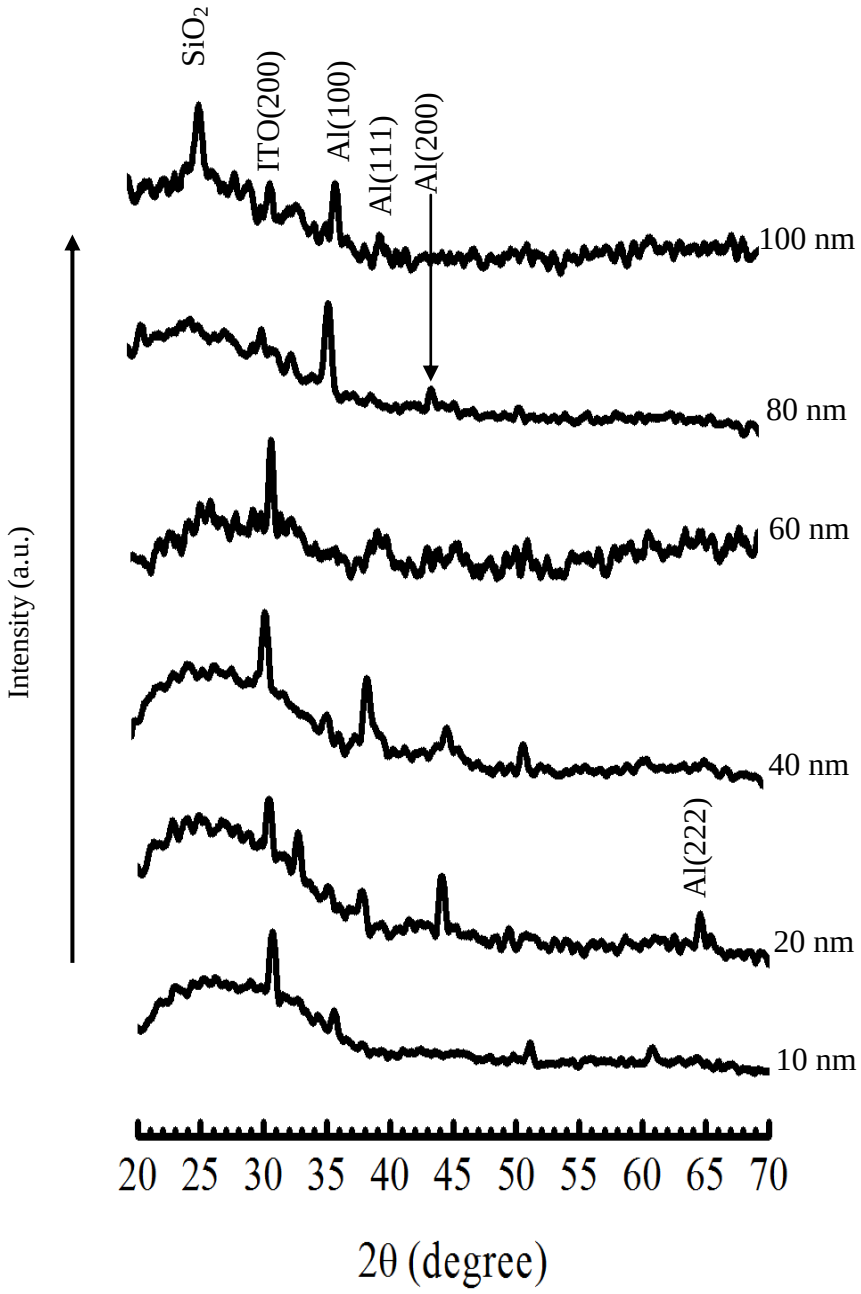

Figure 5.8: XRD patterns of the SiNWs grown using an Al catalyst with various thin film thicknesses from 10-100nm.

5.2.3 Optical Properties

5.2.3.1 Photoluminescence spectra (PL)

The room temperature photoluminescence (PL) spectra of the grown SiNWs catalyzed by various Al thin-film thicknesses of between 10nm to 100nm are shown in Figure 5.9. These SiNWs showed three types of emissions: green, blue, and red bands. The SiNWs prepared using a 10nm thick Al catalyst film showed a broad red peak at about 770nm. Two broad emission bands, located at 751 and 900nm, were observed in the PL spectrum of the SiNWs catalyzed with 20nm thick Al. The PL emission from the SiNWs catalyzed by a 40nm thick Al film also contained two broad peaks at 782 and 900nm as well as a weak blue emission at around 500nm. The PL emission bands for the other samples prepared using Al catalysts with thicknesses of 60, 80 and 100 nm are shown in Figure 5.9 and listed in Table 5.2.

The Bohr radius of the free exciton of the bulk silicon was around 5nm (Megouda 2009), and all prepared SiNWs had a diameters of more than 100nm. Thus, the observed PL emission cannot be ascribed to the quantum confinement effect in the nanowires. The SiNWs grown using 60, 80, and 100nm thickness of Al catalyst emitted green bands at 540nm which could have come from the recombination of free electrons with the oxygen defect in the silicon oxide layer which coated the SiNWs. All prepared samples showed red PL band ranging from 700nm to 782nm emitted from recombination at the interface between the amorphous sheath layer and the crystalline core (Qi 2003; Shi 2009). However, the absence of XRD peaks does not mean that the SiNWs had completely amorphous structure. They could have had a very low degree of crystallinity. Bhattacharya *et al.* (2004) prepared SiNWs by pulsed laser vaporization of silicon using Au as a catalyst and found that red PL emissions peaked at 1.5eV (826nm) and 1.4eV (886nm) for different diameter distributions.

De Boer *et al.* (2010) noticed an increase in PL intensity for Si nanocrystals and shifts to longer wavelengths for small-sized nanocrystals. Our results are in agreement with other studies that synthesized SiNWs using Au as a catalyst and obtained red emission peaks (Colli *et al.* 2006; Wu *et al.* 1996). Moreover, the blue PL could have come from the Si-rich oxides including very small molecular-like Si clusters in the silicon oxides shells which supports the hypothesis that violet/blue PL originates from the SiOx amorphous matrix covering the c-SiNW core (Zhao et al 2013). On the other hand, the shape and intensity of the PL spectra confirm that the emission bands cannot correspond to the SiNWs core where the intensity of the c-Si should be high (Ma et al. 2008).

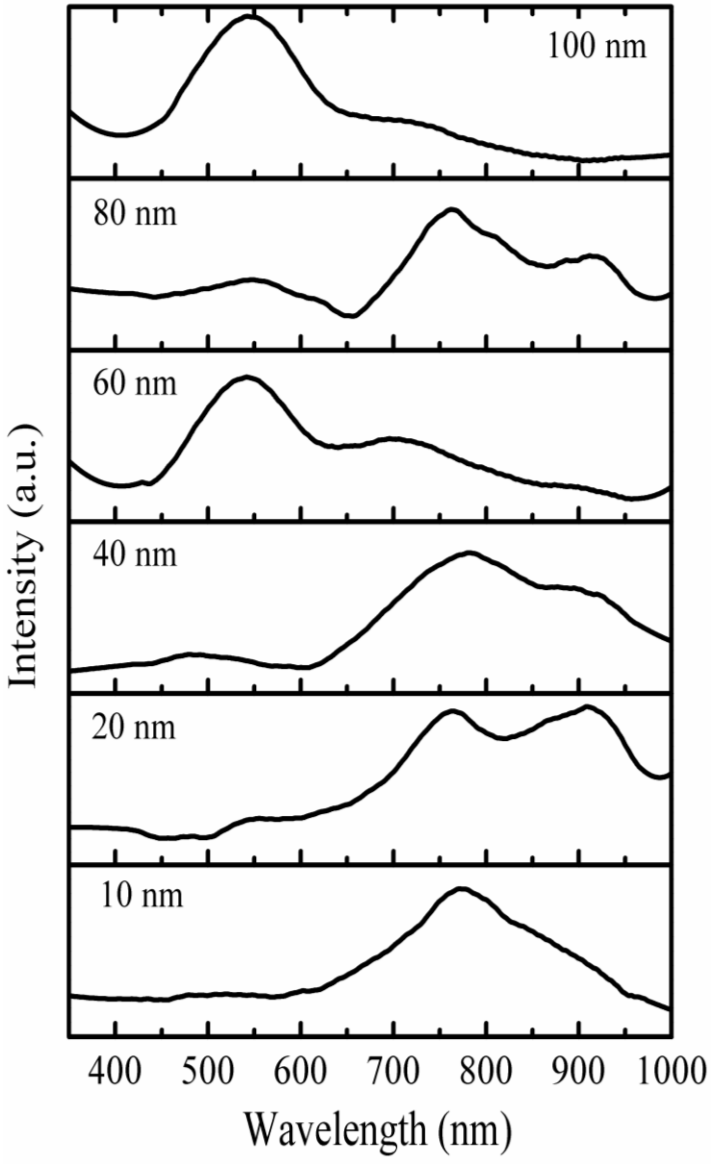

Figure 5.9: Room temperature PL spectra of the SiNWs grown using an Al catalyst with various thin film thicknesses from 10-100nm.

5.2.3.2 Raman spectra

Micro-Raman spectroscopy is an analytical tool that provides information about doping concentration, lattice defect identification, and crystal orientation of nanostructured materials via the effect of phonon confinement (Mahdi *et al.* 2012; Wu *et al.* 1996).

The micro-Raman spectra of SiNWs synthesized using an Al catalyst are shown in Figure 5.10. The SiNWs catalyzed by Al thin films with thicknesses of 10, 20, 40 and 60nm showed Raman peaks located at 500, 498, 495 and 493cm^{-1}, respectively, corresponding to the first order transverse optical mode (1TO) of c-Si. Compared with the 1TO peak for c-Si, which is located at 520cm^{-1} (Liu *et al.* 2001), all the prepared SiNWs 1TO peaks were shifted toward lower frequencies.

A broad Raman peak was observed at 484cm^{-1} for the SiNWs prepared using 100nm thick Al catalyst. The peak location and shape indicate that the wires were amorphous (Gajovic *et al.* 2008) and the broadening of this peak is indicative of oxidation. The SiNWs prepared using an 80nm thick Al catalyst show a 1TO Raman band centered at 511cm^{-1}, shifted from the c-Si band by about 11cm^{-1}. The located 1TO band nearest to the c-Si band could be due to the wires which had a small diameter which appeared in this sample as shown in the FESEM image in Figure 5.1E. The broad peaks at 290 and 920cm^{-1} were related to the second order transverse acoustic phonon mode (2TA) and to the second order transverse optical phonon mode (2TO), respectively (Li *et al.* 1999).

Campbell and Fauchet (1984) proposed a model of phonon confinement to estimate the relationship between the Raman shift and the nanoparticle size. The decreases in the diameter of the Si nanospheres led to the shift in the 1TO peak toward the lower wave number.

Qin *et al.* (2011) noted that an a-Si layer covered the c-Si core of the SiNWs prepared by inductively coupled PCVD using Au as a catalyst and concluded that the broad Raman peak at 480cm^{-1} corresponded to this amorphous Si layer. Moreover, they found that the amorphous layer thickness increased as the SiNW diameter increased due to using a thicker catalyst. The crystal size was calculated from Eq. 4.5 and listed in Table 5.2.

It shows that the wires catalysed with 80nm thickness of Al metal had a larger crystal size of about 3.13nm compared with the other samples which were prepared using various thickness of Al catalyst. Individual SiNWs grown by CVD using 10nm thick Al catalysts had diameters ranging from 50nm to 500nm. The micro-Raman spectra were taken at the nanowire tip and at the nanowire base, which both showed a sharp peak at 518cm^{-1}, while the spectra near the base showed another broad peak at around 475cm^{-1} (Kohen *et al.* 2012).

The Raman band location and curve shape depended on the crystallinity, oxidation layer, size uniformity, and on the variation of crystal constants (Niu *et al.* 2006). The shift in the 1TO peak towards lower frequencies could be caused by the decrease in the crystallinity of SiNWs when the wire diameter increased, except for the sample prepared by 80nm thick Al. From the FESEM image, the SiNWs prepared by the 80nm thick Al were vertically aligned, which could be the reason the 1TO peak appeared nearest to the c-Si location. The enhancement of the crystallinity of SiNWs required a high preparation temperature.

Ho *et al.* (2012) grew SiNWs by the CVD method at 850°C using Au as a catalyst and obtained a single crystal structure with vertical alignment. The 1TO Raman peak was strong and centered at 520cm^{-1}. The SiNWs prepared at lower temperatures resulted in structures with lower crystallinity.

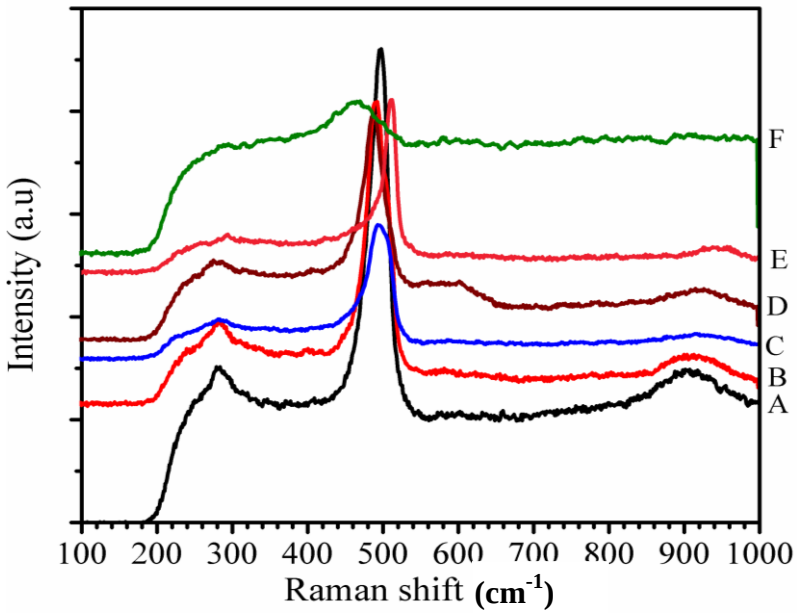

Figure 5.10: Raman spectra of SiNWs prepared using an Al catalyst with thickness of (A) 10nm, (B) 20nm, (C) 40nm, (D) 60nm, (E) 80nm and (F) 100nm.

Table 5.2: Peak locations of Raman and PL bands for SiNWs grown with Al thin film catalysts of different thicknesses.

Catalyst thickness (nm)	Raman band cm^{-1}	PL bands (nm)			Crystal size D_r (nm)
		Blue	Green	Red	
10	500	-		770	2.10
20	495	-	-	751,900	1.87
40	493	-	500 (weak)	782,900	1.8
60	490	-	540	700	1.71
80	511	-	540	770	3.13
100	484	-	540	700 (weak)	1.56

5.3 Conclusions

SiNWs were grown via the pulsed PECVD method using varying thicknesses of the Al catalyst ranging from 10nm to 100nm. Increasing the Al thin-film thickness has a strong effect on the morphology and dimensions of the grown wires. The wire diameter increased from 115nm to 265nm as the catalyst thin film thickness increased from 10nm to 100 nm, resulting in the reduction of the density of the SiNWs from 20μm^2 to 10μm^2. No diffraction peaks related to Si structure were observed in the XRD patterns, indicating the low crystallinity of the prepared wires. The PL spectra of the SiNWs prepared with various Al thicknesses showed emission bands in the green, blue and red regions corresponding to recombination from the oxygen defect in the coated silicon oxide layer and from the interface between the amorphous layer and the crystalline core.

Raman spectra confirmed that the crystallinity of SiNWs decreased as the catalyst thickness increased because the first order transverse band moved further away from the c-Si band location. The SiNWs catalyzed using 80nm thick Al produced a 1TO Raman band nearest to c-Si because the wires were vertically aligned. However, for SiNWs catalyzed by 100nm thick Al, the 1TO Raman peak was found near the a-Si location. The crystal size that were calculated from the Raman spectra showed that the SiNWs catalyzed by 80nm thickness of Al metal had the greatest particle size of 3.13 nm while using 100 nm thickness of Al catalyst produced SiNWs with a lesser particle size of 1.56nm.

CHAPTER 6
PREPARATION AND PROPERTIES OF Au-CATALYZED SiNWs

6.1 Introduction

This Chapter describes how silicon nanowires (SiNWs) were grown on indium tin oxide-coated glass substrates using a PPECVD method with gold (Au) as a catalyst. Various thicknesses of Au thin films ranging from 10nm to 100nm were deposited on the substrates by thermal evaporation. The crystalline structure, surface morphology, and the optical properties of the synthesized SiNWs were investigated. The effect of the catalyst thickness on the NWs growth and properties are described in this Chapter. The surface morphology of the grown SiNWs was investigated by FESEM and TEM. The crystalline structure of the prepared SiNWs was investigated through (XRD) and the photoluminescence (PL) and Raman spectra were recorded.

6.2 Synthesis of SiNWs Catalyzed by Au Metal

6.2.1 Surface Morphology

Figure 6.1 illustrates the FESEM images of SiNWs prepared using various thicknesses of Au thin films ranging from 10nm to 100nm. Homogeneous and long SiNWs were formed when 10 and 20nm thick Au films were used (Figures 6. 1A and 6.1B), similar to the SiNWs grown using 40 and 60nm thick Au with increasing wire diameter (Figures 6.1C and 6.1D). By contrast, SiNWs catalyzed with 80 and 100nm thick Au films demonstrated some kinking or worm-like structures, especially those with 100nm thickness (Figures 6. 1E and 6.1F).

Figure 6.2 shows the diameter distribution of the synthesized SiNWs with an estimated error ratio of about ±5%. The diameters of the SiNWs catalyzed using 10 and 20nm thick Au ranged from 40nm to 100nm and 80nm to 140nm, respectively (Figures 6.2A and 6.2B). The increase in catalyst film thickness clearly led to an increase in the diameter of the SiNWs. The SiNWs catalyzed using 100nm thick Au exhibited diameters ranging from 160nm to 220nm (Figure 6.2F). Cui *et al.* (2003) synthesized SiNWs via CVD at approximately 440°C using different Au thicknesses. They observed that an increase in the catalyst thickness from 5nm to 30nm resulted in an increase in the modal SiNW diameter from 6nm to 31nm. Moreover, Hofmann *et al.* (2003) used PECVD to grow SiNWs on Si wafers at 400°C using different thicknesses of Au. They found that the modal wire diameter increased from 29nm to 300nm when the Au thickness was increased from 0.5nm to 5nm.

Furthermore, Qin *et al.* (2011) demonstrated that the diameter of SiNWs prepared via inductively coupled PCVD on Si wafers at 380°C using 16nm thick Au ranged from 90nm to 130nm and increased to 130nm to 175nm with a 40nm thick Au catalyst, in agreement with our results. Al-Taay et al. (2013a) (as Chapter 4) found that the diameter of SiNWs grown by PPECVD using a Sn catalyst also increased as the catalyst thin film thickness increased.

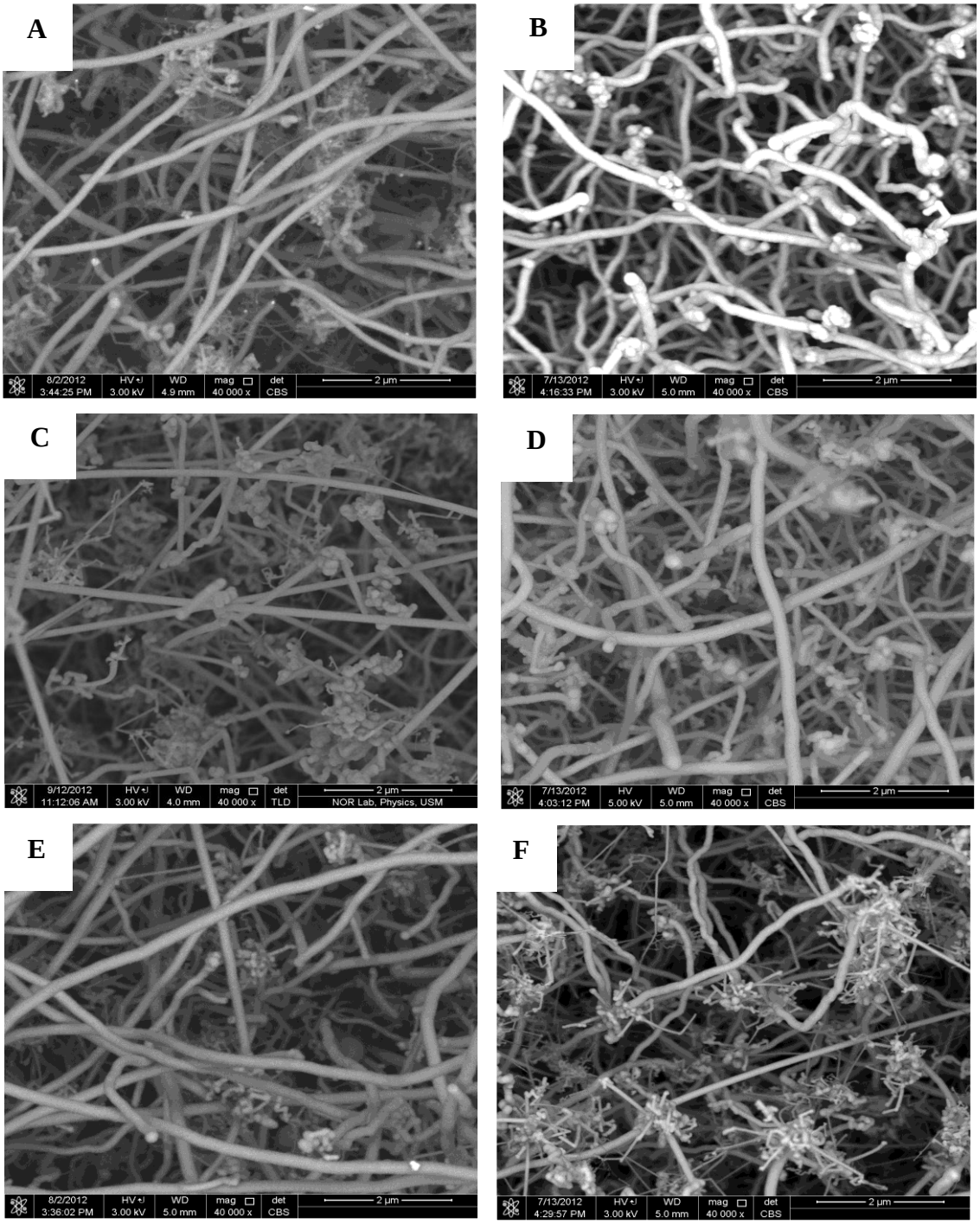

Figure 6.1: FESEM images of SiNWs grown using Au catalyst layer thicknesses of (A) 10nm, (B) 20nm, (C) 40nm, (D) 60nm, (E) 80nm and (F) 100nm.

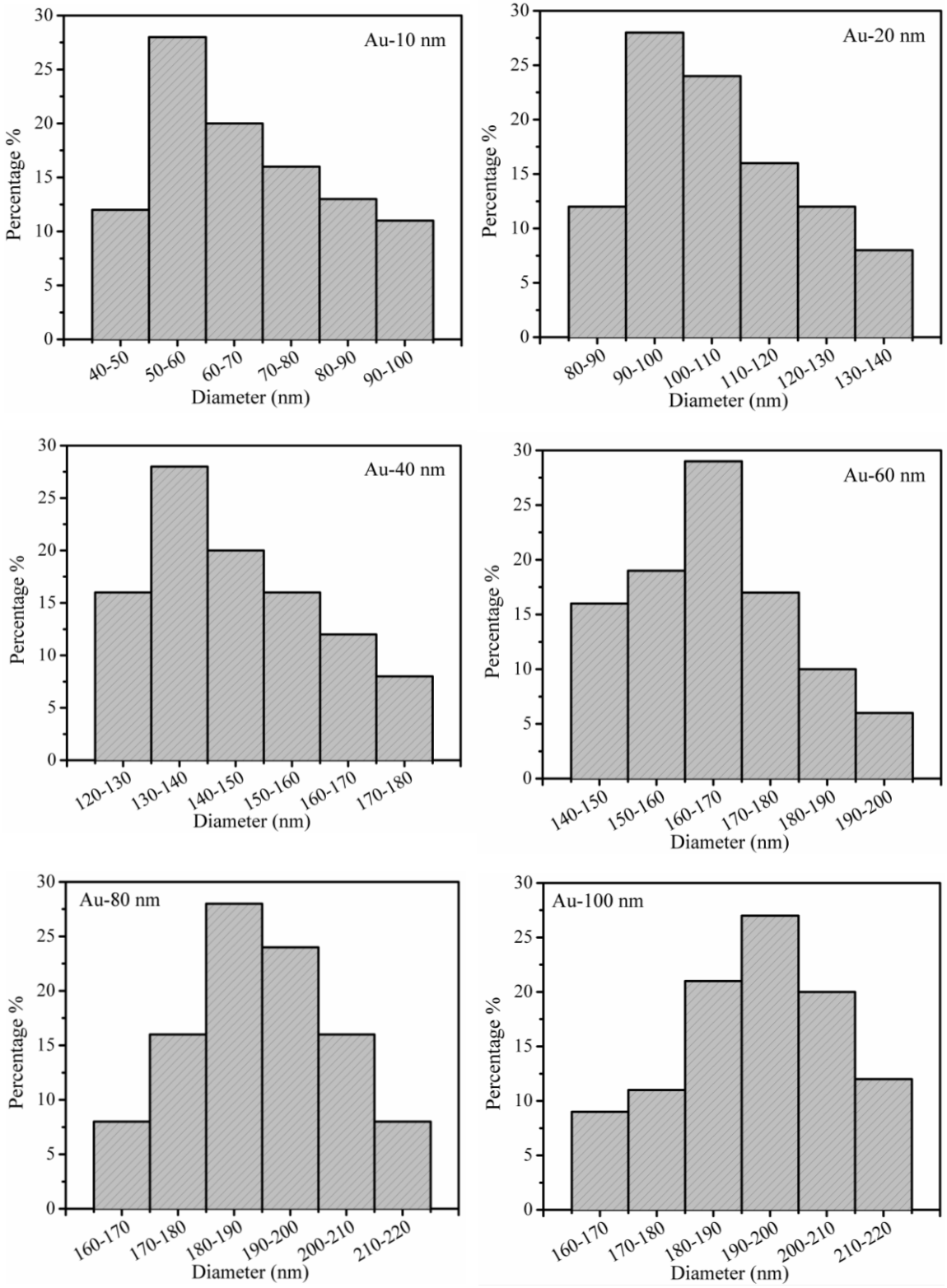

Figure 6.2: Diameter distribution of SiNWs grown using Au catalyst layer thicknesses of (A) 10nm, (B) 20nm, (C) 40nm, (D) 60nm, (E) 80nm and (F) 100nm.

Figure 6.3 shows the relationship between the Au film thickness and the modal diameter of the SiNWs. The wire diameter clearly increased when the thickness of the catalyst thin film increased. Moreover, the density of the SiNWs decreased as the Au thin film thickness increased. Thus, the wire density of SiNWs decreased from 18NW/μm^2 to approximately 6NW/μm^2 as the Au film thicknesses increased from 10 to 100nm (Figure 6.3).

From FESEM images, the Au catalyst diameters that were used to grown SiNWs are calculated and listed in Table 6.1. The liquid/solid interface tension (σ_{LS}) for the Au/Si of the prepared SiNWs was calculated from the Eq. 4.2. The SiNWs prepared using 10nm thick Au films have the largest σ_{LS} of 0.69 while 100nm Au thickness produces wires with the lowest σ_{LS} value of 0.097. In addition, the contact angle β between the Au catalyst and the NW surface was calculated from Eq. 4.4 and listed in Table 6.1.

The SiNWs catalyzed by a 10nm Au film thickness have a minimum β value of 39.2° and the NWs prepared with 100nm Au thick show the maximum value was 84°. Cross-sectional FESEM images of SiNWs synthesized using 20, 60 and 100nm thick Au catalysts are shown in Figure 6.4. The SiNWs were randomly oriented relative to the substrate, and the mean wire length decreased from 12μm to approximately 10μm as the thickness of the catalyst film increased from 20nm to 100nm. In addition, the images demonstrated that the grown SiNWs were tapered, and Au nanoparticles remained at the tip of the wires, indicating that the SiNWs were grown by the VLS mechanism.

Figure 6.5 presents the TEM images of SiNWs synthesized using 20, 60, 80 and 100nm thick Au catalysts. The TEM images confirmed the increase in wire diameter with an increase in the thickness of the catalyst thin film. Moreover, a tapered SiNW with a Au catalyst particle at the tip of the wire is shown.

From the images a core-shell structure was clearly indentified and this confirms the PL spectra results when Sn, Al and Au catalysts were used to grow SiNWs. A worm-like structure was also observed in SiNWs catalyzed by 80nm and 100nm thick Au films, which confirm the FESEM image (Figure 6.1E and 6.1F). The eutectic temperature of the catalyst-Si system can determine the required temperature to synthesize a SiNW via the VLS mechanism.

Most metal catalysts exhibit high eutectic temperatures with Si, whereas the Au-Si system has a relatively low eutectic point of approximately 363°C at 19% Si concentration. Figure 6.6 shows the phase diagram for Au-Si. The Si atoms from SiH_4 species are absorbed by the Au droplet and form an alloy Au/Si at a temperature higher than the eutectic point which led to a reduction in the melting temperature compared with the melting point of Au at 1064.5°C (Schmidt *et al.* 2009).

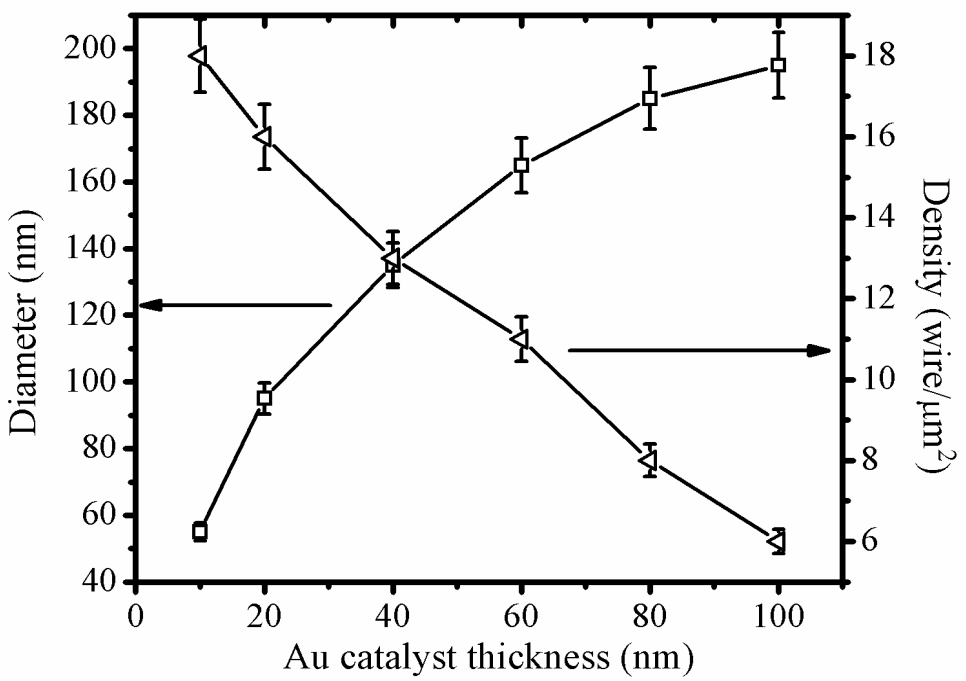

Figure 6.3: The Au catalyst thin film thickness vs. wire diameter and density.

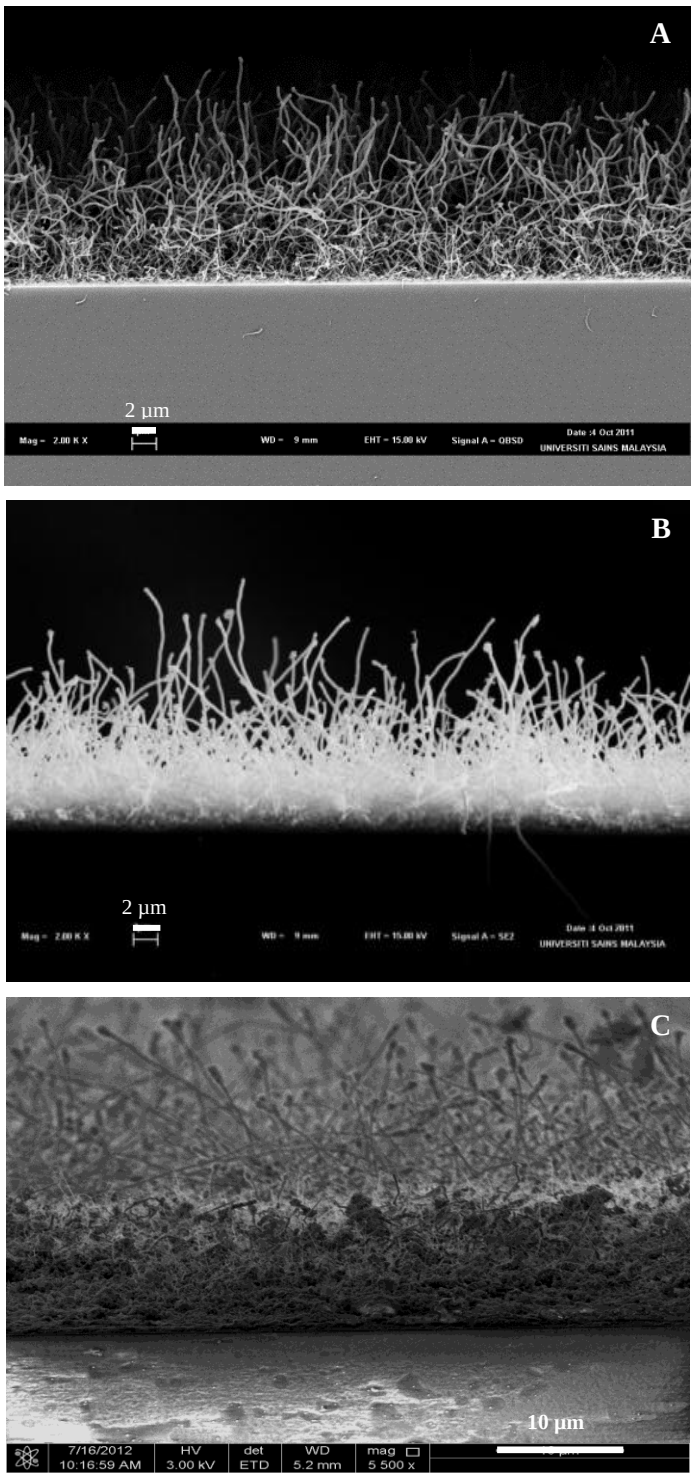

Figure 6.4: Cross-sectional images for SiNWs synthesized using Au catalyst layer thicknesses of (A) 20nm, (B) 60nm and (C) 100nm.

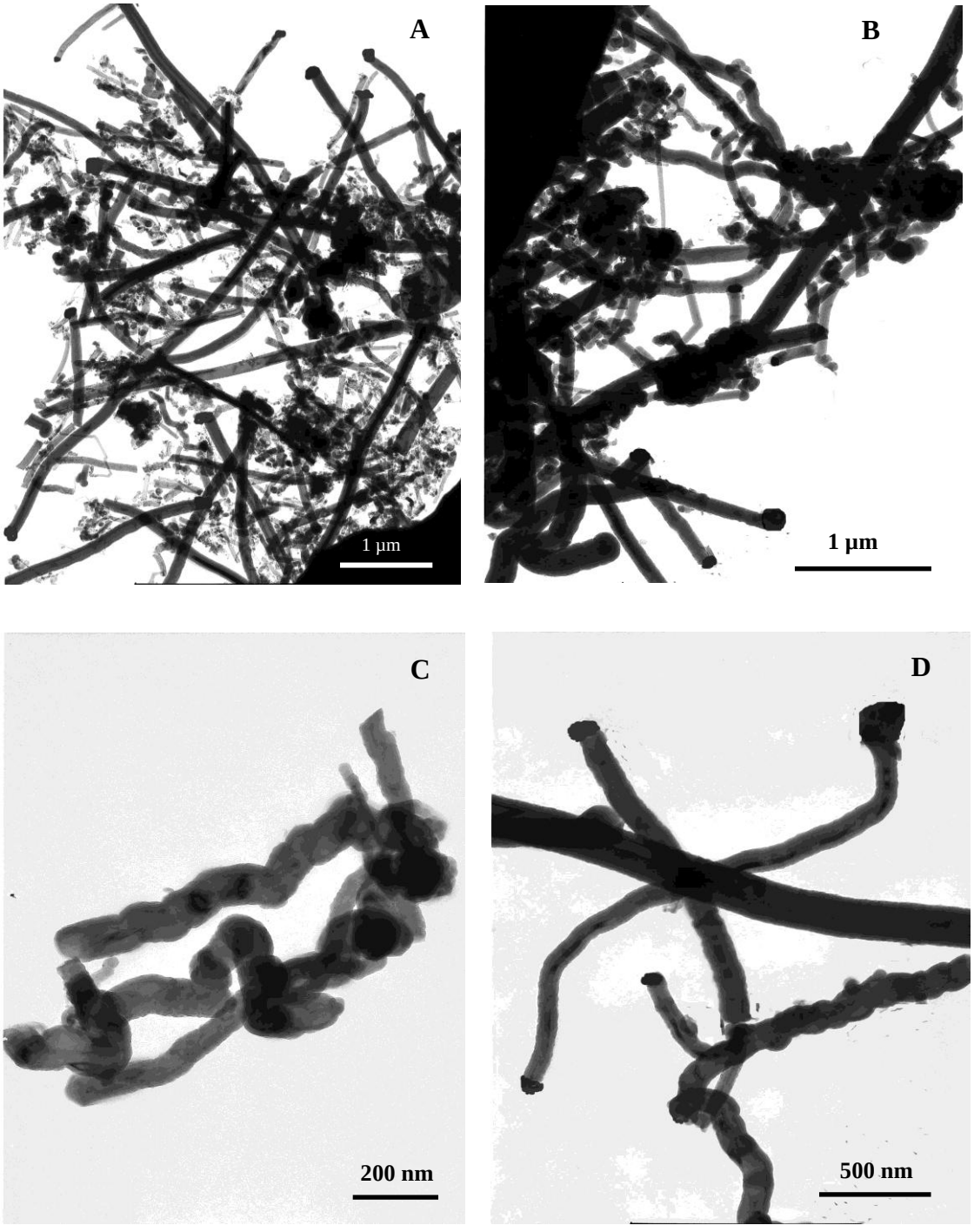

Figure 6.5: TEM images of SiNWs prepared by Au catalyst layer thicknesses of (A)20nm, (B) 60nm, (C) 80nm and (D) 100nm.

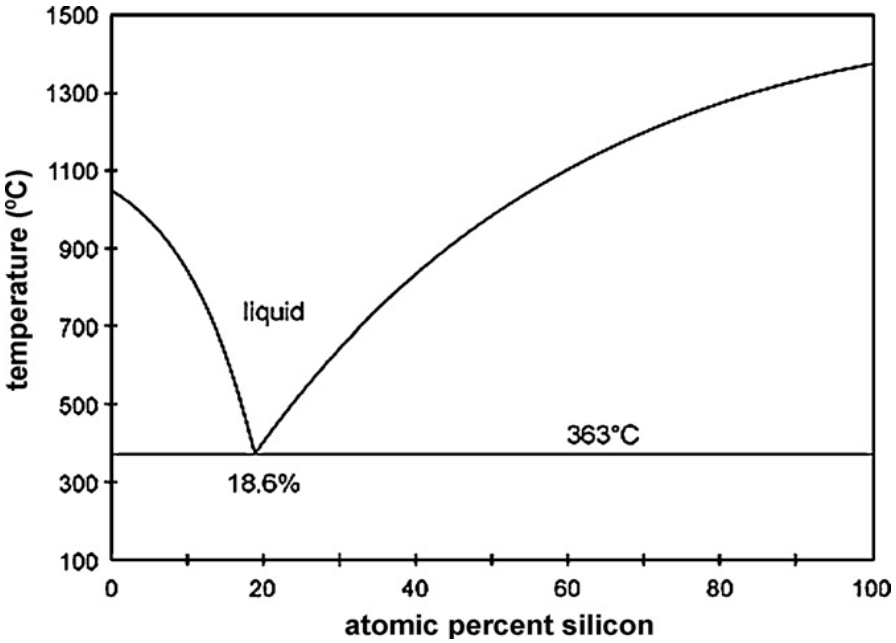

Figure 6.6: The Au- Si alloy binary phase diagram (Schmidt et al. 2009).

Table 6.1: The crystal size, diameter, contact angle and surface tension of the SiNWs grown by Au catalyst.

Au catalyst thickness (nm)	Au catalyst average diameter D_c (nm)	SiNWs diameter D_w (nm)	D_c/D_w	Metal/Wire contact angle ß^O	Surface tension σ_{LS} (J/m^2)
10	87	55	1.58	39.2	0.69
20	125	95	1.31	49.5	0.58
40	152	135	1.12	63.0	0.42
60	177	165	1.07	68.7	0.32
80	187	185	1.01	81.5	0.13
100	196	195	~ 1.0	84.0	0.09

Figure 6.7 presents the Energy Dispersive X-ray (EDX) analysis carried out on the stem of the SiNWs catalyzed by a 40nm thick Au film. The NWs consist of Si and Au with an atomic ratio 82.31% and 2.26 % respectively. In addition, the Au nanoparticles are located on the top of the grown SiNWs which confirms the TEM images and indicate that the Au catalyst helps in the synthesis of SiNWs via the VLS mechanism.

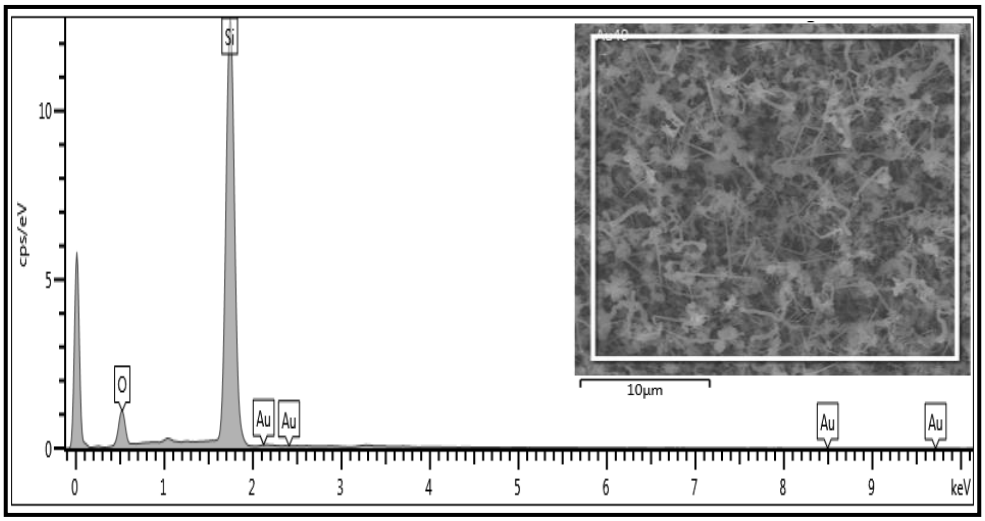

Figure 6.7: EDX spectra of SiNWs catalyzed using 40nm film of Au measured over a wide area of the sample.

6.2.2 Crystalline Structure

The XRD patterns of the SiNWs grown using various thicknesses of Au catalysts are shown in Figure 6.8. The diffraction peaks of the prepared SiNWs correspond to the (111), (220) and (311) lattice planes of the cubic phase of Si.

The diffraction peaks became sharper as the wire diameter increased because of the increasing catalyst thickness, indicating that the crystallinity of the grown SiNWs was enhanced or the particles size was increased. The increase in the XRD peak intensities could be due to the increase in the particle size according to the Scherrer formula (Cullity B.D 1972). The lattice constant (a) of the cubic structure is given by the relationship (Cullity B.D 1972):

$$\frac{1}{d_{hkl}^2} = \frac{h^2 + k^2 + l^2}{a^2}, \qquad (6.1)$$

Where d_{hkl} is the interplanar spacing of the atomic planes, and h, k and l are the Miller indices. The lattice constant values are listed in Table 6.1. Moreover, the diffraction peaks of Au related to the (111) and (200) lattice planes were also detected as shown in Figure 6.8, confirming the deposition of Au particles on the top of the SiNWs. Hamidinezhad *et al.* (2011) and Pham *et al*. (2011) obtained crystalline SiNWs using Au as the catalyst and synthesized by PECVD and thermal evaporation methods, respectively. The diffraction peaks of the Au catalysts appeared in the XRD patterns because the metal particles were located on top of the SiNWs.

Comparing with the SiNWs prepared using Sn and Al catalysts with the same deposition conditions (Al-Taay et al. 2013a; Al-Taay et al. 2013b) (as Chapters 4 and 5), the Au catalyst produced the highest crystallinity SiNWs and that makes it the most suitable for solar cell applications.

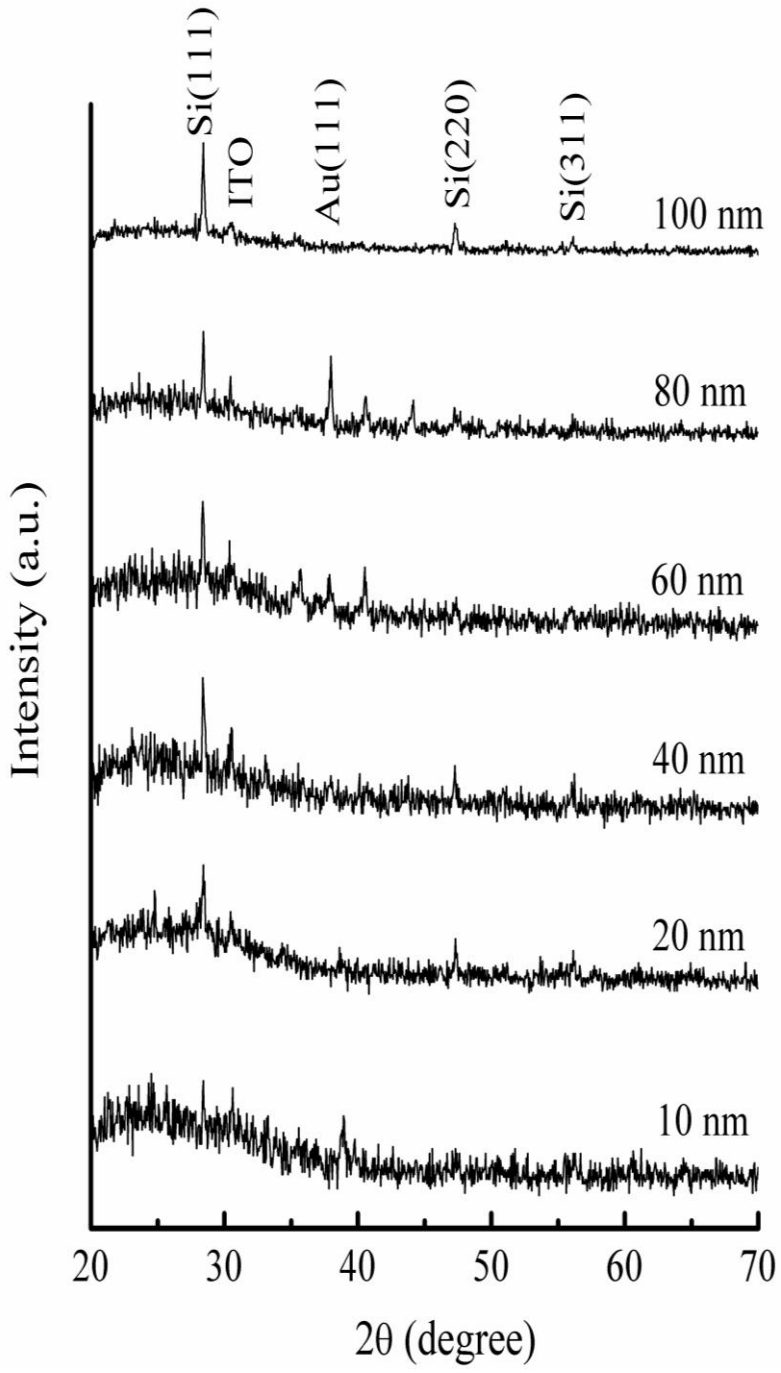

Figure 6.8: XRD patterns of SiNWs prepared using Au catalyst layers with thicknesses 10-100nm.

6.2.3 Optical Properties

6.2.3.1 Photoluminescence Spectra (PL)

The photoluminescence (PL) spectra of nanocrystalline materials is one of the most effective tools for diagnosing the structure quality, surface states, and impurity levels inside the optical band gap (Mahdi et al. 2012). Figure 6.9 shows the PL spectra of the SiNWs catalyzed using various Au thicknesses. A red emission band can be observed in the PL spectra for all the grown SiNWs. The SiNWs catalyzed by 10nm thick Au exhibited a broad emission band that peaked at 720nm. The PL spectrum of the SiNWs prepared using 20nm Au catalyst showed two emission bands centered at 788 and 909nm, whereas the grown wires using 40nm thick Au produced bands at 752 and 890nm. The emission bands for SiNWs catalyzed by Au layers are listed in Table 6.2.

According to the theoretical prediction of Sanders and Chang (1992), quantum confinement can be expected for nanostructure dimensions less than the free excitonic Bohr radius (5nm) of c-Si. The diameter of the grown SiNWs is relatively larger than the Bohr radius. Thus, the quantum confinement effect is not evident. The red band was emitted because of the interface between the amorphous sheath layer and the crystalline core of the wire (Shi *et al.* 2009). In the PL spectrum measured at room temperature for SiNWs synthesized by the oxide-assisted method, a main green emission band at 2.05eV (604nm) and a smaller red emission band at 1.7eV (729nm) were observed (Colli *et al.* 2006).

Bhattacharya *et al.* (2004) obtained red PL emissions centered at 826 and 886nm for different SiNW diameters, synthesized by pulsed laser vaporization using Au as catalyst. In addition, Pham *et al.* (2011) recorded PL spectra at room temperature for SiNWs prepared by thermal evaporation using Au as the catalyst.

They obtained a broad emission band at 650nm, and two other bands that peaked at 455 and 510nm were observed when measured at low temperatures.

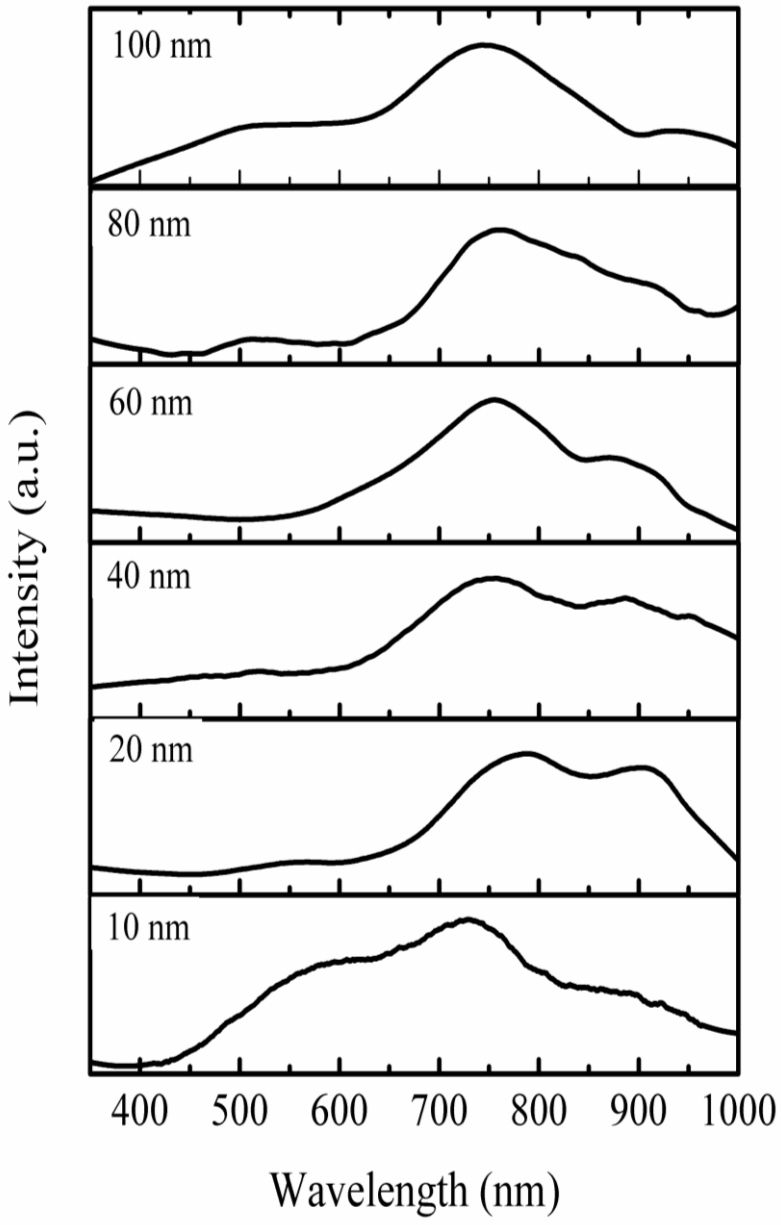

Figure 6.9: Room temperature PL spectra of the SiNWs grown using Au catalyst layer thicknesses of (A) 10nm, (B) 20nm, (C) 40nm, (D) 60nm, (E) 80nm and (F) 100nm.

6.2.3.2 Raman spectra

Raman spectra of SiNWs grown using various thicknesses of Au catalyst are presented in Figure 6.10. The SiNWs grown using 10, 20, 40, 60 and 80nm layers of Au produced Raman peaks located at 497, 503, 503, 505 and 507cm^{-1}, respectively. The Raman peak was identified as the first order transverse optical phonon mode (1TO). The 1TO peak location depends on the degree of crystallinity of the Si. For c-Si the 1TO peak appears at 520cm^{-1} and for a-Si at 480cm^{-1} (Liu *et al.* 2001; Li *et al.* 2013). The Raman peak of the SiNWs catalyzed by 100nm thick Au appeared at 513.5cm^{-1} which is shifted by approximately 6.5cm^{-1} compared with the c-Si 1TO peak location.

The wire diameter increased because of the increase in catalyst thickness, which led to an increase in the crystallinity of SiNWs that could have caused the shifting of the 1TO peak toward higher frequencies. The two broadening bands that peaked at 290 and 920cm^{-1} are ascribed to the second order transverse acoustic phonon mode (2TA) and the second order optical phonon mode (2TO), respectively, and were observed for all prepared SiNWs (Li *et al.* 1999).Wang *et al.* (2000) found that the Raman peak location is dependent on the diameter of the wires synthesized by laser ablation, and the Raman peak appeared at 509.8cm^{-1} for 10nm diameter NW and shifted to 517.7cm^{-1} when the diameter of the wires increased to 21nm.

Meshram *et al.* (2011) obtained a Raman peak at 515cm^{-1} for NWs with diameters ranging from 50nm to 300nm for SiNWs grown at 400°C by hot wire CVD. Moreover, a sharp Raman peak at 500cm^{-1} for SiNWs synthesized by PECVD at 400°C with diameters ranging from 40nm to 400nm was also observed (Chong *et al.* 2011).

The crystallite size D_r values of SiNWs catalyzed with various Au thickness are calculated from Eq. 4.5. The crystallite size increased from 1.9nm for the wires grown using a 10nm thickness of Au catalyst to 3.22nm for the wires catalyzed by a 100nm

thick Au catalyst (Table 6.2). The increased crystallite size when the Au catalyst thickness increased implies enhanced crystallinity of the SiNWs grown with an increased catalyst thickness, as illustrated also in XRD patterns. Ma et al. (2008) studied the annealing effect on the Raman peak location and the shape of the nc-Si and nc-Si/SiO_x core/shells. They found that annealing samples led to a shift in the 1TO Raman peak from 495 cm^{-1} to 517 cm^{-1} and the peak became narrower in width due to the increase in the particles size.

Chong *et al.* (2012) prepared SiNWs using 50nm to 250nm In droplet size with a home-built hot-wire-assisted PEVCD system. They concluded that the SiNWs grown using 40W rf power had high crystallinity with a crystallite size of 4.2nm compared with those prepared using 80W rf power with crystallite size of 2.9nm. Moreover, they noted that the TO band of the SiNWs grown using low rf power was located at 517cm^{-1}, whereas the band peaked at 512cm^{-1} for the wires synthesized using high rf power.

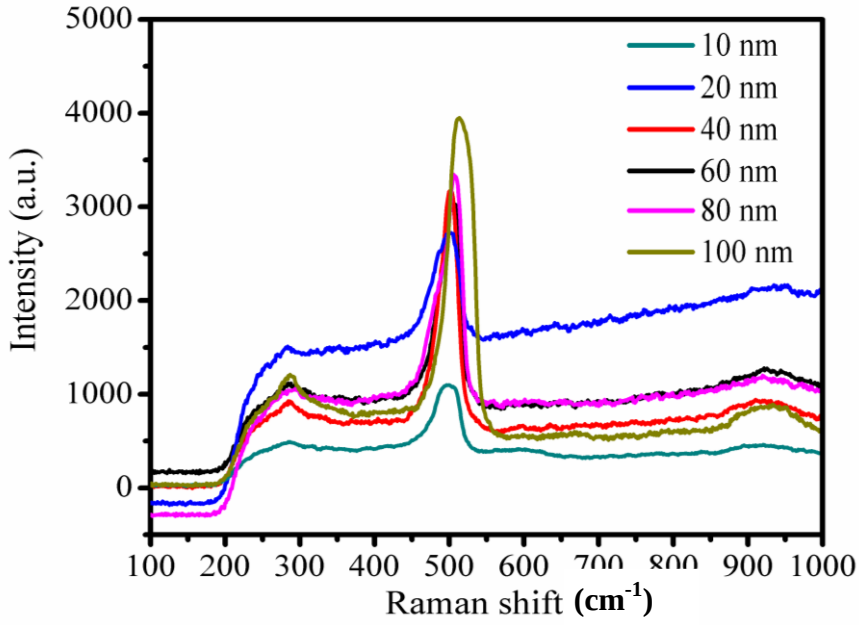

Figure 6.10: Raman spectra of SiNWs prepared using an Au catalyst layers with thicknesses of 10nm, 20nm, 40nm, 60nm, 80nm and 100nm.

Table 6.2: Peak locations of the Raman and PL bands for SiNWs grown with an Au thin film catalyst of different thicknesses.

Catalyst thickness (nm)	Lattice constant (Å)	FWHM of (111) XRD peak(degree)	PL bands (nm)	Raman band (cm^{-1})	D_r (nm)
10	5.430	0.221	720	496.5	1.90
20	3.438	0.210	788, 909	503	2.21
40	5.435	0.198	752, 890	503	2.21
60	5.438	0.197	761, 881	505	2.35
80	5.445	0.190	762	507	2.51
100	5.438	0.182	750	513.5	3.22

6.3 Conclusions

Varying thicknesses of the Au catalyst ranging from 10nm to 100nm have been used to synthesize SiNWs via the PPECVD method at 400°C. FESEM and TEM images confirmed that the wire diameter increased as the thickness of the catalyst film increased, and the wire length decreased from 12µm to approximately 10µm. The presence of Au nanoparticles at the tips of the wires indicates that the SiNWs were grown via the VLS mechanism. Moreover, the diameter of the grown SiNWs increased from 55nm to 195nm when the Au catalyst thickness increased from 10nm to 100nm, respectively. XRD patterns showed that the synthesized SiNWs consisted primarily of crystalline Si with (111), (220) and (311) growth planes. The SiNWs grown by Au catalyst had high crystallinity which makes them suitable for fabricating a solar cell. The PL spectra of the SiNWs prepared with various Au thicknesses showed red emission bands. Raman spectroscopy confirmed the increase in crystallinity of the

SiNWs as the Raman peaks shifted from 497cm^{-1} to 513.5cm^{-1} as the catalyst thickness increased. The crystal sizes that were calculated from the Raman spectra showed that the SiNWs catalyzed by 100nm thickness of Au metal had the largest particle size of 3.22nm while using 10nm thickness of Au catalyst produced SiNWs with a smaller particle size of 1.9nm.

CHAPTER 7
PREPARATION AND PROPERTIES OF Zn-CATALYZED SiNWs

7.1 Introduction

In this work, Zn metal was used for the first time to catalyze SiNWs via PPECVD. The thin films of Zn catalyst with controlled the thicknesses in the range of 10-100nm were deposited successfully on the ITO coated glass substrate by the thermal evaporation method. This Chapter examines the effect of the thickness of the thin film catalyst on the morphology, structure and optical properties of the grown SiNWs. FESEM and TEM were used to describe the morphology of prepared SiNWs. Through X-ray diffraction, the structures of the prepared SiNWs were determined while the optical properties were studied through the photoluminescence (PL) and Raman spectra of the grown wires.

7.2 Synthesis of SiNWs Catalyzed by Zn

7.2.1 Surface Morphology

The surface morphologies of SiNWs, synthesized via PPECVD and catalyzed using various thicknesses of Zn are depicted in the FESEM images shown in Figure 7.1. The as-grown SiNWs appear to be distributed randomly on the ITO substrate with a curved shape. The 10 and 20nm thick Zn catalysts produced thin and short curved SiNWs as shown in Figures 7.1A and 7.1B respectively. When the thickness of the Zn catalyst was increased, the wire shapes gradually changed and the wires grew randomly, overlapping each other and increasing in diameter as shown in Figures 7.1C to 7.1E.

The as-grown SiNWs became thicker and their diameters reached 240nm. Moreover, the wires appeared to be more curved when a 100nm thick Zn catalyst was used (Figure 7.1F). Thus, catalyst thickness appears to affect the diameter, shape, and density of the as-grown SiNWs. Figure 7.2 shows the analysis of the diameter distributions of the synthesized SiNWs using different Zn thicknesses that were calculated with an error ratio of about ±5%. The diameter of SiNWs prepared with 10nm thick Zn catalyst varied from 60nm to 110nm, whereas using a 20nm thick Zn catalyst led to SiNWs with diameters that ranged from 60nm to 120nm, as shown in Figures 7.2A and 7.2B, respectively.

The diameters of the SiNWs prepared using 40 and 60nm thick Zn catalysts were in the range of 120nm to 130nm and 130nm to 140nm respectively. A similar trend was found for SiNWs grown with 80 and 100nm thick Zn catalysts. The SiNWs had larger diameters of 165 and 175nm respectively (see Figures 7.2E and 7.2F).

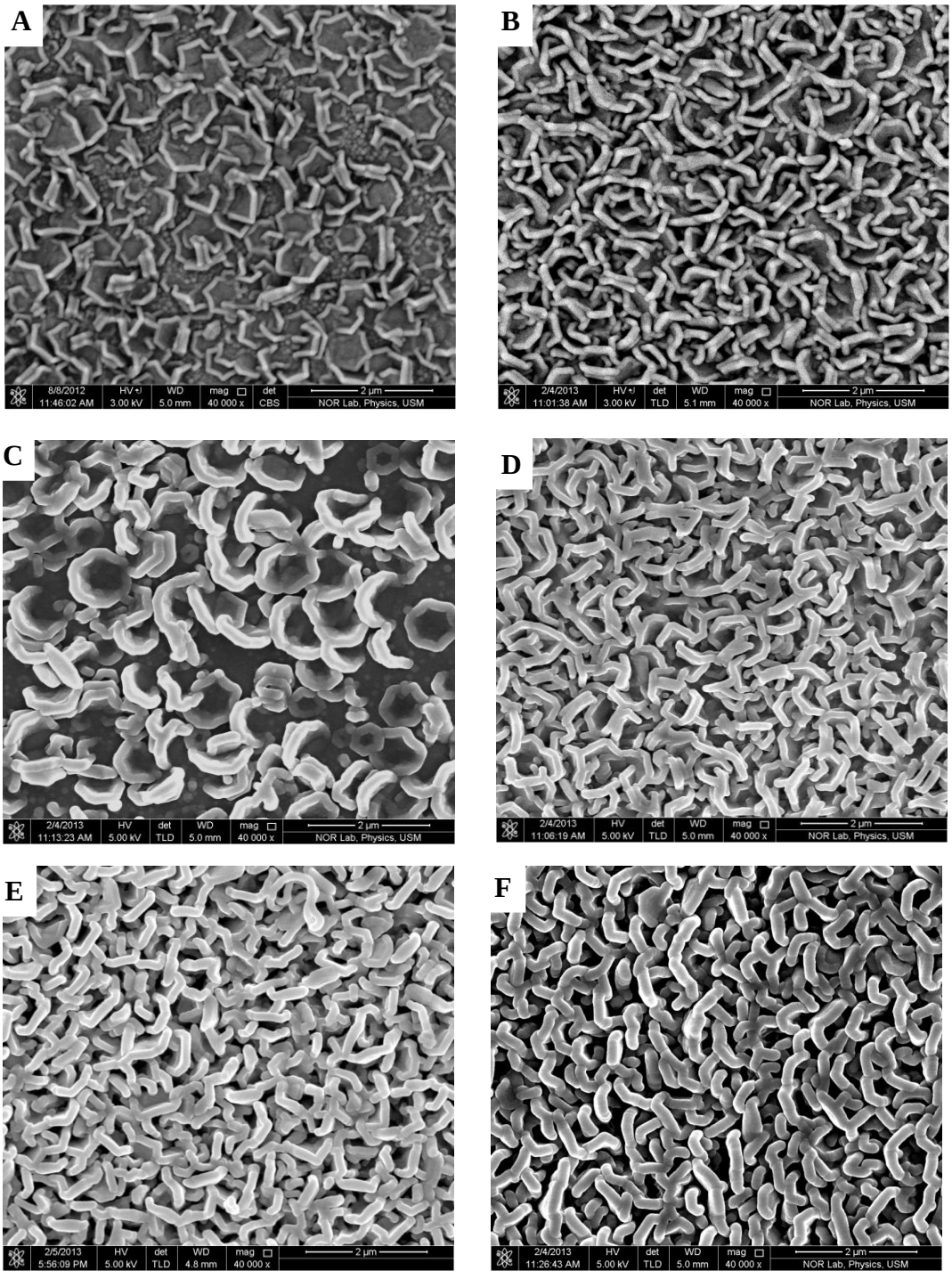

Figure 7.1: FESEM images for SiNWs prepared using Zn catalyst thicknesses of (A) 10nm, (B) 20nm, (C) 40nm, (D) 60nm, (E) 80nm and (F) 100nm.

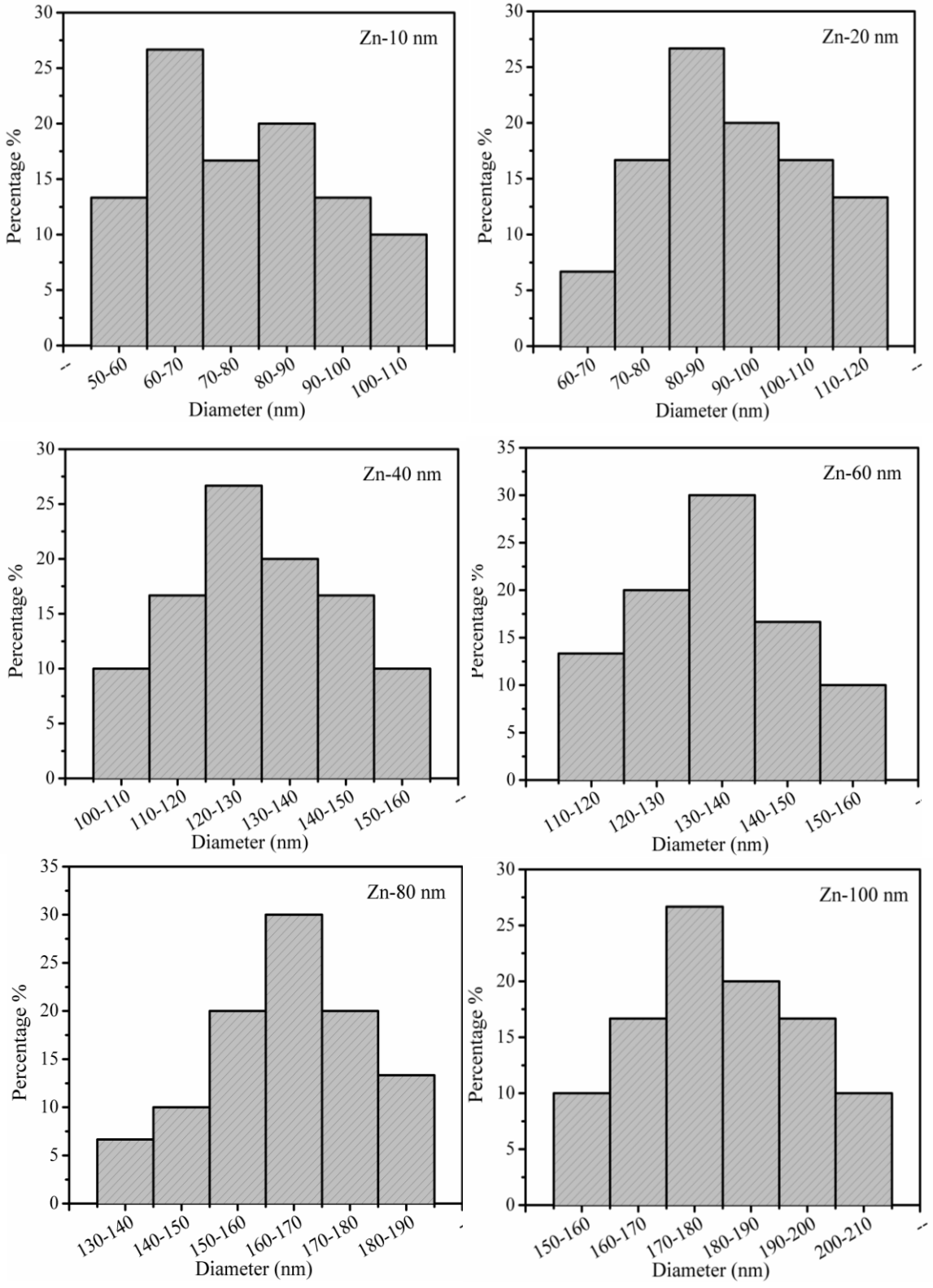

Figure 7.2: Diameter distributions of the SiNWs grown using a Zn catalyst with various thin film thicknesses from 10-100nm.

Using plasma to prepare SiNWs via the PECVD method usually leads to an increase in the rate of deposition compared with the CVD technique that in turn leads to an increase in the diameter and length of the prepared wires. Yu *et al.* (2000) and Chung *et al.* (2000) synthesized SiNWs with diameters between 15 and 35nm using CVD at temperatures of 440°C to 500°C using Zn as the catalyst. The Zn catalyst was created through the deposition of $ZnCl_2$/ethanol solution on a Si substrate and heating the substrate at 450°C. They found that SiNW synthesis via the gas-phase reaction of $SiCl_4$ with Zn at 1000°C resulted in SiNWs with diameters in the range of 40nm to 80nm and this is less than the 120-130nm diameter obtained using PECVD with 40nm thickness on Zn metal catalyst. Zn metal was likewise observed at the end of the NWs, indicating that SiNWs could be grown via the VLS mechanism (Uesawa et al. 2010).

The results are in accordance with the results obtained by Al-Taay et al. (2013a) and Al-Taay et al. (2013b) (as Chapters 4 and 5), who found that using Sn and Al catalysts with varying thicknesses in the range of 10nm to 100nm led to an increase in the diameter of as- grown SiNWs by PPECVD. Other studies similarly found that catalyst thickness plays an important role in determining the NW diameter and that an increase in catalyst thickness leads to an increase in SiNW diameter (Cui *et al.* 2001; Wang *et al.* 2006; Qin *et al.* 2011) .

The densities of the SiNWs grown using Zn catalysts with varying thicknesses were measured from the FESEM images. Figure 7.3 presents the relationships among catalyst thickness, average diameter, and density of SiNWs. An increase in Zn thin-film thickness from 10nm to 100nm led to an increase in the average diameter of grown SiNWs from 65nm to 205nm. The densities of synthesized SiNWs likewise decreased from 15NW/μm^2 to 7NW/μm^2 when the Zn thin-film thickness increased from 10nm to 100nm, as shown in Figure 7.3.

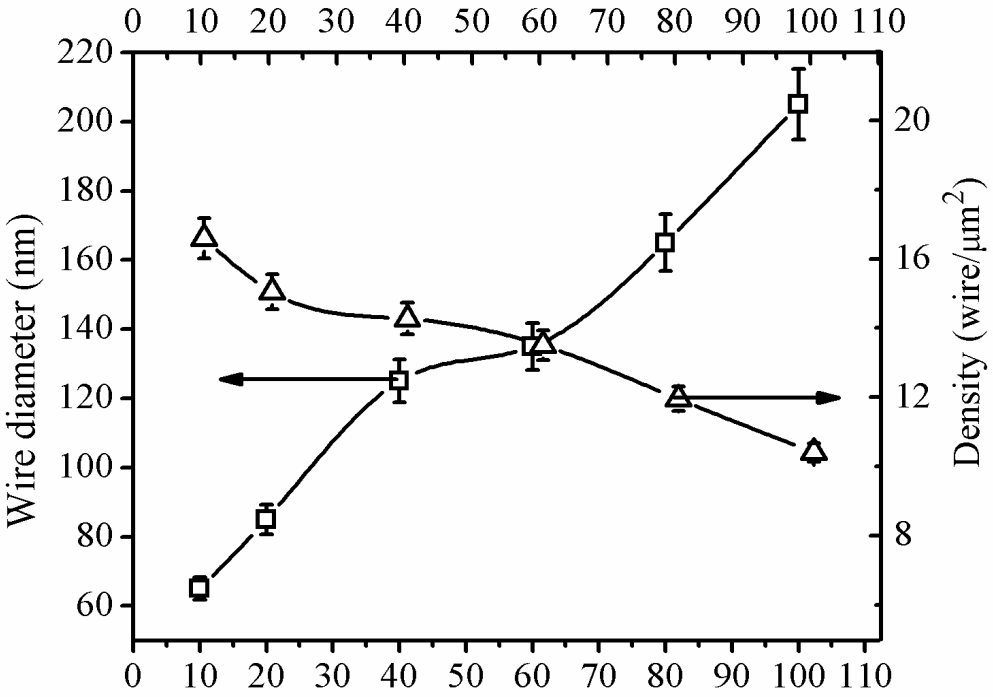

Figure 7.3: The Zn catalyst thin film thickness vs. wire diameter and density.

Figure 7.4 shows the cross-sectional images of SiNWs catalyzed using Zn with 20 and 60nm thicknesses. The height of the grown wires using 20 and 60nm of Zn catalyst was 420 and 350nm, respectively. Al-Taay *et al.* (2013c) (as Chapter 6) noted that increasing the Au catalyst thickness from 20 to 100nm lead to a decrease in the wires height from 12 to 10μm.

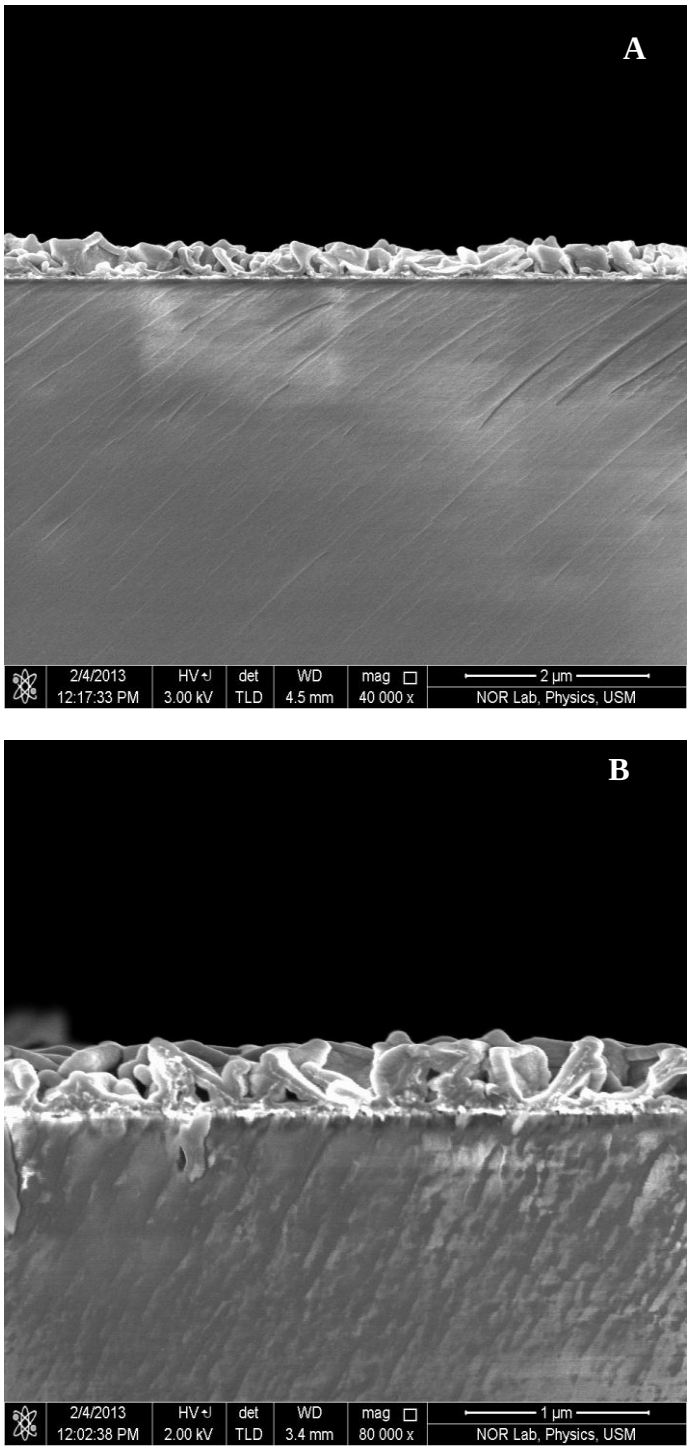

Figure 7.4: Cross-sectional images of SiNWs synthesized using Zn catalyst thicknesses of (A) 20nm and (B) 60nm.

Energy Dispersive X-ray (EDX) measurement was conducted for SiNWs catalyzed with 40nm thick Zn during the FESEM observations (Figure7.5). The EDX spectra were collected from a large part of the SiNWs. Analysis showed the presence of Si with an atomic ratio of 54% and of Zn metal with an atomic ratio of 8.6%, indicating that the Zn catalyst is involved in the growth of SiNWs. The small amount of oxygen shown was due to the exposure of the samples to the atmosphere during preparation.

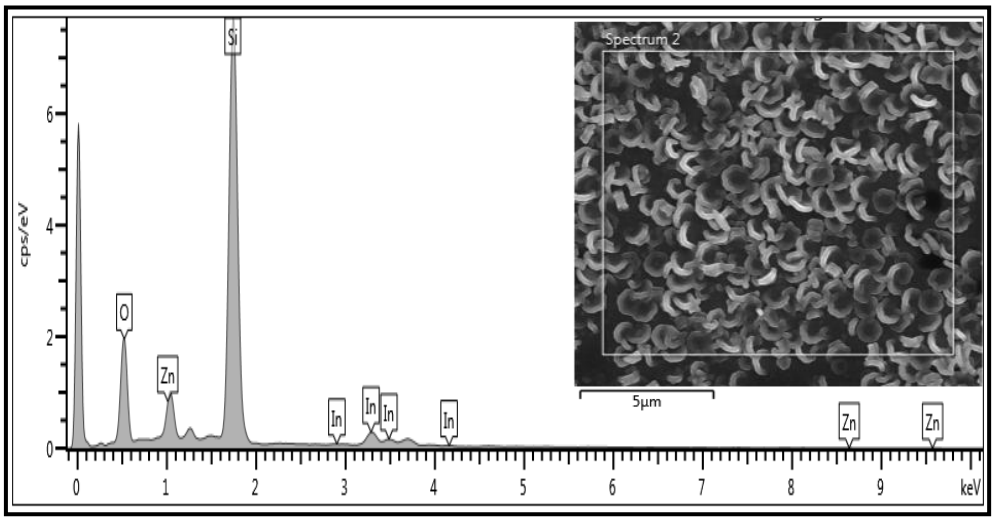

Figure 7.5: EDX spectra of SiNWs catalyzed using a 40nm thin film of Zn.

Further microstructure characterization was carried out using the TEM. The TEM images of SiNWs catalyzed with 20, 60, 80 and 100nm thick Zn catalysts are shown in Figure 7.6. The Zn catalyst particle was clearly observed at the tip of the NWs, indicating that Zn catalyzed the growth of SiNWs via the VLS mechanism. The TEM images confirmed that an increase in catalyst thickness results in an increase in wire diameter. The phase diagram of Zn–Si is shown in Figure 7.7. It is dominated by a single eutectic point at 420°C at a Si concentration of 10% , despite its high vapor pressure of 0.2 mbar at 420°C (Schmidt et al. 2009). Moreover, Zn metal has an advantage in that Zn contamination can be removed easily compared with Au metal contamination.

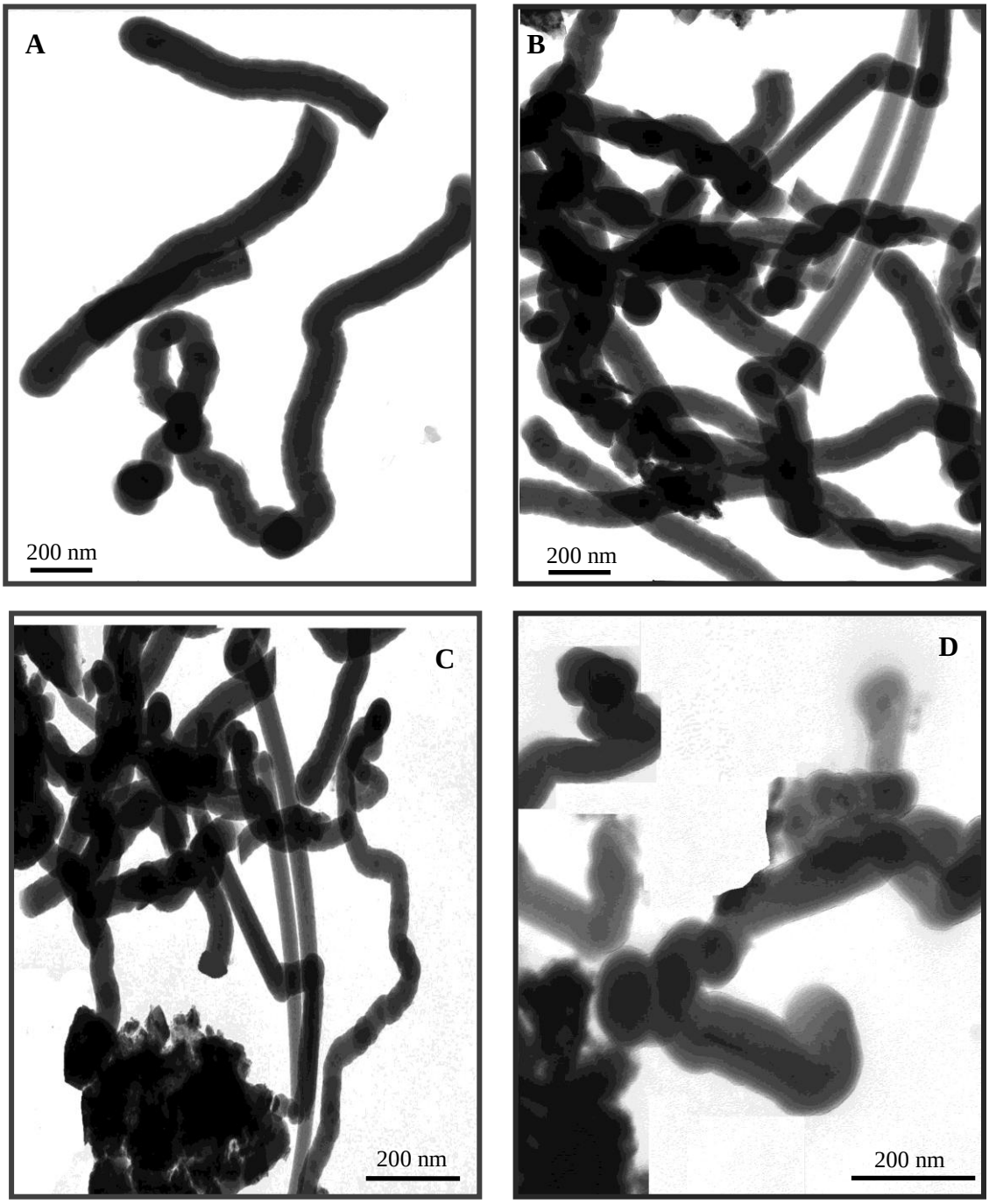

Figure 7.6: TEM images of SiNWs prepared by Zn catalyst thin films with thicknesses of (A) 20nm, (B) 60nm, (C) 80nm and (D) 100nm.

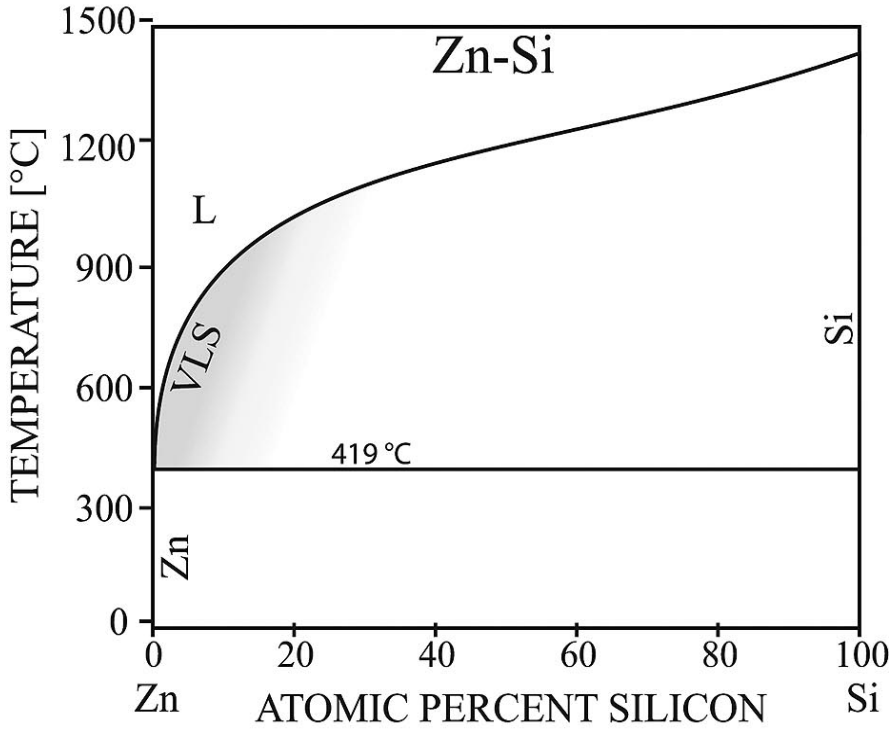

Figure 7.7: The Zn- Si alloy binary phase diagram (Schmidt et al. 2010).

7.2.2 Crystalline Structure

The XRD patterns of SiNWs synthesized with varying Zn thicknesses in the range of 10nm to 100nm are shown in Figure 7.8. The XRD patterns for all the prepared samples show a diffraction at peak about 30.6°, which corresponds to the (200) plane of the ITO-coated glass substrate.

Figure 7.8 further shows that diffraction peaks appeared at 28.4°, 47.3° and 56.1° corresponding to the (111), (220) and (311) planes of the crystalline Si phase, respectively. These peaks were most pronounced for SiNWs catalyzed with 10 and 80nm thick Zn films, indicating that the prepared SiNWs had good crystallinity. Zn metal diffraction peaks from the (111) plane were also detected at 36°, indicating the catalyzed growth of SiNWs via the VLS mechanism.

The absence or low intensity appearance of XRD peaks could be due to the low temperature used in the SiNW preparation, which in turn led to the growth of wires with low crystallinity. Using PECVD to prepare an amorphous layer over the wire, led to a reduction in the crystallinity of the as-grown SiNWs (Iacopi *et al*. 2007; Yu *et al.* 2009; Yu *et al.* 2008).

Another reason for the weak crystallinity is that the wires were grown with a polycrystalline structure and the strength of the diffraction peaks in the XRD pattern is dependent on the particle size and the larger particles dominate (Mahdi *et al.* 2012).

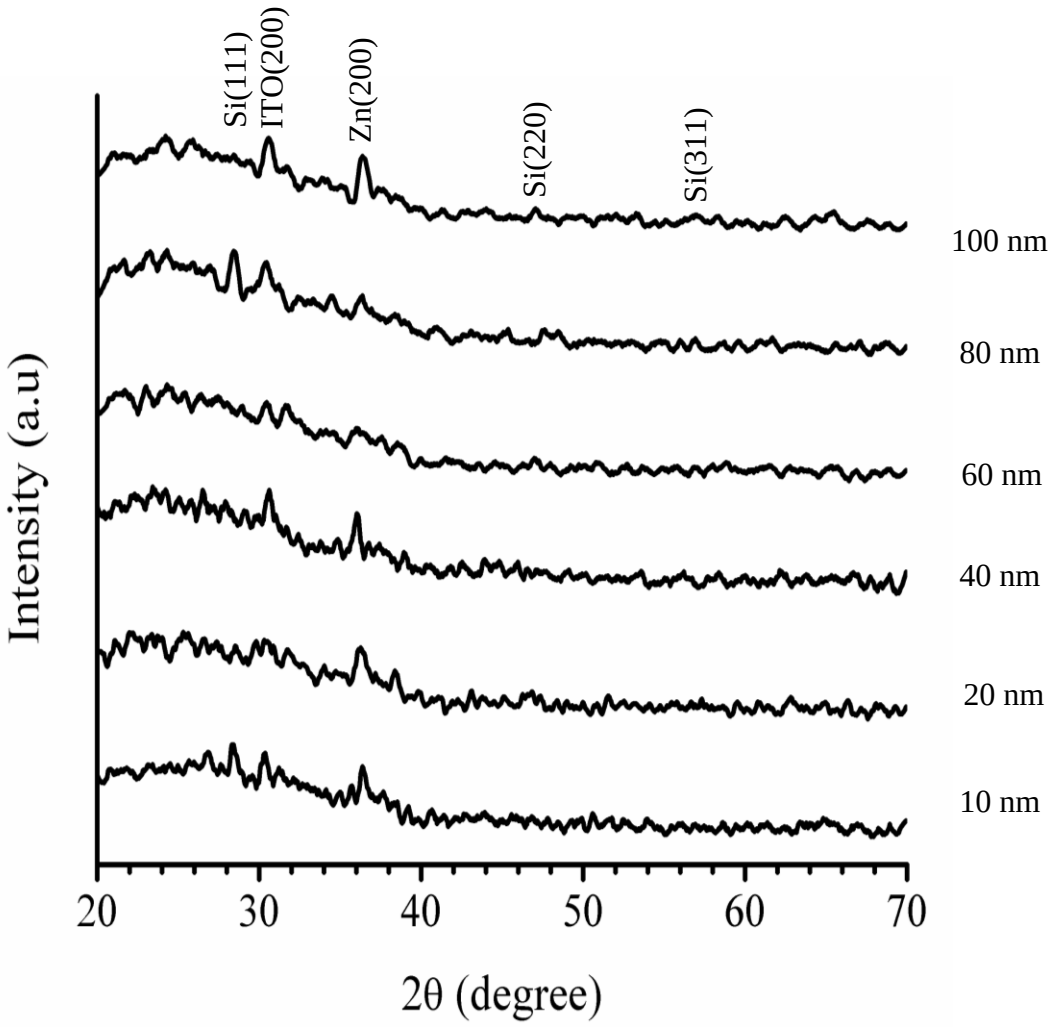

Figure 7.8: XRD patterns of SiNWs prepared using various Zn catalyst thicknesses in the range of 10-100nm.

7.2.3 Optical Properties

7.2.3.1 Photoluminescence Spectra (PL)

Figure 7.9 shows the room-temperature PL spectra of the SiNWs catalyzed using Zn metal with varying thicknesses in the range of 10nm to 100nm. Green, blue and red emission bands were observed from the SiNWs. The PL spectrum of the SiNWs catalyzed with 10nm thick Zn displayed a broad emission band with peaks at 500, 750, 850 and 920nm, whereas the 20nm thick Zn catalyst produced SiNWs with three broad emission bands located at 540, 750 and 900nm. Two broad emission bands at 450 and 750nm were observed in the PL spectrum of the SiNWs grown with 100 nm thick Zn.

The PL emission for SiNWs catalyzed with 40, 60 and 80nm thick Zn are listed in Table 7.1 and shown in Figure 7.9. In nanocrystalline materials, two emission peaks can usually be observed, a sharp one from the band-to-band recombination and a broad emission peak at a longer wavelength, due to a surface state or defect (Tai and Guo 2008). However, the emission peak could be related to the electron–hole recombination that occurred near the band edge. Based on the theoretical prediction of Sanders and Chang (1992), the quantum confinement effect appears when the nanostructure dimension becomes comparable to or less than that of the free excitons of c–Si.

The prepared SiNWs presented a huge NW diameter of about 50nm, indicating quantum confinement. Moreover, when the NW diameter becomes smaller, the energy band gap between the occupied and non-occupied states of electrons is enlarged, thereby leading to a blue shift (Ke *et al*. 2002). Furthermore, for oxide-passivated SiNWs, a specific red PL at 745 nm was observed, and this peak may originate from the Si–O–Si bridge bonds along the crystalline direction (111) based on the theoretical calculation and this peak is not observed from other structures such as (110) or (112) SiNWs, implying its dependence on the crystalline configurations (Kang *et al.* 2011).

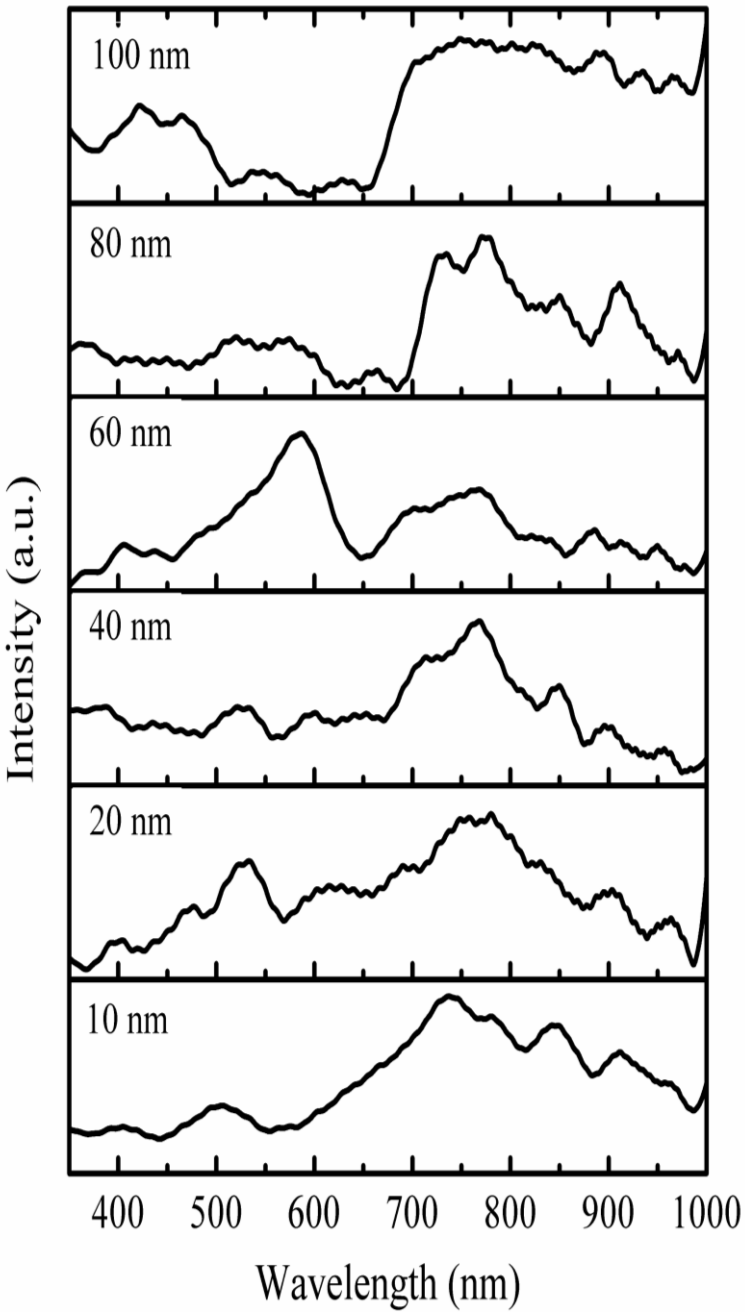

Figure 7.9: PL spectra of SiNWs prepared using Zn catalyst layers with thicknesses of 10-100nm.

7.2.3.2 Raman spectra

Raman spectra of SiNWs catalyzed via different Zn metal thicknesses ranging from 10nm to 100nm are shown in Figure 7.10. The spectra for all prepared samples have two broad peaks located at 920 and 290cm^{-1} which correspond to the second order optical phonon mode and the second order transverse acoustic phonon mode of crystalline Si, respectively (Li *et al.* 1999).

In contrast, with the Raman spectrum of c-Si, which is attributed to the first optical phonon peak at 520 cm^{-1} (Pan *et al.* 2005). The first order Raman peak of the SiNWs catalyzed with 10 and 80nm thick Zn exhibited a sharp peak located at 496cm^{-1} with a down shift of about 24cm^{-1}. On the other hand, SiNWs prepared using 20, 40, 60nm thick Zn displayed broad Raman peaks at 482, 476 and 475cm^{-1}, respectively. The Zn with 100nm thickness also produced SiNWs with a broad Raman peak located at 468 cm^{-1}.

The SiNWs catalyzed with 10 and 80nm of Zn displayed a sharp Raman peak and it was the closest to c-Si location at 520 cm^{-1}, whereas broad peaks were observed for other samples catalyzed using different Zn thicknesses. Raman spectroscopy is an effective tool for estimating the amount of crystalline and amorphous phase in nanomaterials. Thus, the crystalline material presented a sharp Raman peak, located at 520cm^{-1}, whereas the amorphous material displayed a broader peak at lower frequency (Li *et al.* 2013). The location and curve shape of Raman band depends on the crystallinity, size uniformity, oxidation layer and on the variation of crystal constants (Niu et al. 2006). Our results are a good match with the results reported in the literature (Kiany *et al.* 2011; Meshram *et al.* 2011).

The relationship between nanoparticle size and Raman shift assumes that the phonon confinement effect occurs when the particle diameter exceeds the phonon mean free path, resulting in the 1TO Raman band shifting towards a lower wave number. The increasing the wires diameter led to shift of the 1TO band toward lower wave numbers because the wires became less crystalline as the diameter increased. The SiNWs prepared using 80nm Zn catalyst displayed a Raman peak located at 495cm^{-1} because this sample showed good crystallinity compared with the other catalysts as shown in XRD pattern. Table7.1 presents the crystallite size values of SiNWs catalyzed with

different Zn catalyst layer thicknesses. The SiNWs catalyzed with 10 and 80nm thick Zn had a larger crystal size of approximately 1.9nm diameter.

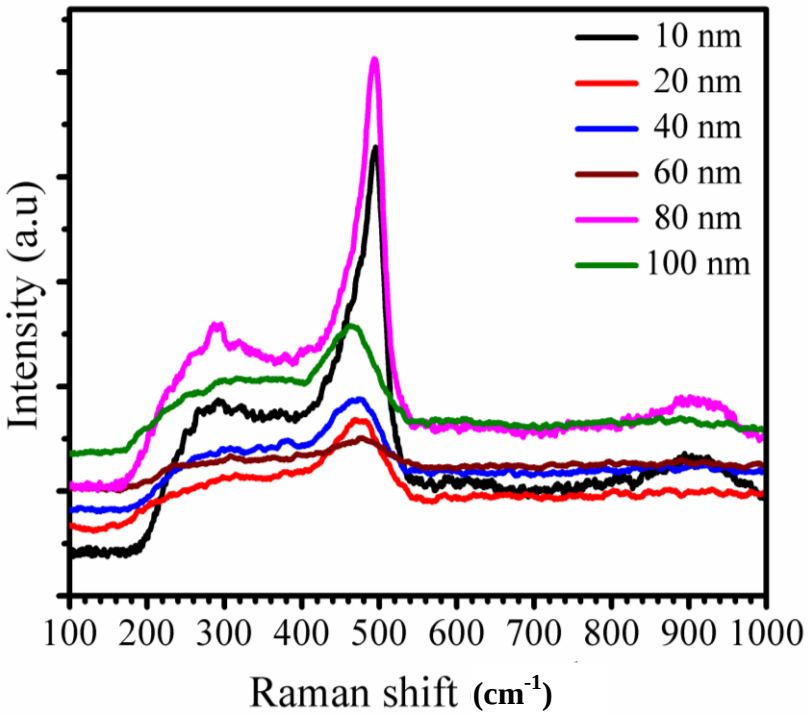

Figure 7.10: Raman spectra of SiNWs prepared using Zn catalyst layers with thicknesses of 10-100nm.

Table 7.1: Raman and PL peak locations and crystal size of the grown SiNWs using Zn catalyst.

Zn thickness (nm)	Raman peak (cm^{-1})	crystallite size D_r (nm)	PL bands (nm)
10	496	1.9	500, 750, 850, 920
20	482	1.55	540, 760, 900
40	476	1.41	540, 750, 850, 900
60	475	1.4	590, 750, 900
80	495	1.9	550, 750, 900
100	468	1.3	450, 750

7.3 Conclusions

Zn metal with various thicknesses was successfully used as a catalyst to grow high-density SiNWs through PPECVD on ITO-coated glass substrates. The FESEM images show that Zn catalyst thickness can affect and control the morphology and diameter of as- grown SiNWs. The diameters of the NWs increased from 65 to about 205nm as a result of increased catalyst thickness from 10nm to 100nm. X-ray diffraction patterns reveal that SiNWs prepared using 10 and 80nm-thick Zn have good crystallite sizes compared with the SiNWs prepared using other thicknesses.

Green, blue, and red emission bands are observed in the PL spectra of the SiNWs catalyzed with various Zn thicknesses. Raman spectra show that the first-order band is sharp and is located nearest to the c–Si location for SiNWs catalyzed using 10 and 80nm-thick Zn. In comparison, a broad Raman band is observed for other prepared samples, indicating that SiNWs grown using 10 and 80nm-thick Zn catalysts have higher crystallinity. These results are confirmed by the XRD. The crystallite sizes calculated from the Raman spectra showed that the SiNWs catalyzed by 10nm and 80nm thickness of Zn metal had the largest model particle sizes of 1.9nm while using 100 nm thickness of Zn catalyst produced SiNWs with a smaller modal particle size of 1.3nm.

CHAPTER 8

COMPARISON AND DISCUSSION OF THE PROPERTIES OF METAL-CATALYZED SiNWs

8.1 Introduction

The Pulsed PECVD method has been used to grow SiNWs on indium tin oxide-coated glass substrates. Sn, Au, Al and Zn metals at various of thicknesses in the range 10nm to 100nm were used to catalyze SiNW growth. This Chapter compares the results obtained on the performance of SiNWs grown using different types and thicknesses of catalysts. The effect of the catalyst type and thickness on the SiNW properties, such as morphology, and structural and optical properties is summarized here.

8.2 Effect of Catalyst Type and Thickness on the Morphological Properties of SiNWs.

SiNWs were grown using (PPECVD) with Sn, Au, Al and Zn catalysts. Various SiNWs morphologies were observed in this study. SiNWs grown using a 10nm thin film Sn catalyst showed inhomogeneity in diameter. When the Sn catalyst thickness was increased to 20nm, the NWs showed a more homogenous diameter. Also, the SiNWs grown using 60, 80 and 100nm films showed significant improvements in wire morphology, especially in terms of homogeneity in diameter.

Meanwhile, homogeneous and long NWs were observed when the Au catalyst in the thickness range of 10nm to 60nm was used, but kinking or worm-like structures appeared when the thickness was increased to 80nm and 100nm as shown n TEM images (Fig.6.5).

An Al catalyst produced shorter NWs that tended to aggregate when the Al thickness was increased to 60nm. Also, two morphological structures were obtained when the catalyst thickness was 80nm and 100nm: thick, short, aligned NWs, and small, circular NWs, respectively. Using a thin-layer Zn catalyst produced thin and short-curved NWs, but with increasing Zn thickness, the NWs grew in an overlapping manner and appeared more curved (at 100nm Zn thickness). The Au catalyst produced the longest NWs. With an Au catalyst thickness of 20nm, the mean NW length was 12µm. This NW length was reduced to 10µm with increasing catalyst thickness (100nm). The Zn catalyst produced NWs with the shortest length.

An increase in the thickness of the catalysts led to an increase in catalyst diameter as shown in the FESEM images, which in turn resulted in an increase in the diameter of the prepared SiNWs. The average diameter of the grown SiNWs increased with increasing thickness of the Sn, Al, Au and Zn catalysts (Figure. 8.1). The 10nm thick Al catalyst resulted in the largest diameter of SiNWs of 115nm, whereas the same thickness of Au catalyst resulted in the smallest SiNW diameter of 55nm. However, the SiNWs catalyzed by Al metal were thicker compared with the others grown using Sn, Au and Zn metals (see Figure. 8.1). The average diameter of the SiNWs grown using various catalysts with different thicknesses, in the range 10nm to 100nm are listed in Table 8.1.

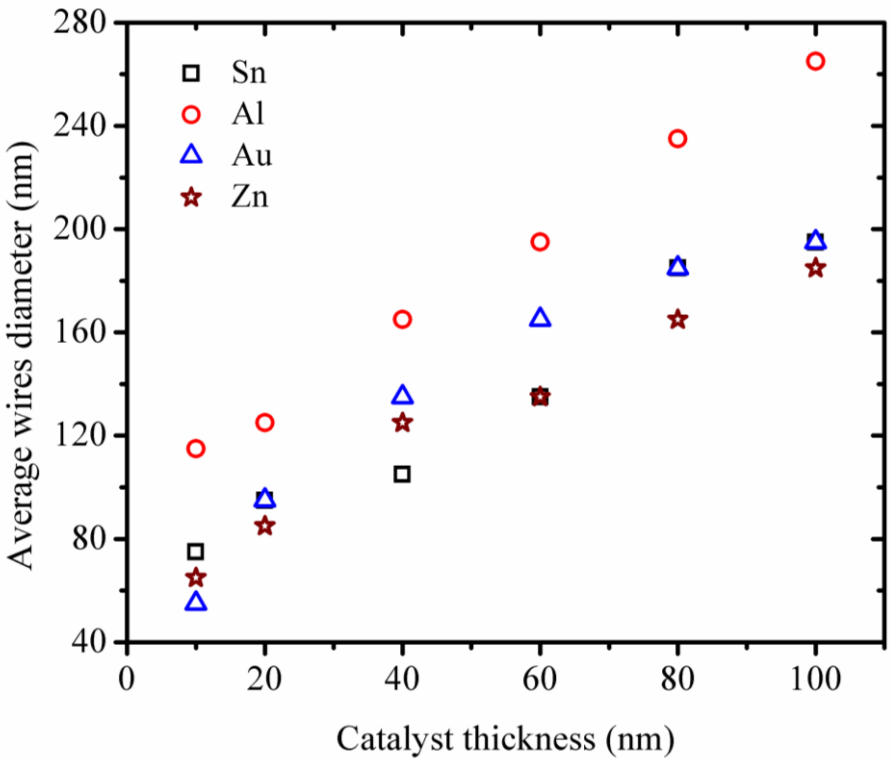

Figure 8.1: Average diameter of NWs vs. thickness of Sn, Au, Al and Zn catalysts.

The density of SiNWs grown using various catalyst thicknesses, in the range 10nm to 100nm, has been plotted in Figure. 8.2. Generally, the density of the SiNWs decreased as the catalyst thickness increased. Figure 8.2 shows that a 10nm thick Al catalyst produced the greatest SiNW density of 20 NW/μm^2, whereas 100nm thick Au resulted in the lowest density of 6 NW/μm^2.

Table 8.1: The average diameter of the SiNWs grown using various catalysts with different thicknesses.

Catalyst thickness (nm)	Diameter (nm)			
	Sn	Al	Au	Zn
10	75	115	55	65
20	95	125	65	85
40	105	165	135	125
60	135	195	165	135
80	185	235	185	165
100	195	265	195	175

The growth of SiNWs is influenced by the physical properties of the catalyst type used. The eutectic point of the catalysts/Si determines the minimum required temperature for the growth of the SiNWs. The underlying mechanism of Si growth with Al catalysis is VSS, whereas with the other catalysts, the underlying mechanism was VLS. The melting points, eutectic points and the growth mechanisms of the various catalysts are listed in the Table 8.2. Using different types of metals to catalyze SiNWs is very important. Thus, there are more than one reason to use Sn, Au, Al and Zn metals in the preparation of SiNWs. According to the various eutectic points of the Sn, Au, Al and Zn metals with Si, the growth temperature will control the wires morphology and in turn the other physical properties.

Three of the metals used had a eutectic point less than the chosen growth temperature. That means the growth process will happen through VLS. Another reason for choosing a different catalyst was that each has a different diffusion ability in Si will which lead to effects on the properties of the grown SiNWs, especially the optical and electrical properties. Furthermore, all of the used catalysts require relatively low growth temperatures that avoid melting the ITO-glass substrates. The use of this type of cheap substrates is desirable. On the other hand, increasing the growth temperature up to the eutectic point of Al-Si will lead to melting of the substrate. The substrate type affects the growth of the nanowires, thus using another type of substrate such as Si or sapphire may lead to SiNWs with different morphology and properties. Moreover, using other substrates than ITO-glass may create a problem for the back contact of the fabricated device.

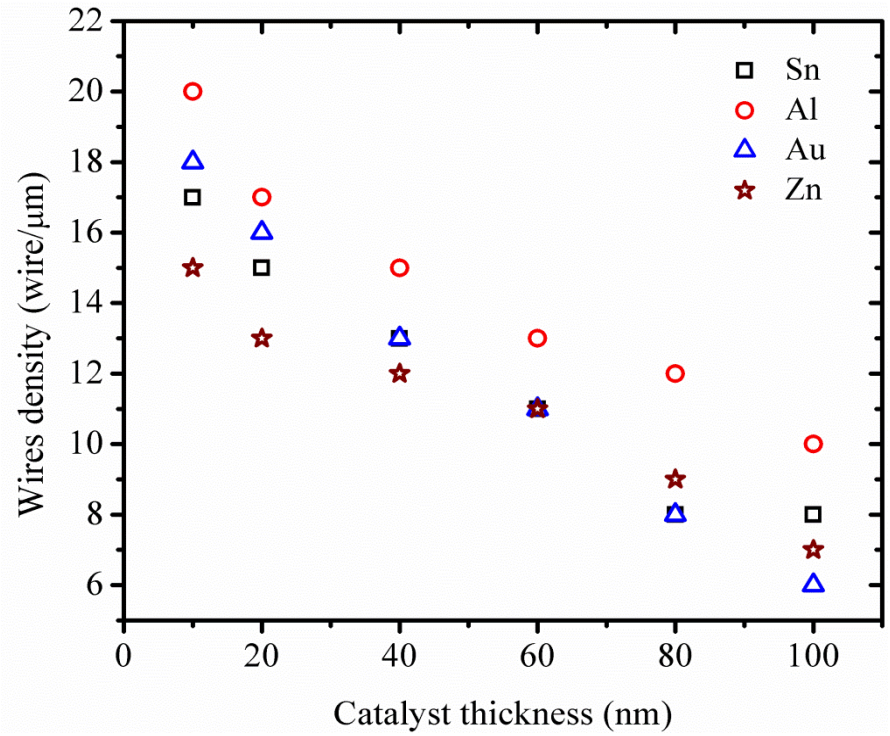

Figure 8.2: The NW density vs. thickness of Sn, Al, Au and Zn catalysts.

The X-ray diffraction measurements show that the SiNWs grown by Au catalysts had higher crystallinity compared with other catalysts. Moreover, the diffraction peaks became sharper with increasing wire diameter because of increasing catalyst thickness, indicating that the crystallinity of the grown SiNWs was enhanced.

Table 8.2: The melting point and Si/metal eutectic point of Sn, Au, Al and Zn metals.

Catalyst	Melting Point (^{o}C)	Si eutectic point (^{o}C)	Growth Mechanism
Sn	231.9	232	VLS
Au	1064.18	363	VLS
Al	660.3	577	VSS
Zn	419.58	420	VLS

8.2.2 Comparison of the Optical Properties of SiNWs

The PL and Raman spectra were employed to study and investigate the optical properties of the SiNWs catalyzed by Sn, Au, Al and Zn metals. Generally, a red emission band was observed clearly in the PL spectra for all prepared SiNWs. The PL spectra of the SiNWs prepared using a Sn catalyst showed red emission in all samples, except those catalyzed by 60nm Sn films emitted light at a wavelength of 608nm.

In addition, SiNWs catalyzed with Al at various thicknesses displayed green, blue and red emission bands which corresponded to recombination at the oxygen defect in the Si oxide layer, which coated the outer surface of the NWs. The PL spectra of the SiNWs prepared with various Au thicknesses showed a red emission band. Green, blue, and red emission bands in the PL spectra were observed for the SiNWs catalyzed by Zn with various thicknesses. In the Raman spectrum, the first order transverse optical mode

(1TO) appeared in all SiNWs catalyzed using Sn, Au, Al and Zn. However, the 1TO peak location depended on the catalyst type and thickness. The Raman peak location for SiNWs prepare using Sn, Al,Au and Zn are listed in Table 8.3. Important results were observed at a catalyst thickness of 80nm for all catalysts, and the 1TO Raman peak was closest to the crystalline Si peak location in all prepared samples, except for the SiNWs prepared using 100nm of Au metal where the Raman peak was closest to the crystalline Si peak.

The crystal size of the grown SiNWs calculated from the Raman spectra confirmed decreasing SiNWs size as the thickness of Sn, Al and Zn catalysts increase from 10nm to 60nm and 100nm. The SiNWs prepared using 80nm thick Sn, Al and Zn catalysts had the largest crystal size. The SiNWs synthesized with the Au catalyst diverged from this behavior, in that the crystal size increased as the catalyst thickness increased from 10nm to 100nm, as shown in Figure. 8.3.

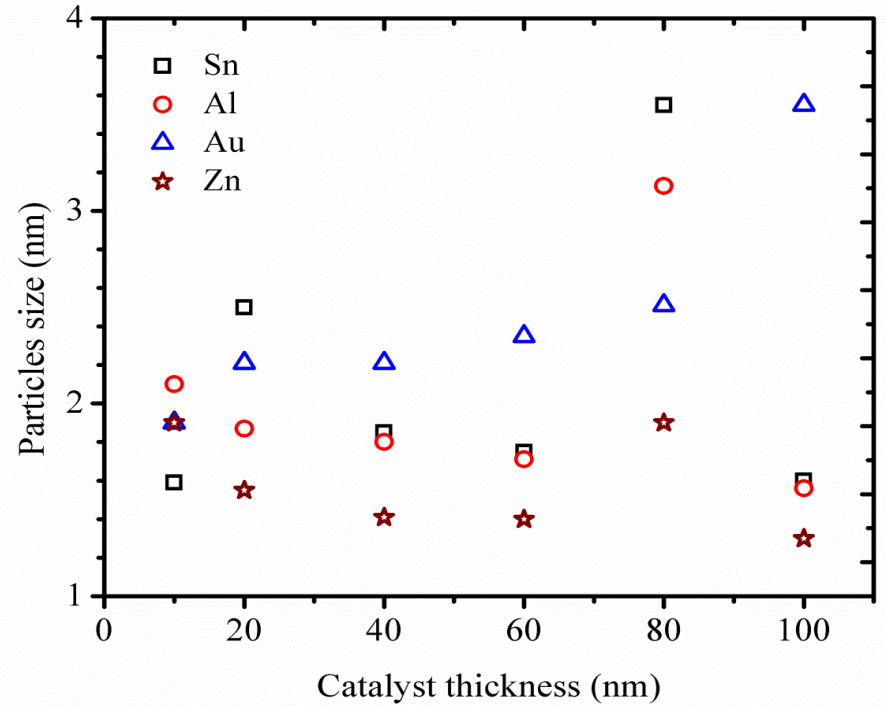

Figure 8.3: The crystal size vs. thickness of Sn, Al, Au and Zn catalysts.

Table 8.3: The Raman peak location of the SiNWs grown using various catalysts with different thicknesses.

Catalyst thickness (nm)	Raman peak position (cm^{-1})			
	Sn	Al	Au	Zn
10	497	500	496.5	496
20	505	495	503	482
40	494	493	503	476
60	491	490	505	475
80	513	511	507	495
100	488	484	513.5	468

8.3 Conclusions

SiNWs can be prepared by Sn, Au, Al and Zn metals as catalysts. The growth mechanism of the wires is VLS when Sn, Au and Zn catalyst are chosen and VSS mechanism for wires catalyzed by Al metal. The wire morphology (diameter, length, and shape) is significantly affected by the type and thickness of the catalyst film. In general, the wires became thicker and shorter with increasing catalyst thickness from 10nm to 100nm for all catalyst types.

The SiNWs prepared using an Au catalyst had higher crystallinity than those prepared using the other catalysts. Moreover, the optical properties of the grown SiNWs are affected by the catalyst type and thickness. For example, the Raman 1TO peak location depends on catalyst type and thickness.

Generally, the Raman peak is red shifted with increasing catalyst thickness, except the thickness of 80nm where the 1TO Raman peak is closest to the crystalline Si peak location in all prepared samples. However, the Raman peak of the sample, prepared using 100nm of Au, was the nearest to the crystalline Si peak location. Investigating the effect of the various catalyst types and thicknesses on the physical properties of SiNWs is very important. The SiNWs which were catalyzed by 80nm thickness of Sn, Al and Zn had the maximum particle sizes while the wires prepared using 100nm of Au catalyst had the largest particle size.

The Sn, Au, Al and Zn metals have different eutectic points with Si, which results significantly effect on the growth process of SiNWs. The growth process temperature affects the morphology, and in turn, the other properties of the grown SiNWs. Preparation of SiNWs at temperature higher than the eutectic point will proceed through the VLS mechanism, whereas when the temperature is less than the eutectic point, growth will be through the VSS mechanism. The preparation process of SiNWs using Sn, Au and Zn is classified as VLS, whereas that prepared using Al was classified as VSS.

Au and Zn are both effective catalysts which can be used to grow SiNWs under their growth conditions. However, Au has several advantages that make it a suitable catalyst to synthesize SiNWs. There are a relatively low temperature eutectic point of Au/Si and a high solubility in Si at the eutectic temperature. Zn is also an interesting alternative catalyst that can be used to grow SiNWs.

However, Zn metal not been used frequently to grow SiNWs due to the difficulty of preparing Zn thin films as it easily oxidizes in air . In this work, Zn thin films were deposited successfully via thermal evaporation with various thicknesses then used for

the first time as a catalyst to synthesize SiNWs via PPECVD. Zn metal was successfully used to catalyse SiNWs and produced high density NWs with interesting morphology.

The melting point and eutectic point of Zn and Au catalysts are close to the deposition temperature of 400^{o}C which produced high density growth of SiNWs via the VLS mechanism with a small average diameter. The physical properties of the SiNWs grown using Zn and Au catalysts are promising for the production of solar cells, therefore, these two elements were selected for the production of solar cells, as we shall see in the next chapter.

CHAPTER 9

FABRICATION AND CHARACTERIZATION OF SiNW-BASED SOLAR CELLS

9.1 Introduction

Silicon nanowire (SiNW) based solar cells provide interesting opportunities for the development of a new generation of thin-film Si solar cells with enhanced light trapping and increased cell performance. Thus, SiNWs have been recognized for their role in the development of third-generation solar cells, which aim to reduce the costs for device production and materials.

This Chapter reports on different SiNW-based solar cells that have been designed and investigated. In addition, details of the fabrication process of the solar cells and their properties are discussed. The devices were fabricated on an indium tin oxide-coated glass substrate by pulsed plasma-enhanced chemical vapor deposition (PPECVD). The SiNW-based solar cells were fabricated using two catalysts, Zn and Au, which produced two different NW morphologies. Both types of SiNWs were used for fabricating the devices. First, the cell was fabricated as a (p-i-n) structure, which included the p-type SiNWs catalyzed with Zn metal. The as-grown SiNWs were then covered by intrinsic and n-type amorphous Si layers.

Homojunction (p-n) SiNW solar cells were also fabricated using Zn and Au metals as catalysts for growing the NWs. This design involved doping the NWs to fabricate p-n homo-junctions within each wire. The electrical characteristics of the fabricated devices were measured using IV characterization techniques. The surface morphology and structural properties of the prepared devices were studied by scanning electron microscopy and X-ray diffraction, respectively.

9.2 Fabrication of Solar Cells Based on the p_i_n Structure

9.2.1 Device fabrication process

SiNWs were fabricated on an indium tin oxide (ITO)-coated glass substrate by PPECVD using 80nm thick Zn metal as catalyst. P-type SiNWs were produced using silane (SiH_4) and diborane (B_2H_6) gases at 400°C for 45min. Subsequently, the temperature and pressure were reduced to 225°C and 0.7torr, respectively, to create the intrinsic amorphous silicon layer (i-aSi); i-aSi was produced using undiluted silane gas for 25min and plasma power of 4W. Same synthesis conditions of Parlevliet(2008) were used to prepare 470nm of i-aSi layer.

Under the same conditions, an n-type amorphous silicon (n-aSi) layer was produced using SiH_4 combined with phosphine (PH_3) gas for 3min to deposit the n-aSi layer (Parlevliet 2008). After the p-i-n SiNW solar cell structure was fabricated, the system was purged with argon and cooled to room temperature. The samples were then removed and kept for further measurement. Figure 9.1 presents the schematic of the fabricated solar cell with the p-SiNWs/i-aSi/n-aSi structure.

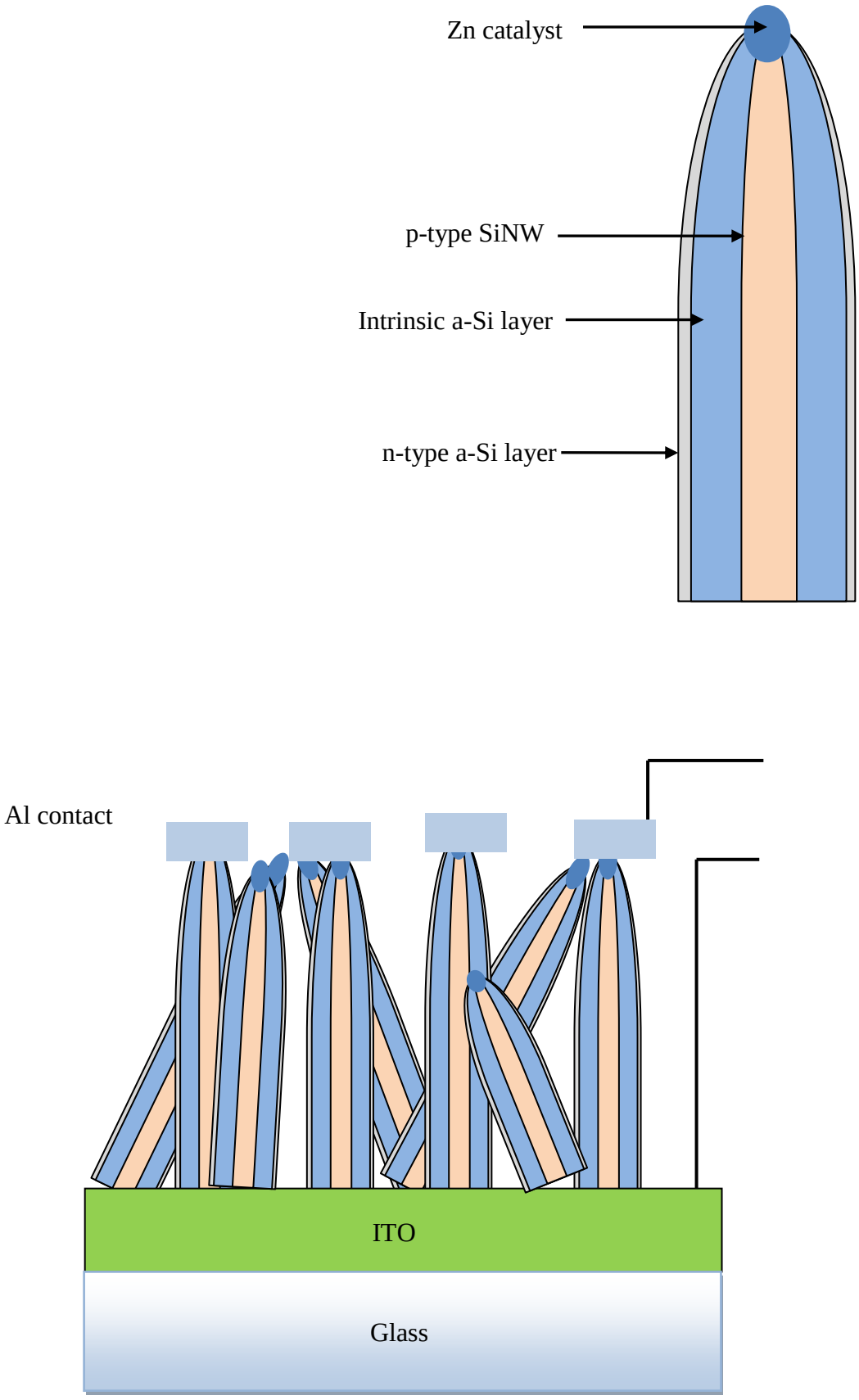

Figure 9.1: Schematic of p-i-n structure solar cell.

9.2.2 Surface Morphology

The surface morphology of the p-i-n SiNW solar cell, synthesized by PPECVD using Zn metal as catalyst exhibited high density and short wires, as shown by the FESEM images in Figure 9.2a. The device was grown vertically on the ITO substrate with a height of approximately 650nm and is shown in a cross-sectional SEM image in Figure 9.2b.

The wire diameters ranged from 350nm to 600nm, as shown in the distribution of the synthesized SiNWs in Figure 9.3. The deposition of the intrinsic and n-type amorphous silicon layers onto the as-grown p-type SiNWs increased the diameters of the wires. The 100nm gold-catalyzed prototype SiNW photovoltaic device, fabricated by the same method described in previous research, exhibited an average diameter of about 420nm (Parleviet and Jennings 2011).

The Zn–Si system exhibited lower Si concentration than with Au and Al catalysts, which have 19% and 12% concentration levels, respectively (Schemidt et al. 2009). In addition, Zn contamination was more easily removed from Si than Au contamination (Schemidt *et al.* 2009). Significant differences were observed in the surface morphology between the SiNWs catalyzed by 80nm thick Zn metal and the p-i-n structure of the SiNWs catalyzed by same thickness of Zn metal. The wires which were catalyzed by 80nm thick Zn seemed curved and the diameter ranged from 130 to 190nm. However, these differences in wire shape and diameter can be ascribed to the usage of different growth temperatures and times. Furthermore, different preparation parameters of SiNWs were used to fabricate the device like the growth temperature, time of the deposition and the a-Si layer. The variations in the parameters of the grown SiNWs led to different morphologies of the wires.

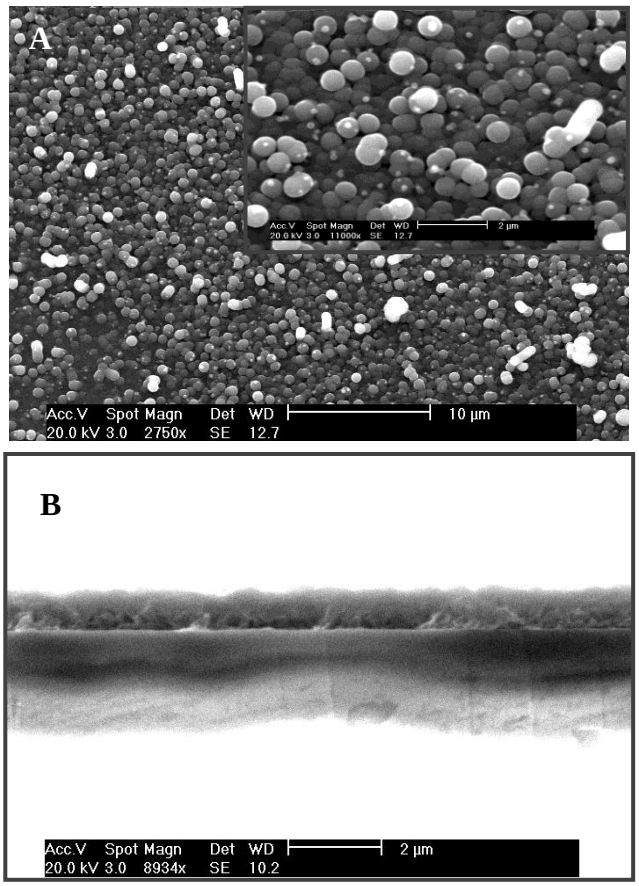

Figure 9.2: (a) FESEM image for p-SiNWs covered with intrinsic and n-type amorphous Si (b) Cross-sectional images of p-i-n SiNW solar cell.

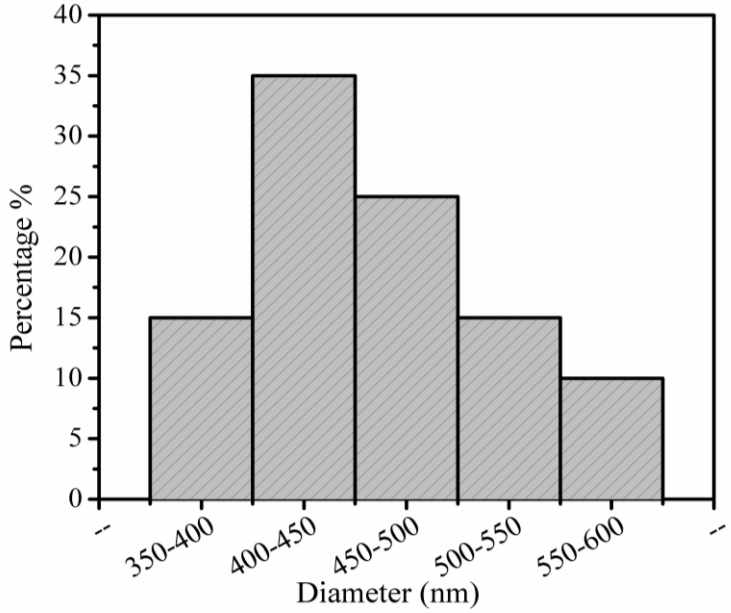

Figure 9.3: Diameter distribution of NWs in the prepared solar cell using an 80nm thickness of Zn catalyst.

9.2.3 Crystalline structure

The crystalline structure of the SiNWs in solar cell grown using an 80nm-thick Zn catalyst was investigated by XRD, as shown in Figure 9.4. The Figure illustrates that the diffraction peak of the Zn metal was observed at 36°, which corresponds to the (002) plane, indicating that Zn is the catalyst used to grow the SiNWs. The peaks observed at 34.4° and 35.8° were related to the (002) and (101) crystalline planes of zinc oxide (ZnO). The appearance of ZnO diffraction peaks in the XRD pattern indicates that some of the Zn catalyst formed an oxide during SiNW growth. The pattern for the synthesized solar cell also shows a diffraction peak at approximately 30.6°, which corresponds to the (200) plane of the ITO-coated glass substrate. The absence of diffraction peaks that correspond to SiNWs may be related to the low crystallinity of the as-grown wires, as well as to the amorphous intrinsic and n-type a-Si layers that cover the wires.

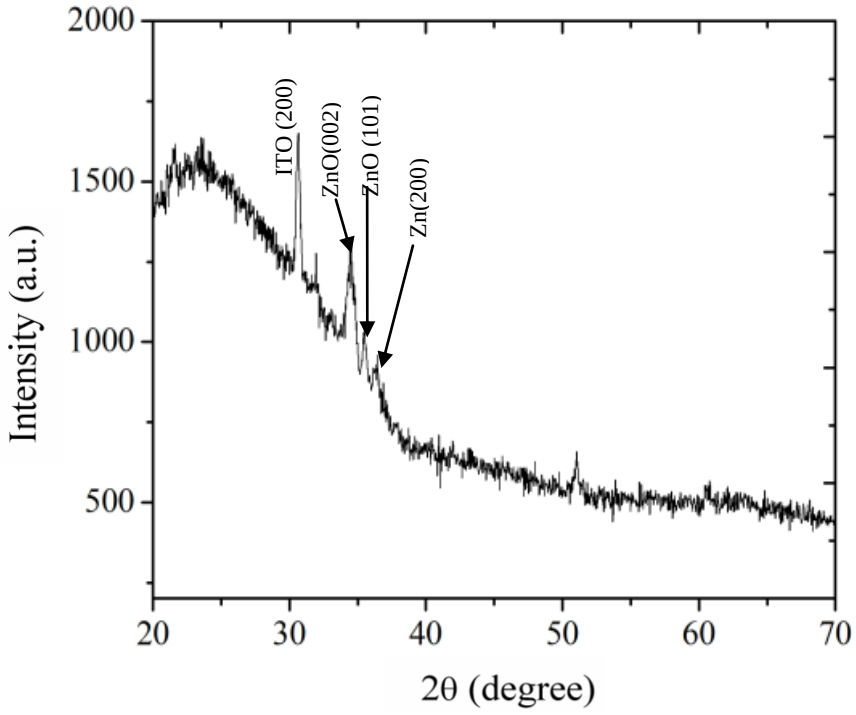

Figure 9.4: XRD patterns of SiNW prepared using Zn catalyst.

9.2.4 J–V characteristics

Figure 9.5 shows the current density–applied voltage (J–V) characteristics under AM1.5 light and dark conditions of the fabricated devices that used Zn-catalyzed p-type SiNWs covered by two layers of amorphous intrinsic and n-type Si. The Al contacts were arranged as a series of circular spots that enable light to illuminate the device around the contacts. The short-circuit current density (J_{sc}) and open-circuit voltage (V_{oc}) were derived from Figure 9.5. The efficiency (η) and fill factor (FF) of the prepared solar cells were calculated via Eq. 2.11 and Eq. 2.12, respectively. The conversion efficiency of the fabricated solar cells was measured for different samples and showed differences which could be due to the metal-semiconductor contact quality. The efficiency of the fabricated p-i-n SiNW solar cells ranged from 0.78-2.05%. Figure 9.5 (a, b and c) shown the illuminated current density- voltage plots for the fabricated cell and the solar cells characteristics are listed in Table 9.1.

Table 9.1: The parameters of the p-i-n structure fabricate solar cells.

Fabricated cells	V_{oc} (V)	J_{sc} (mA/cm^2)	FF%	η (%)
Cell A	0.50	13.3	30.8	2.05
Cell B	0.31	16.2	32.05	1.61
Cell C	0.39	6.50	30.7	0.78

Shunt resistance (R_{sh}) and series resistance (R_s) are the other parameters that can affect cell performance. R_s is caused by the bulk resistance of a semiconductor, the bulk resistance of metallic contacts, and the interconnections and contact resistance between the metallic contacts and the semiconductor. R_{sh} is caused by leakage across the junctions around the edge of a cell, in the non-peripheral regions near the crystal defects, and in the precipitates of foreign bodies in the junction region. High R_s reduces the output voltage under load, thereby decreasing FF. Low R_{sh} results in current leakages and reduces FF.

Thus, R_{sh} reduces the open-circuit voltage without changing the short-circuit current, and a high R_s reduces the short-circuit current without affecting the open-circuit voltage (Pode and Diout 2011). Ideally, R_s should be low and R_{sh} should be high because increasing the R_s of a solar cell increases the voltage drop within the cell, and a high R_{sh} increases the current flowing through the short-circuit voltage rather than the leakage path (Solanki 2011). The R_{sh} and R_s of the highest-performing p-i-n fabricated solar cells were 1.875kΩ and 556Ω, respectively. The intrinsic a-Si layer has a key function in solar cell operation. This layer increases light absorption because the amorphous silicon has a significantly higher optical absorption coefficient in the visible portion of the spectrum than crystalline silicon (Shah *et al.* 1999). The effective use of the intrinsic a-Si layer reduces surface recombination (Fujiwara and Kondo 2007). Moreover, the p-layer is exposed to the incoming radiation and tends to degrade. Therefore a crystalline structure is preferred.Yu *et al.* (2012) found that increasing the intrinsic a-Si:H layer thickness from 20nm to 80nm increases the light absorption from 40% to 80% in the 400nm to 600nm wavelength range. They also found that increasing the photocurrent density from 8.32mAcm^{-2} to 13.3mA cm^{-2} and the open-circuit voltage from 0.52V to 0.66V increases the efficiency of the solar cell from 2.2% to 4.2%.

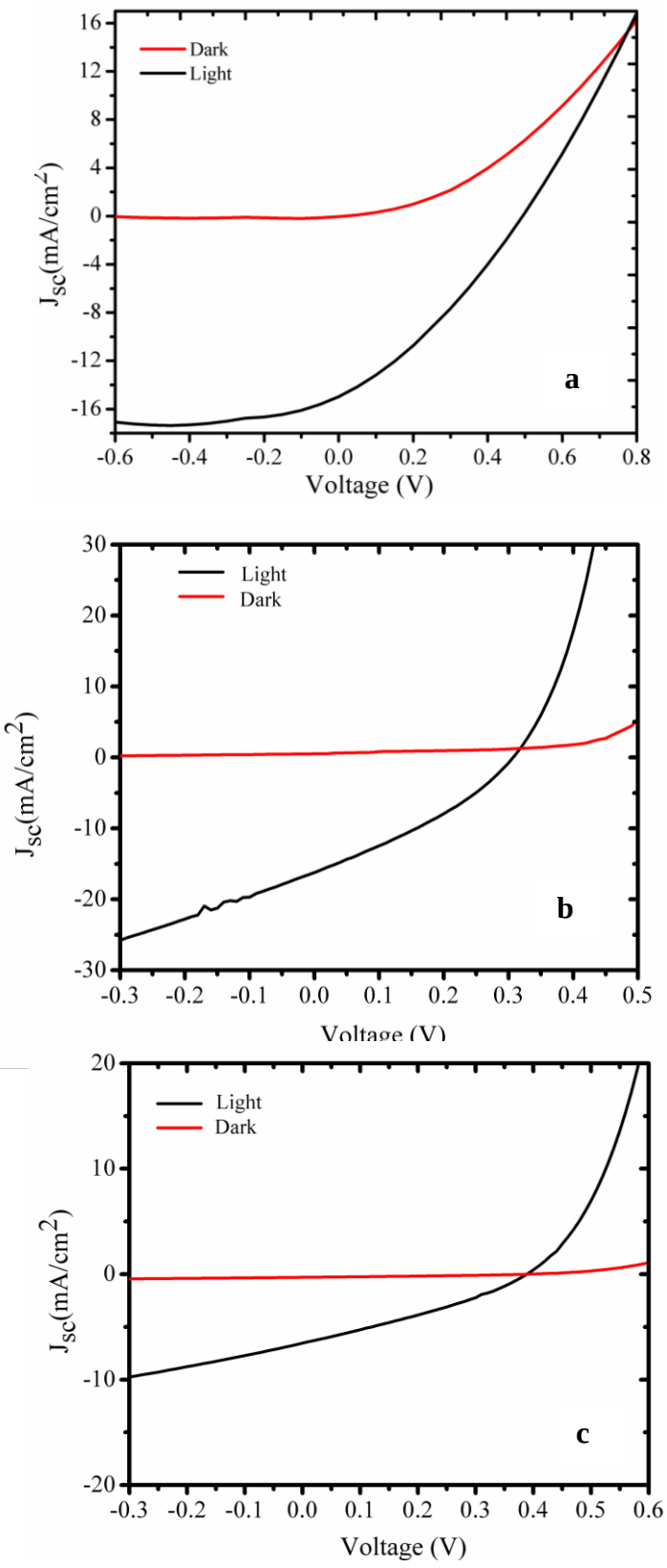

Figure 9.5: The current density–applied voltage (J–V) characteristics of the fabricated p-i-n solar cells with η of (a) 2.05%, (b) 1.61%, and (c) 0.78%.

Kempa *et al.* (2008) demonstrated that using the intrinsic layer reduces the saturation current, leading to substantial current leakage in single and tandem nanowire array p-i-n devices. Furthermore, their I–V characteristics indicate V_{oc} and J_{sc} of 0.29V and 3.5mA/cm^2, respectively, with 0.5% maximum efficiency. The p-type SiNWs/a-Si coaxial structure is required to collect effectively the photon-generated carriers from the conformal covering a-Si layer (Yu *et al.* 2010). A prototype device was fabricated by depositing intrinsic and n-type a-Si on top of the SiNWs. The device was grown on the TCO/Corning glass substrate to precipitate metallic Sn or In from the substrate by PECVD process at a temperature range of 300°C to 600°C.

Moreover, O'Donnell *et al.* (2011) used the PECVD process to grow a radial junction (i.e a junction cross of diameters of a single SiNWs) of intrinsic and n-type a-Si over p-SiNWs grown on a glass substrate using Sn as the catalyst. They observed that light trapping can be optimized by increasing the wire length from 1µm to 3µm, producing a 13mA/cm^2 current. Moreover, the device exhibited an increase in V_{oc} from 200mV to 800mV and increase in conversion efficiency from 3.4% to 5.6%. Cho *et al.* (2013) also used the PECVD method to grow p-type SiNWs catalyzed by Sn and covered by intrinsic and n-type hydrogenated a-Si on a glass substrate covered with ZnO:Al to synthesize a radial junction SiNW solar cell (pin) structure. The solar cells showed an efficiency of 4.9%, V_{oc} of 0.8V, and J_{sc} of 12.4mA/cm^2.

Meanwhile, catalyst type has a crucial function in wire morphology, crystallinity, and electrical properties. Thus, the selection of a suitable catalyst that enables the production of highly efficient SiNW-based solar cells warrants further studies. For example, using Au metal as a catalyst for SiNW growth reduces Si lifetime and limits the light conversion efficiency of the fabricated solar cell (Tsakalakos *et al.* 2007).

Parlevliet *et al.* (2011) synthesized a p-i-n structure of SiNW-based solar cells by the PPECVD method using 100nm thick Sn and Au metals as catalysts. They obtained an output efficiency of 0.03% when Sn was used, but the other solar cell that was fabricated using Au as catalyst did not respond to the light. Thus, using Zn metal to catalyze SiNWs for solar cell applications is a promising approach for fabricating more efficient devices.

Tian *et al.* (2007) obtained 3.4% efficiency when they investigated the change of doping gas precursors on the characteristics of core-shell solar cells made on a single SiNW with a p-i-n structure fabricated by CVD. Diffusing the doping atoms in a furnace is another method of creating the p-n junction. Nanowire-based p-n junctions have recently been prepared by the thermal evaporation method at approximately 900°C with 1.47% conversion efficiency (Wang *et al.* 2010).

The morphological characteristics of SiNW-based solar cells, such as wire length and diameter, can affect cell efficiency because a long NW has a low minority carrier lifetime that results in a high recombination rate. Thus, V_{oc}, J_{sc}, and η are all low for long NWs (Shiu *et al.* 2011). The SiNW devices produced in the current study exhibited efficiency comparable to that published described in the literature. The devices described in this study have not been fully optimized, as proven by the variation in efficiency. However, they demonstrated the potential of Zn-catalyzed silicon nanostructures for photovoltaic applications.

9.3 p_n Homojunction SiNW Solar Cells

9.3.1 Device fabrication process

The PPCVD method was used to fabricate SiNW homo-junction solar cells. ITO-coated glass was used as the substrate for the solar cells. Zn and Au metal thin films with thicknesses of 80 and 100nm, respectively, were used to catalyze the SiNWs. To prepare p-type SiNWs, the temperature was fixed at 400°C for 35min, and then SiH_4 and B_2H_6 gases were introduced with a flow rate of 280 sccm for 25min (as silicon and boron sources, respectively). After this phase of the deposition was completed, B_2H_6 gas flow was stopped and PH_3 gas was inserted at a flow rate of 0.7 sccm for 20min to produce the n-type SiNWs. After the fabrication process of the SiNW p-n junction, the system was purged with argon and cooled to room temperature. Figure 9.6 shows the schematic of the homojunction p-n structure of SiNW solar cells fabricated using p and n type SiNWs catalyzed with Zn and Au.

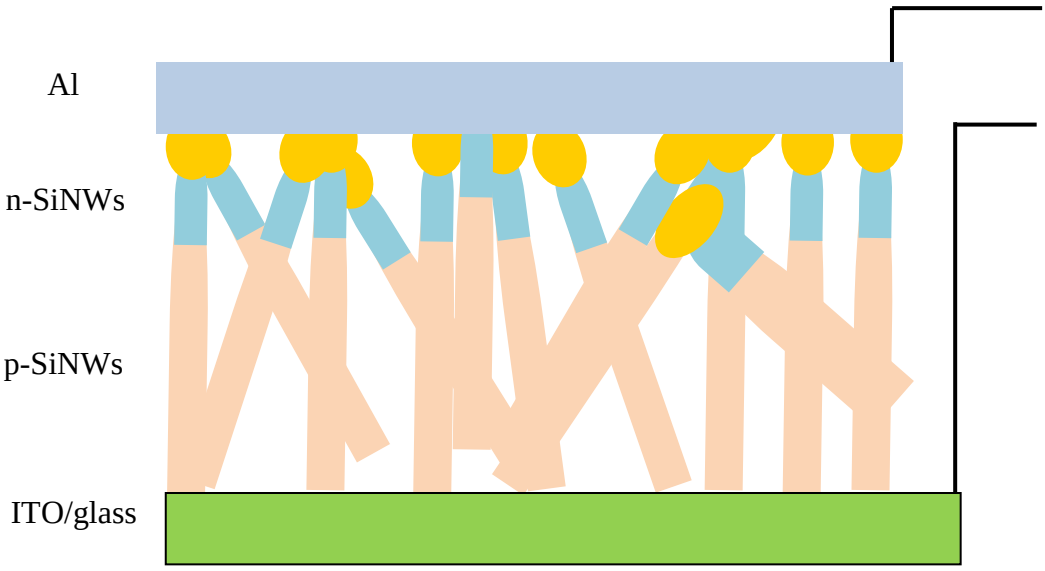

Figure 9.6: Schematic diagram of the p-n junction SiNW solar cell.

9.3.2 Surface morphology

The surface morphology of the SiNWs synthesized using 80nm-thick Zn and 100nm-thick Au catalysts are shown in Figure 9.7. Both Zn and Au produced high-density SiNWs under the growth conditions. However, the morphology of the NWs was significantly different for each catalyst. The SiNWs grown using the Zn catalyst appeared on the substrate as short curved NWs, whereas the Au catalyst produced long and homogeneous SiNWs, as shown in Figure 9.7.

The cross-sectional FESEM images of the Zn- and Au-catalyzed SiNW photovoltaic devices are shown in Figure 9.8. The wires were randomly oriented on the substrate with a straight structure. The lengths ranged from 5.6μm to 11μm for the SiNWs grown using the Au catalyst and from 0.16μm to 0.38μm using the Zn catalyst. Figure 9.9 shows the analysis of the diameter distribution of the fabricated devices using Zn and Au catalysts. The wire diameter of the SiNWs grown using the Zn catalyst ranged from 190nm to 260nm, whereas the SiNWs prepared with the Au catalyst had a wire diameter range from 140nm to 210nm. Moreover, the density of the SiNWs was calculated, to be 8 and 5NWs/μm^2 for the wires grown using Au and Zn catalysts, respectively.

The SiNWs catalyzed by Zn were thicker compared with those catalyzed by Au. According to the phase diagram, the eutectic points of the Au–Si and Zn–Si systems were 363 and 420°C, respectively, and the melting point of Zn was 420°C, whereas that of Au was 1064°C (Schemidt *et al.* 2009). The substrate was annealed at 400°C for 35min before the SiH_4 gas was inserted into the preparation chamber. Thus, the Zn particles aggregated and were larger in diameter than the Au, which in turn led to an increase in the grown wire diameters.

Parlevliet and Jennings (2011) grew SiNWs by PPECVD using a 100nm thin film thickness of Au as a catalyst, and found that the average diameter of the deposited SiNWs was 420nm. Kelzenberg *et al.* (2008) also prepared SiNWs using 100nm thin film thickness of Au catalyst and obtained diameters of prepared wires ranging from 200nm to 1.5µm. Yu *et al.* (2008) and Chung *et al. (*2000) used Zn as a catalyst to grow SiNWs by the CVD the method. The Zn catalyst was formed using SiH_4 and $ZnCl_4$/ethanol solution at 450°C. They obtained SiNWs with diameters ranging between 15 and 35nm.

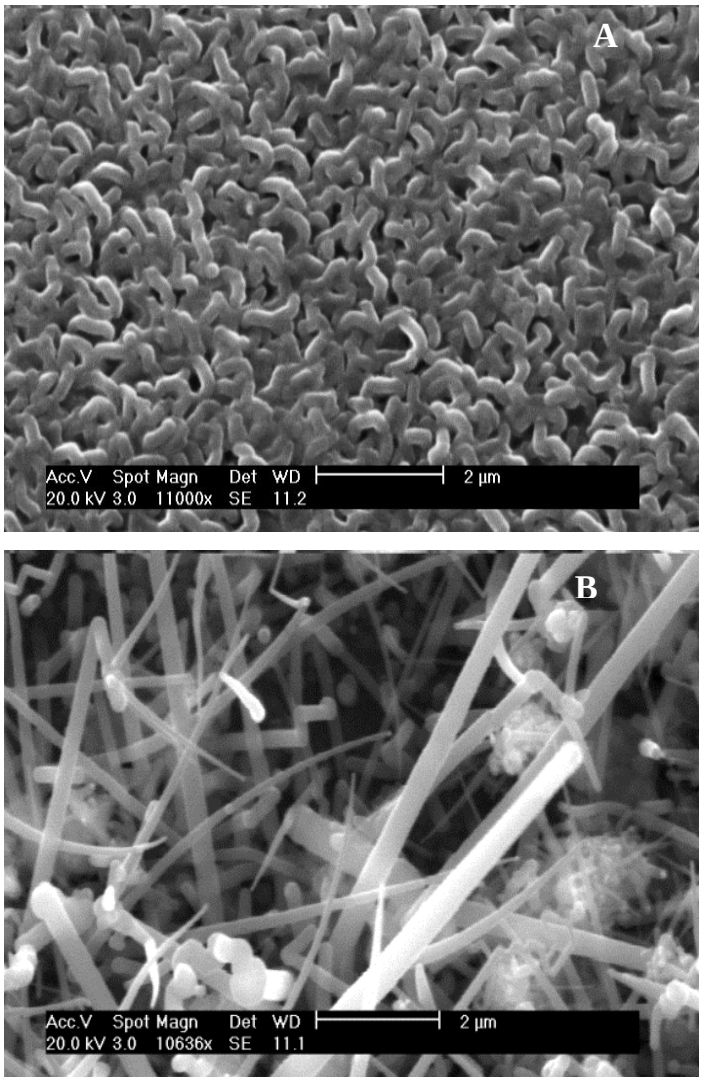

Figure 9.7: SEM images of the p-n junction SiNWs solar cells using (A) Zn and (B) Au catalysts.

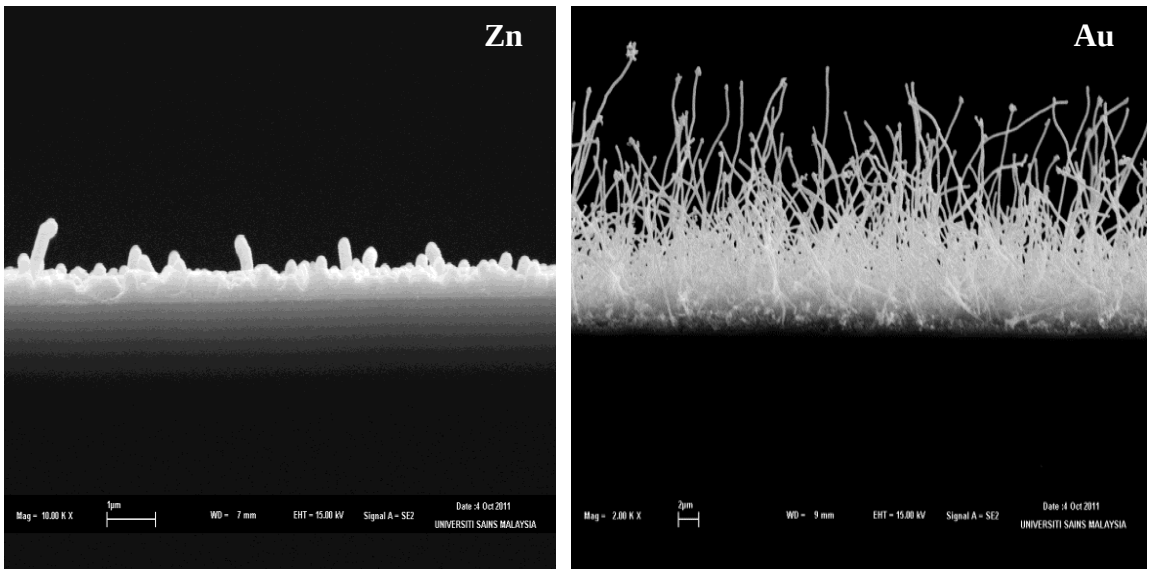

Figure 9.8: Cross sectional FESEM images of the prepared solar cells.

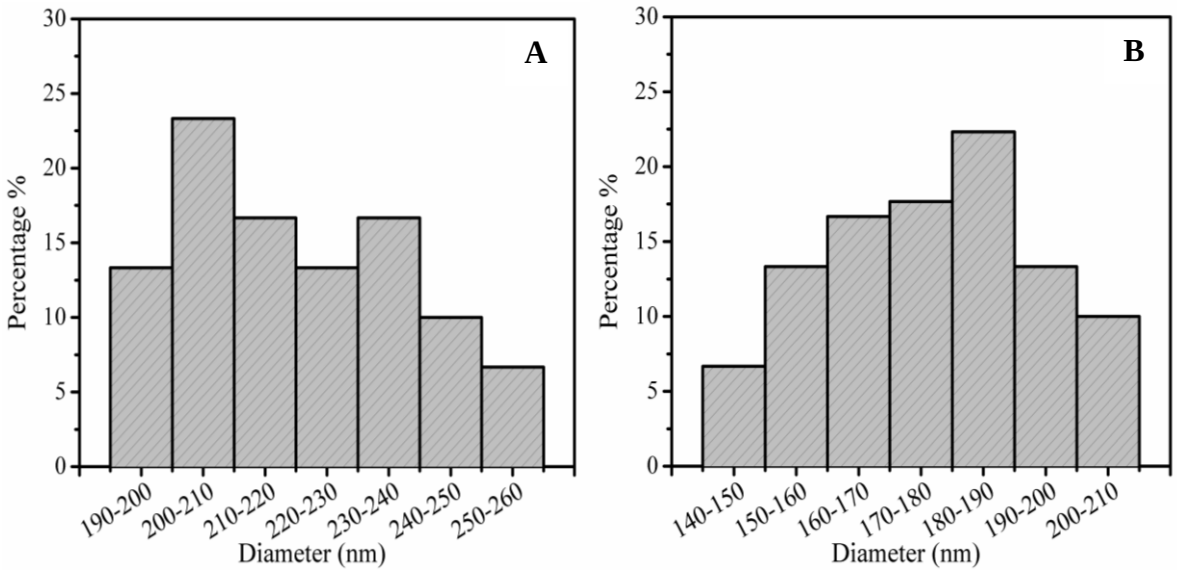

Figure 9.9: Diameter distribution of the SiNWs in the solar cells using (A) Zn and (B) Au catalysts.

9.3.3 Crystalline structure

Figure 9.10 shows the XRD patterns of the Zn and Au-catalyzed SiNW-based solar cells. The SiNWs, produced using Au as catalyst, showed diffraction peaks at 28.6, 47.6, and 56.3°, corresponding to the (111), (220) and (311) planes, respectively, of the Si diamond structure. The XRD pattern of the Zn catalyzed sample shows a high diffraction peak at 28.4^{o} corresponding to the (111) plane of the Si crystalline structure. Moreover, the diffraction peaks corresponding to the Zn and Au catalysts are apparent in Figure 9.10.

These results are in accordance with Parlevliet and Jennings (2011), Kuo *et al.* (2011) who synthesized SiNWs by PPECVD and CVD methods, respectively, using Au as catalyst, obtained highly crystallized SiNWs. The peaks due to the metal catalysts were detected because the metals were located on top of the SiNWs. Parlevliet and Jennings (2011) and Iacopi *et al.* (2007) also used Sn and Al catalysts to grow SiNWs by PPECVD and PECVD methods. They found that the grown SiNWs exhibited amorphous structure.

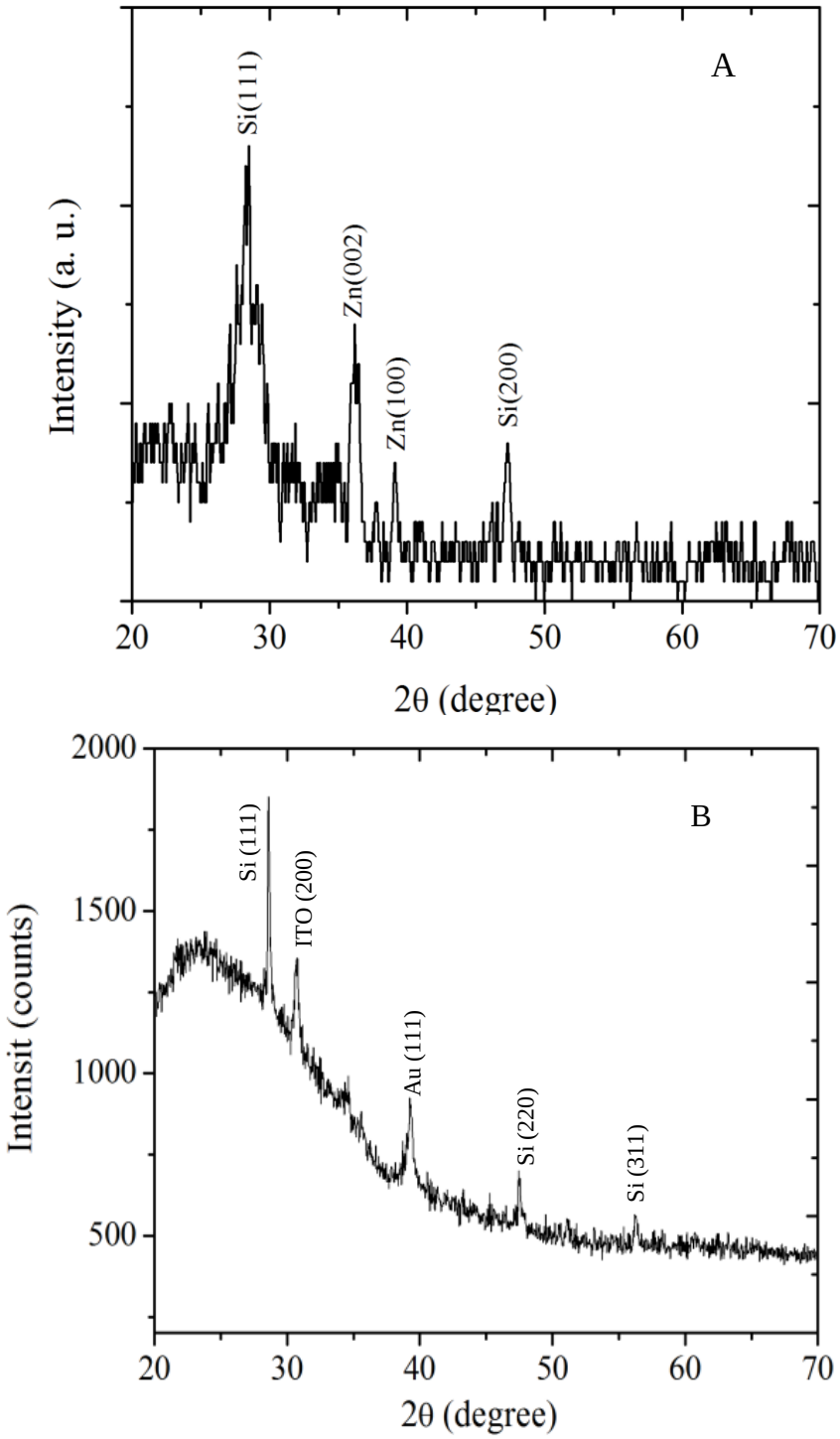

Figure 9.10: XRD patterns of SiNWs solar cells prepared using (A) Zn and (B) Au catalysts.

9.3.4 J–V characteristics

The J–V characteristics of the pn junction SiNW solar cells fabricated using the Zn and Au catalysts are shown in Figure 9.11. These devices exhibited clear photovoltaic behavior with an efficiency of 1.01 % for the p-n Zn solar cell, while the p-n Au solar cell produced an efficiency of 0.67%. In addition, J_{sc} and V_{oc} were derived from Figure 9.11, the V_{oc} of the solar cell produced by the Au-catalyzed SiNWs was significantly less than the V_{oc} of the solar cell fabricated using Zn as the catalyst. This difference may be attributed to the fact that the Au in Si acts as a recombination centre that reduces the charge carrier lifetime, which consequently reduces the open-circuit voltage (Sze 1981).

The η of the p-n junction fabricated solar cell catalyzed by Zn and Au metals were measured at several different sites on the cells' surfaces. The cell parameters are summarized in Tables 9.1 and 9.2. The calculated η showed a variation in values that could be due to the difference in metal-Si contact quality. The as-grown SiNWs had various morphological differences such as diameter, shape and NW density that could have led to significant effects on the metal-Si contact quality. The fabricated p-n junction solar cells catalyzed with Zn exhibited a range of efficiency from (1.01%-0.29%), while the efficiency of the p-n junction cells catalyzed with Au was ranged between (0.67%-0.25%). The best η value of the p-n junction solar cell fabricated using Zn was 1.01%, whereas the other one that was fabricated using the Au catalyst achieved 0.67%.

The surface morphology of the grown SiNWs like the length, diameter, and density can affect the efficiency of the solar cells due to the long NWs have a low minority carrier lifetime as a result of the high recombination rate; thus, all of the key cell parameters are low for long NWs (Shiu *et al.* 2011).

The morphology of the as-grown SiNWs catalyzed by Zn was significantly different compared with those prepared using a Au catalyst (Fig. 9.7). The former exhibited a greater diameter with shorter NW length around 0.38μm compared with those fabricated using a Au catalyst and which produced a maximum length of 11μm. Thus, increasing the wire length led to a reduction in the minority carrier lifetime.

Syu *et al.* (2012) noted that the efficiency of the fabricated SiNW/organic hybrid solar cell increased from 3.76% to 5.59% when the length of the as-grown NWs decreased from 5.59μm to 0.37μm. Furthermore, increasing the wire diameter minimized the area between the SiNWs and reduced the reflection of the incident light.

Other researchers have also studied the optical properties of SiNW arrays, and found that η increases as the NW diameter increases (Junshuai *et al.* 2009, Tsakalakos *et al.* 2007) prepared p-type SiNWs catalyzed by Au and covered with n-type a-Si to fabricate the p-n junction of a SiNW- based solar cell on a metal foil substrate by the CVD method. The authors achieved an efficiency of <0.1%.

SiNW solar cells with radial p-n junction structures were fabricated by the CVD method using Au as a catalyst on a crystalline Si substrate at 550°C (Gunawan and Guha 2009). The authors observed that the efficiency enhancement, due to the presence of the NWs, increased light trapping within the device, and the fabricated cells showed a maximum efficiency of 0.9%, V_{oc} =300mV, and J_{sc} =11mA/cm^2. The spectral efficiency showed that the surface recombination effect increased on the large surface area of the NW cells when Au was used as catalyst.

Stelzner *et al.* (2008) fabricated SiNW solar cells on Si wafers and multicrystalline Si thin films on glass, and obtained a V_{oc} of 230mV to 280mV, J_{sc} of 2mA/cm^2, and η of 0.1%. Moreover, Thomas *et al.* (2008) synthesized a solar cell based on single crystal SiNWs grown by the VLS method with a Au catalyst, and the devices exhibited V_{oc} = 0.29V, J_{sc} = 3.5mA/cm^2, and a maximum efficiency of 0.5%.

The FF of our Au-catalyzed SiNW solar cell was 59%, which was about twice of the Zn-catalyzed SiNWs solar cell value. The value of the FF was significantly higher than that reported for other SiNW solar cell devices with FFs of 20% and 40% (Kelzenberg *et al.* 2008, Ghung and Heat 2000, Sung-Wook *et al.* 2000, Kuo *et al.* 201, Iacopi 2007)

The R_s and R_{sh} of the fabricated solar cells were also calculated. The R_s of the Zn-catalyzed SiNW solar cell was 833.3Ω, which was much higher than that of the Au-catalyzed SiNW solar cell with 120.4Ω. This disparity may be attributed to the difference in the morphology of the wires such as (diameter, shape, length and density).

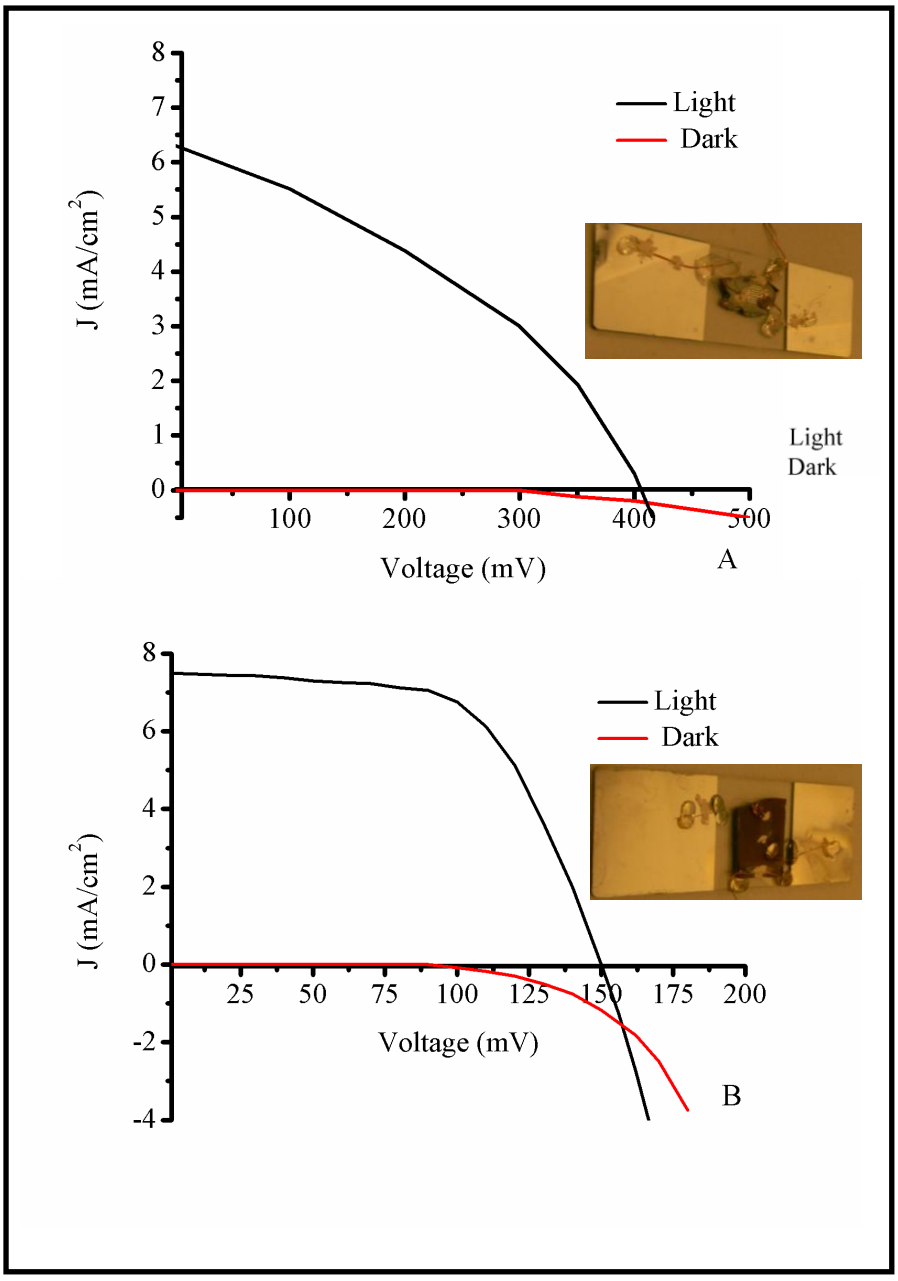

Figure 9.11: J-V characteristics under dark and illumination of the fabricated SiNWs solar cells catalyzed with (A) Zn and (B) Au catalysts.

Table 9.2: The Zn catalyzed p-n junction SiNWs solar cell parameters.

Zn catalyzed SiNWs cells	V_{oc} (V)	J_{sc} (mA/ cm^2)	F.F%	η %
Site 1	0.41	6.31	39	1.01
Site 2	0.42	7.44	28	0.9
Site 3	0.44	3.98	36	0.64
Site 4	0.34	1.67	51	0.29

Table 9.3: The Au catalyzed p-n junction SiNW solar cell parameters.

Au catalyzed SiNWs cells	V_{oc} (V)	J_{sc} (mA/ cm^2)	F.F%	η %
Site 1	0.15	7.5	59	0.67
Site 2	0.145	7.87	51	0.59
Site 3	0.140	5.55	63	0.49
Site 4	0.172	3	48	0.25

Comparison of the photovoltaic performance for SiNW solar cells catalyzed via Zn metal with p-i-n and p-n structures, showed that the performance of p-i-n solar cell structure was much better with efficiency of 2.05%, compared with the p-n junction solar cell that had a 1.01% efficiency. It is worth mentioning that both fabricated p-n and p-i-n devices show good stability with time when several tests to calculate the device characteristics have been made.

9.4 Conclusions

Several designs of solar cells based on SiNWs were fabricated by the PPECVD method at 400°C on an ITO-coated glass substrate. Zn metal was successfully used for the first time to catalyze p-type SiNWs. The as-grown wires were covered by two layers of intrinsic and n-type amorphous Si to fabricate the p-i-n solar cell structure.

FESEM images showed that the wires had diameters ranging from 350nm to 600nm. The XRD pattern at the diffraction peaks corresponding to Zn metal, ZnO, and the ITO substrate, whereas the Si peaks were absent. The fabricated solar cell exhibited an effective response to light. The maximum photocurrent density was 13.3mA/cm^2 and the open-circuit voltage was 0.5V. A promising nanowire pin junction solar cell was fabricated in this work, which had a 2.05% light conversion efficiency.

Other structures of solar cells were also fabricated based on the Au and Zn catalysts using the same preparation method. Solar cells consisting of SiNWs were catalyzed with Zn and Au metals and doped as p and n types to produce p-n homojunction cells for the first time. The surface morphology, crystalline structure, and photovoltaic properties were investigated.

The SiNWs grown with Zn and Au catalysts produced two different NW morphologies. The NWs grown using Zn as catalyst exhibited larger diameters and shorter lengths than those grown using Au as catalyst. Structural analysis showed that the SiNWs prepared using the Au catalysts were crystalline, in contrast to the nanowires grown using Zn catalyst.

The efficiency of the p-n junction solar cells catalyzed by Zn and Au were calculated in different area of the surface. The fabricated p-n solar cell based on the Zn-catalyzed SiNWs showed a higher efficiency of 1.01% compared with the Au-catalyzed SiNW pn solar cells with an efficiency of 0.67%.

The variation in the output results of the two fabricated solar cells was due to the difference in the surface morphology and the crystalline structure of the prepared SiNWs. Based on these results, it appears that the p-i-n structure is more promising and that Zn is a promising catalyst for producing SiNW solar cells. More studies are required to investigate the effect of the growth parameters on the nanowires properties and in turn, to optimize the device design. However, Zn metal is promising catalyst that can be use to grow SiNWs and fabrication solar cell devices. However, it would be useful to study the effect of other factors such as other catalyst types and temperature of preparation on the characteristics of the preparation of solar cell. Furthermore, many more samples are needed to demonstrate definite trends related to deposition conditions.

CHAPTER 10

CONCLUSIONS AND SUGGESTIONS FOR FUTURE WORK

10.1 The Research Goals

Solar power is a promising alternative for generating clean and renewable energy. Producing solar cells with high efficiency and low cost has become the goal of most third-generation PV studies. One promising approach is to use nanostructured materials that can reduce the cost and improve the efficiency of solar cells. In addition, the development of a new generation of thin film Si solar cells, with enhanced light trapping by incorporating SiNWs is also promising, and could significantly reduce the fabrication cost of solar cells. The application of SiNWs to solar cells has numerous advantages, such as improvement of the energy collection efficiency of the cell due to the shift in photoresponse of the Si closer to the maximum of the solar spectrum on the earth's surface.

The light trapping structure of SiNWs makes them good absorbers of light. This work was geared toward the preparation of high-density SiNWs and the optimization of the growth conditions and properties on low cost ITO-coated glass substrates. Under standard deposition conditions, SiNW growth can be improved using various catalysts with low eutectic points with Si. The research aims to determine whether the efficiency and stability of SiNW based thin film solar cells could be improved by synthesizing them via the PPECVD process method using various types and thicknesses of catalysts. The metals that can be used to catalyze the SiNWs include Sn, Al, Au and Zn at various thicknesses ranging from 10nm to 100nm.

The effect of catalyst type and thickness on the morphology, crystalline structure and optical properties of the grown SiNWs was investigated. The catalyst thickness was optimized and SiNW solar cells were fabricated and characterized.

10.2 Key Findings

Zn metal is a promising candidate for catalyzing SiNWs, but it is not used frequently to grow SiNWs due to the difficulty in controlling the thickness during the preparation of Zn thin films. However, Zn metal was deposited successfully in this work by vacuum thermal evaporation and used for the first time as a catalyst to grow SiNWs by PPECVD. Using the Zn catalyst produced high-density SiNWs with a very interesting morphology.

All of the catalysts used produced high-density SiNWs, and the morphological properties of the grown wires, such as diameter, length and shape, were sensitive to the type and thickness of the catalyst used. The grown SiNWs thickened and shortened for all catalyst types when the catalyst thickness increased from 10nm to 100nm, resulting in a reduction in the density of the SiNWs. According to the phase diagram of Si metal, the growth temperature is an important parameter in the preparation of SiNWs.

In this work, SiNWs were grown at 400°C, which was less than the eutectic point of Al-Si of 577°C, indicating that the growth mechanism is classified as VSS. However, the preparation mechanism of the SiNWs was under the VLS mechanism with the catalysts of Sn, Au and Zn. The crystalline structure of the grown SiNWs was studied by XRD, and this showed that the SiNWs catalyzed by Au had higher crystallinity than these the grown with other catalysts.

Moreover, no diffraction peaks related to the Si structure were observed in the XRD patterns for the SiNWs prepared with Al and Sn catalysts, indicating that the prepared wires had low crystallinity. The XRD patterns of the SiNWs prepared using 10 and 80nm thick Zn exhibited good crystallinity.

The PL spectra for all grown SiNWs catalyzed by Sn, Al, Au and Zn clearly showed a red emission band. In addition, green, blue and red emission bands were observed in the PL spectra of the NWs catalyzed with various Al thicknesses. The PL spectra of the SiNWs prepared with various Zn catalyst thicknesses showed green, blue and red emission bands in the spectra. That could be caused by the recombination of free electrons with the oxygen defect in the silicon oxide layer which coated the SiNWs.

The first-order transverse optical mode (1TO) peak location in the Raman spectrum was dependent on catalyst type and thickness, and appeared in all the prepared SiNWs with various catalysts. The 1TO Raman peak was closest to the crystalline Si peak location in all the prepared SiNWs at a catalyst thickness of 80nm, except for the SiNWs prepared using 100nm of Au metal, in which the Raman peak was closest to the crystalline Si peak.

The crystal size of the prepared SiNWs was calculated from the Raman spectra. However, although calculating the particle size is important, few studies have focused on this aspect. The shift in 1TO Raman peak position confirmed that the particle size of the grown SiNWs decreased as the thickness of Sn, Al and Zn catalysts increased. The crystal size of the grown SiNWs catalyze with 10, 20, 40, 60 and 100nm of Sn, Al and Zn metals decreased with increasing catalyst thickness. However, contrary to this trend, the 80nm thick Sn, Al and Zn catalysts showed the largest crystal size of SiNWs. For, the SiNWs synthesized with the Au catalyst the crystal size increased as the catalyst thickness increased from 10nm to 100nm.

The novel characteristics of the SiNWs were incorporated in this study to successfully fabricate SiNW-based solar cells catalyzed by Zn metal. In addition, several cell structures were designed and produced using Zn and Au catalysts to compare the influences of the morphology of the catalysts on the characteristics of the fabricated cells.

First, the p-i-n solar cell structure was fabricated as p-type SiNWs catalyzed by Zn metal and then covered by intrinsic and n-type amorphous Si layers. The fabricated solar cell exhibited high performance with 2.05% light conversion efficiency, as well as maximum photocurrent density and open-circuit voltage of 13.3mA/cm^2 and 0.5V, respectively. Other solar cells were designed for the first time as homo-junction (p-n)-structure solar cells consisting of SiNWs catalyzed with Zn and Au catalysts doped as p and n types to fabricate p-n homo-junctions within each wire. The surface morphology, structure, and photovoltaic properties were also investigated.

The two catalysts produced significantly different solar cells. The Zn catalyst produced SiNWs with larger diameters and shorter than those grown using the Au catalyst. The fabricated solar cell based on the Zn-catalyzed SiNWs revealed higher efficiency of 1.01% compared with the Au-catalyzed SiNW solar cell with an efficiency of 0.67%.

Therefore, the results showed that the p-i-n structure is more promising for fabricating solar cells and also that the Zn metal is a promising catalyst that can be used to prepare SiNW based solar cells. In this work, more studies are required to investigate the effect of the growth parameters on the NWs properties and in turn, to optimize the device design. However, Zn metal is promising catalyst that can be use to grow SiNWs and fabrication solar cell devices.

10.2 Suggestion for Future Work

The characteristics of the SiNW solar cells showed interesting performance and produce a basis to develop low cost SiNW based solar cells. However there is still much room to improve the cells performance by optimising the cell design such as the nanowire layer. This would include the doping profile with p- type SiNWs and growing denser arrays of NWs which provide better light trapping.

The growth temperature is a critical factor in determining the properties of the SiNWs. Thus, a study of the effect of different growth temperatures, substrate types, plasma frequencies and times of preparation on the morphological, structural and optical properties of SiNWs catalyzed by Sn, Al, Au and Zn metals would be very useful. The catalyst type plays an important role in the SiNW preparation. By using different metals, such as In, Ti, Cu and Ga nanowire with different electrical and optical properties can be grown.

Fabrication of hetero-junction solar cells based on SiNWs is another important topic. CdS is an n-type semiconductor with a direct band gap of 2.42 eV, thus it could be used as a window layer to fabricate a n-CdS/p-SiNWs solar cell. Finally, to increase the light absorbance of solar cells, the epitaxial layer could be modified by growing specific structures to increase the optical path length, making epitaxial cell growth on textured substrates possible.

11. References

Agarwal, A., Buddharaju, K., Lao, I.K., Singh, N., Balasubramanian, N., Kwong, D.L. (2008) *Sensor and Actuators A*, 145-146, 207-213.

Alferove, Z.I., (2002) "Nano-Optoelectronics, Concepts, Physics and Devices." In, ed. M. Grundman. Springer-Verlag Berlin Heidelberg ,New york, USA.

Al-Taay, H.F., Mahdi, M.A., Parlevliet, D., Jennings, P., (2012a) *Materials Science in Semiconductor Processing,* 16, 15-22.

Al-Taay, H.F., Mahdi, M.A., Parlevliet, D., Hassan, Z., Jennings, P. (2013b) *Physica E,* 48, 21–28.

Al-Taay, H.F., Mahdi, M.A., Parlevliet, D., Hassan, Z., Jennings, P., (2013c) *Superlattices and Microstructures,* 61, 134-145.

Arbiol,J., Kalache,B.R., Cabarrocas,P.R., Morante,J.R., Morral,A.F.(2007) *Nanotechnology*, 18, 305606-305610.

Bhattacharya, S., Banerjee, D., Adu, K.W. Samui, S. (2004) *Applied Physics Letters,* 85, 2008-2010.

Bhushan, B. (2007) *Springer Handbook of Nanotechnology, Springer Scien-ceþBusiness Media,Inc,New York,USA.*

Boj, S.C., Zardo, I., Estrade, S., Wei, L., Alet, P.J.,Cabarrocas, P.R.I., Morante, J.R.,Peiro, F.,Morral, A.F.I., Arbiol, J.(2010) *Crystal Growth and Design* , 10, 1534-1543.

Brendel, R. (2003) *Thin Film Crystalline Silicon Solar Cells physics and technology, WILEY-VCH GmbH and Co. KGaA.*

Cabarrocas, P.R.I. (2004) *Physica Status Solid C* , 1, 1115–1130.

Campbell, I.H., Fauchet, P.M. (1984) *Solid State Communications*, 58, 739-741.

Carius, R., Merdzhanova, T., Fingers, F., Klein, S.,Vetterl, O. (2003) *Journal of Material Science: Materials in Electronics*, 14, 625–628.

Chanda, A., Dasgupta, S., Bose, S., Bandyopadhyay, A.(2009) *Materials Science and Engineering C*, 29, 1144-1149.

Cho, J., O'Donnell, B., Yu, L., Kim, K.H., Ngo, I., Cabarrocas, P.R.I.(2013) *Progress in Photovoltaics: Research and Applications* 21, 77–81.

ChoiI, S.Y., Fung, W.Y., Lu, W.(2011) *Applied Physics Letters*, 98, 033108-033111.

Chong, S.K, Goh, B.T, Aspanut, Z, Muhamad, M.R, Dee, C.F, Rahman, S.A, (2011) *Thin Solid Films*, 519, 4933-4939.

Chong, S.K., Goh, B.T., Dee, C.F., Rahman, S.A.(2013) *Thin Solid Films*, 529, 53–158.

Chong, S.K, Goh, B.T., Wong, Y.Y., Nguyen, H.Q., Do, H., Aspanut, Z., Muhamad, M.R., Dee, C.F., Rahman, S.A., Ahmad, I., Agarwal, A.(2012) *Journal of Luminescence.* 132, 1345-1352.

Choy, K.L. (2003) *Progress in Materials Science*, 48, 57–170.

Chung, S.W., Yu, Y., Heath, J.R.(2000) *Applied Physics Letters*, 76, 2068-2070.

Colli, A., Hofmann, S., Fasoli, A., Ferrari, A.C., Ducati, C., Dunin-Borkowski, R.E., Robertson, J. (2006) *Applied Physics A*, 85, 247-253.

Cui, Y., Lauhon, L.J.,Gudiksen, M.S., Wang, J. Lieber, C.M.(2001) *Applied Physics Letters* , 78, 2214–2216.

Cullity, B.D. (1972) *Elements of X-Ray Diffraction*, Addison-Wesley, Reading MA., USA.

Czichos, H., Saito, T., Smith, L.(2006) *Springer handbook of materials mesurement methods*, Springer Science+Business Media, LLC, New York, USA.

Das, U., Morrison, S., Madan, A.(2003) In *NCPV and Solar Program Review Meeting*, 817-818.

David, J.(2009) *Device Applications of Silicon Nanocrystals and Nanostructures*, Ottawa,Ontario,Canada.

De Boer, W.D.A.M. D., Timmerman, D. K., Dohnalová, K. I.N., Yassievich, I.N. H., Zhang, H. W.J., Buma, W.J. T., Gregorkiewicz, T.(2010) *Nature Nanotechnology*, 5, 878-884.

Demichel, O., Oehler, F.,Calvo, V.,Noe, P.,Pauc, N.,Gentile, P.,Ferret, P.,Baron, T., Magnea, N, (2009) *Physica E*, 41, 963-965.

Falk, J.L.L., Hemesath, E.R., Lopez, F.J., Lauhon, L.J.(2007) *Journal of the American Chemical Society*, 129, 10670–10671.

Feynman, R. (1960) *Engineering and Science*, 23,22-36.

Fonash, S.J.(2010) *Solar cell Device Physics, acadmic press in an important of Elsevier, oxford, UK.*

Fujiwara, H., Kondo, M. (2007) *Journal of Applied Physics*, 101, 054516-054524.

Fukata, N., Oshima, T.,Tsurui, T., Ito, S.,Murakami, K.(2005a) *Science and Technology of Advanced Material* , 6, 628-632.

Fukuda, M. (1999) *Optical semiconductor devices, in, John Wiley & Sons, Inc, Canda.*

Gajovic, A., Gracin, D., Djerdi, I., Tomosic, N., Jusaic, K., Su, D.S. (2008) *Applied Surface Science*, 254, 2748-2754.

Garozzo, C., Magna, A.L., Mannino, G., Privitera, V., Scalese, S., Sberna, P.M., Simone, F., Puglisi, R.A. (2013) *Journal of Applied Physics*, 113, 214313-1.

Ge, D., Domnich, V.,Gogotsi, Y. (2003) *Journal of Applied Physics*, 93, 2418-2423.

Goloechen, J., Garcia, C. (1992) *Journal of Materials Science,* 27, 5247–5252.

Grassian,V.H. (2009) *Nanoscience and Nanotechnology Environmental and Health Impacts, WILEY, John Wiley and Sons Inc, Hoboken, New Jersey*.

Guo, Z., Tan, L. (2009) "Fundamentals and Applications of Nanomaterials." In: Artech House, USA.

Gunawan, O., Guha, S. (2009) *Solar Energy Materials and Solar Cells*, 93, 1388-1393.

Gusev, A.I., Rempel, A.A. (2004) *Nanocrystalline Materials*. Chippenham, U.K: Antony Rowe Ltd,.

Hamidinezhad, H., Wahab, Y., Othaman, Z., Ismail, A.K. (2011) *Applied Surface Science* , 257, 9188-9192.

Hannon, J.B., Kodambaka, S., Ross, F.M.,Tromp, R.M. (2006) *Nature*, 440, 69–71.

Hasan, M., Fazlul Huq, M., Mahmood, Z.H. (2013) *SpringerPlus*, 2, 51-159.

Heitsch, A.T., Fanfair,D.D., Tuan, H.Y., Korgel, B.A. (2008) *Journal of the American Chemical Society*, 130, 5436-5437.

He, B.B. (2009) "Two-Dimentional X-ray Diffraction " In. USA: Jon Wiley & Sons, Inc.

Ho, T.W., Hong, F.C.N. (2012) *Applied Surface Science*, 258,7989– 7996.

Hofmann, S., Ducati, C., Neill, R.J., Piscanec, S., Ferrari, A.C., Geng, J., Borkowski, R.E.D., Robertson, J. (2003) *Journal of Applied Physic* , 94, 6005-6012.

Holmes, J.D., Johnston, K.P., Doty, R.C., Korgel, B.A. (2000) *Science*, 287, 1471-1471.

Honsberg, C.B., Barnett, M., Douglas, K. (2006) *IEEE*, 2565-2568.

Huang, B.R., Yang, Y.K.,Lin, T.C.,Yang, W.L. (2012) *Solar Energy Materials & Solar Cells*, 98, 357–362.

Iacopi, F., Vereecken, P., Schaekers, M., Griffiths, M. H., Moelans, N., Blanpain, B., Richard, O., Detavernier,C. Griffiths, H. (2007) *Nanotechnology*, 18, 505307–505313.

Irene, E.A. (2005) *Electronic Materials Science, in John Wiley & Sons, Inc., Publication, New Jersey, USA.*

Ismail, R., Ahmadi, M.T., Anwar, S. (2013) Advanced Nanoelectronics, Taylor and Francis Group, LLC, USA.

Jeon, M., Kamisako, K. (2009) *Materials Letters* , 63, 777-779.

Jeon, M., Kamisako, K. (2008) *Applied Surface Science*, 254, 7703-7707.

Jeon, M., Kamisako, K. (2010) *Current Applied Physics*,10, 5191–5195.

Jha, A.R. (2010) *Solar Cell Technology and Applications*. New York, USA: CRC Press Taylor and Franeis Groupm.

Junshuai, L., Hong, L.Y. (2009) *Applied Physics Letters*, 95, 243113-243115.

Kamins, T.I., Williams, R.S., Chen, Y., Chang, Y.L., Chang, Y.A. (2000) *Applied Physics Letters.* 76, 562-564.

Kang, Z., Liu, Y., Lee, S.T. (2011) *Nanoscale*, 3, 777-791.

Ke, L.M., Mei, L., Bin, K.L., Wei, W.C., Yong, G.X., Lin. L.H. (2002) *Chinese Physics Letters*, 19, 1703-1706.

Ke, Y., Weng, X., Redwing, J.M., Eichfeld, C.M., Swisher, T.R., Mohney, S.E., Habib, Y.M. (2009) *Nano Letters*, 9, 4494-4499.

Kelzenberg, D., Daniel, B., Atwater, A.H. (2008) *Nano Letters*, 8, 710-714.

Kempa, T.J., Tian, B., Kim, D.R., Hu, J., Zheng, X., Lieber, C.M. (2008) *Nano Letters*, 8, 3456-3460.

Kumar, D., Srivastava, S.K., Singh, P.K., Husain, M., Kumar, V. (2011) S*olar Energy Materials & Solar Cells*, 95, 215–218.

Khan, M.A., Kuznia, J.N., Bhattarai, A.R., Olson, D.T. (1963) *Applied Physics Letters*, 76, 1786-1788.

Khursheed, A. (2011) *Scanning electron microscope optics and spectrometeras*: Singapore World Scintific Publishing Co. Pte. Ltd.

Kitai, A. (2011) *Principles of Solar Cells LEDs and Diodes The role of the PN junction, John Wiley and Sons, Ltd.*

Kohen, D., Cayron, C., Vito, E.D., Tileli, V., Faucherand, P., Morin, C., Brionde, A., Perraud, S. (2012) *Journal of Crystal Growth*, 341, 12-18.

Koo, H.J. (2006) *Polymer nanocomposites processing characterization and applications*. USA: In: McGraw Hill.

Kuo, C., Gau, C., Dai, B. (2011) *Solar Energy Materials and Solar Cells*, 95, 154-157.

Lee, S.T., Wang, N., Zhang, Y.F., Tang, Y.H. (1999) *Materials Research Bulletin*, 24, 36-40.

Lewis, N.S. (2007) *Science*, 315, 798-801.

Li, B.B., Yu, D.P., Zhang , S.L. (1999) *Physical Review B*, 59, 1645-1648.

Li, C., Fang, G., Sheng, S., Chen, Z.,Wang, J., Ma, S., Zhao, X. (2005) *Physica E* , 30, 169–173.

Li, C.B., Usami, K., Mizuta, H.,Oda, S. (2009) *Journal of Applied Physics*, 106, 046102-046105.

Liu, Z.Q., Xie, S.S., Zhou, W.Y., Sun, L.F., Li, Y.B., Tang, D.S., Zou, X.P., Wang, C.Y., Wang, G. (2001) *Journal of Crystal Growth*, 224, 230-234.

Liz-Marzan, L.M., Kamat, P.V. (2003) *Nanoscale materials, in, Kluwe Acadmic Publishers, USA,*.

Ma, D.D., Lee, C.S., Au, F.C.K., Tong, S.Y., Lee, S.T. (2003) *Science*, 299, 1874-1877.

Ma, Y., Zeng, X.T., Yu, T., Zhu, Y., Shen, Z.X., (2008) Materials Research Society,23, 294-297.

Mahdi, M.A., Hassan, Z., Ng, S.S., Hassan, J.J., Mohd Bakhori, S.K. (2012) *Thin Solid Films*, 520, 3477-3484.

Mahdi, M.A., Hassan,J.J., Ng,S.S., Hassan, Z. Ahmed, N.M. (2012) *Physica E*, 44, 1716-1721.

Mario, P., Ciovanni, P., Rosaria, C. (2008) *Flexible Solar Cell*: weinheim: wiley-vch verlag gmb h and co-k gaa.

Mcllroy, D.N., Alkhateeb, A., Zhang, D., Aston, D.E., Marcy, A.C., Norton, M.G. (2004) *Journal of Physics Condensed Matter*, 16, 415-440.

Megouda, N., Douani, R., Hadjersi, T., Boukherroub, R. (2009) *Journal of Luminescence* , 129, 1750-1753.

Meshram, N.P., Kumbhar, A., Dusane, R.O. (2011) *Thin Solid Films*, 519, 4609-4612.

Meshram, N.P., Kumbhar, A., Dusane, R.O. (2013) *Materials Research Bulletin*, 48, 2254–2258.

Mohammad, S.N. (2009) *Journal of Applied Physics*, 106, 104311–104322.

Mohd, A.M., Adnan, S., Hutagalung, D., Cheong, K.Y. (2009) *Journal of Nuclear and Related Technologies*, 6, 87- 90.

Molnar, W., Lugstein, A., Pongratz, P., Seyring, M., Rettenmayr, M., Borschel, C., Ronning, C., Auner, N., Bauch, C., Bertagnolli, E. (2013) *Nano Letters*, 13, 21-25.

Nakajima, K., Usami, N.(2009) *Crystal growth of Si for Solar Cells, Springer Berlin Heidelbery,* .

Nebol'sin, V.A., Shchetinin, A.A. (2003) *Inorg. Mater*, 39, 899-903.

Niu, J., Sha, J.,Yang, D. (2004) *Physica E*, 24, 278-281.

O'Donnell, B., Yu, L., Foldyna, M., Cabarrocas, B.R.I. (2011) *Journal of Non-Crystalline Solids*, 358, 2299-2302.

Pagliaro, M., Plamisano, G., Ciriminna, R. (2008) *Flexible Solar Cells*. Weinheim: WILEY-VCH Verlag Gmblt and Co. KGaA.

Pan, H., Lim, S., Poh, C., Sun,H., Wu, X., Feng, Y., Lin, J. (2005) *Nanotechnology*, 16, 417-421.

Parlevliet, D. (2008) *Silicon Nanowires For Photovoltaic Applications* PhD Thesis Murdoch University, Australia.

Parlevliet, D., Jennings, P. (2011) *Journal of Nanoparticle Research*, 13, 4431 - 4436.

Peng, K.Q., Wang, X., Li, L., Hu, Y., Lee, S.T. (2013) *Nano Today*, 8, 75-97.

Pham, V.T., Le, V.N., Chu, A.T., Pham, T.T., Tran, N.K., Pham, H.D., Pham, T., Tran, N.K., Pham, T.H. (2011) *Advances in Natural Sciences: Nanasecience and Nanotechnology* , 2, 015016-015021.

Pode, R., Diout, B. (2011) Solar Lighting, Springer Verlag London Limited,.

Poinern, G.E.J., Ng, Y.J., Fawcett, D.(2010) *Journal of Colloid and Interface Science* , 352, 259-264.

Prasad, P.N. (2004) "Nanophotonics." In: John Wiley and Sons, Inc, Hoboken, New Jersey.

Qi, J., White, J.M., Belcher, A.M., Masumoto. Y. (2003) *Chemical Physics Letters*, 372, 763-766.

Qin, Y., Li, F., Liu, D., Yan, H., Wang, J., He, D., Tileli, V., Faucherand, P., Morin, C., Brionde, A., Perraud, S. (2011) *Materials Letters*, 65, 1117-1119.

Rathi, S.J., Jariwala, B.N., Beach, J.D., Stradins, P., Taylor, P.C., Weng, X., Ke, Y., Redwing, J.M., Agarwal, S., Collins, R.T. (2011) *Journal of Physical*, 3, 23-26.

Recharsky,V.K., Zavalij,P.Y. (2003) Fundamentals of powder diffraction and structural characterization of materials, IN, Springer Science+Business Media, Inc., New York, USA,.

Reimer, L. (2008) *Transmission electron microscopy*. New York,USA: Springer Science+Business Media, LLC.

Robert, B. (2009) *Photosynthesis Research*, 101, 147-155.

Rockett, A. (2008) *The Materials Science of Semiconductors*. New York, USA: Springer Science+Business Media, LLC.

Sanders, G.D., Chang, Y.C. (1992) *Physical Review B,* 45, 9202-9213.

Sato, S., Kamimura, H., Arai, H., Kakushima, K., Ahmet, P., Ohmori, K., Yamada, K. (2010) Lwai H. 2012. *Solid State Electronic*, 54, 925-928.

Sattler, K.D. (2011) *Handbook of Nanophysics- Nanotubes and Nanowires, in, Taylor and Francis Group, LLC, USA,*.

Schell, H., Reich, S., Thomsen, C. (2005) *Physica Status Solidi B,* 242, 2474-2479.

Schemidt, V., Wittemann, J.V., Gosele, U. (2010) *Chemical Review*, 110, 361-388.

Schemidt, V., Wittemann, J.V., Senz, S., Gosele, U. (2009) *Advanced Materials*, 21, 2681–2702.

Shah, A., Torres, P., Tscharner, R., Wyrsch, N., Kepppner, H. (1999) *Science*, 285, 692-698.

Sharma, S., Sunkara, M.K. (2004) *Nanotechnology*, 15, 130-134.

Shi, F., Lin, J., Huang, Y., Zhang, J., Tang, C. (2009) *Materials Chemistry and Physics*, 118, 125-128.

Shi, W.S., Peng, H.Y., Zheng, Y.F., Wang, N., Shang, N.G., Pan, Z.W., Lee, C.S., Lee, S.T. (2000) *Advanced Materials*, 12, 1343-1345.

Shiu, S.C., Lin, S.B., Hung, S.C., Lin, C.F. (2011) *Applied Surface Science,* 257, 1829-1834.

Sivakov, V., Andra, G., Gawlik, A., Berger, A., Plentz, J., Falk, F., Christiansen, S.H. (2009) *Nano Letters*, 9, 1549-1554.

Sivakov, V., Andra, G., Gawlik, A., Berger, A., Plentz, j., Falk, F. (2009) *Nano Letters* , 9, 1549–1554.

Sivakov, V.A. Voigt, F., Berger, A., Bauer, G., Christiansen, S.H., (2010) PHYSICAL REVIEW B 82, 125446-125451

Smith, Z.R., Smith, R.I., Collins, S.D. (2013) *Electrochimica Acta,* 92, 139-147.

Solanki, C.S. (2011) *Solar Photovoltaic's Fundamentals, Technologies and Applications, Second Edition, PHI Learing Private limited, New Delhi,*.

Steiner, T. (2004) "Semiconductor Nanostructures for Optoelectronic Applications." In: Artech House, Inc. Boston , London.

Stelzner, T., Pietsch, M., Christiansen, S. (2008) *Nanotechnology*, 19, 295203-295206.

Sung-Wook, C., Jae-Young, Y., Heath, R. (2000) *Applied Physics Letters*, 76, 2068-2070.

Syu, H. J. S.C., Lin, C.F.(2012) *Solar Energy Materials and Solar Cells,* 98, 267-272.

Sze, S.M. (2007a) *Physics of Semiconductor Devices, Third Edition, WILEY Interscience, A John Wiley and Sons, INC,* USA.

Tai, G., W. Guo. (2008) *Ultrasonics Sonochemistry,* 15, 350-365.

Tarey, R.D., Raju, T.A. (1985) *Thin Solid Films*, 128, 181-189.

Thomas, J., Bozhi, T., Lieber, C.M. (2008) *Nano Letters*, 8, 3456-3460.

Tian, B.Z., Zheng, X.L., Kempa, T.J., Fang, Y., Yu, N.F., Yu, G.H. (2007) *Nature*, 449, 885-892.

Tsakalakos, L., Balch, J., Fronheiser, J., Korevaar, B.A. (2007) *Applied Physics Letters*, 91, 233117-233119.

Uesawa, N., Inasawa, S.,Tsuji, Y.,Yamaguchi, Y. (2010) *The Journal of Physical Chemistry C*, 114, 4291-4296.

Recharsky, V.K., Zavalij, P.Y. (2003) "Fundamentals of powder diffraction and structural characterization of materials." In. Springer Science+Business Media, Inc. New York, USA:

Wacaser, B.A., Dick, K.A., Zohansson, J., Borgström, M.T., Deppert, K., Samuelson, L. (2009) *Advanced Materials, 21, 153–165*

Wacaser, B.A., Reututew, M.C., Khayyat, M.M.,Wen, C., Haight, R.,Guha, S., Ross, F.M. (2009) *Nano Letters*, 9, 3296-3301.

Wagner, R.S., Ellis, W.C., Jackson, K.A., Arnold S.M. (1964) *Journal of Applied Phyics*, 35, 2993-3000.

Wang, N., Tao, B.D., Chan, Y.F., Zhang, X.Y. (2003) *Nano Letters*, 3, 475-477.

Wang, R.P., Zhou, G.W., Liu, Y.L., Pan, S.H., Zhang, H.Z., Yu, D.P., Zhang, Z. (2000), *Physical Review B*, 61, 16827-16832.

Wang, X., Pey, K.L., Yip, C.H., Fitzgerald, E.A., Antoniadis, D.A. (2010) *Journal of Applied Physics*, 108, 124303-12307.

Wang, Y., Schmidt, V., Senz, S., Gosele, U. (2006) *Nature Nanotechnology*, 1, 186-189.

Westwater, J., Gosain, D.P., Usui, S. (1998) *Phys. Stat. Sol. A*, 165, 37-42.

Wong, Y.Y., Yahaya, M., Salleh, M.M., Majlis, B.Y. (2005) *Science and Technology of AdvancedMaterials*, 6, 330-334.

Wu, X.L., Siu, G.G., Tong, S., Liu, X.N., Yan, F., Jiang, S.S., Zhang, X.K., Feng, D. (1996) *Applied Physics Letters*, 69, 523-525.

Xia, Y.N., Yany, P.D., Sun, Y.G., Wu, Y.Y., Mayers, B., Gotes, B., Yin, Y.D., Kim, F. Yan, H.Q. (2003) *Advanced Materials*, 15, 353-389.

Xie, X., Zeng, X., Yang, P., Li, H., Li, J., Zhang, X., Wang, Q. (2012) *Nanoscale Research Letters*, 7, 621-623

Xing, Y.J., Xi, Z.,Yu, D., Hang, Q.,Yan, H. (2002) *Chinese Physics Letters*, 19, 240-242

Yoo, J., Dayeh, S.A., Tang, W., Picraux, S.T. (2013) *Applied Physics Letters*, 102, 093113-1.

Yu, D.P., Bai, Z., Ding, Y., Hang, Q.L., Zhang, H.Z.,Wang, J.J., Zou, Y.H.,Qian, W. (1998) *Applied Physics Letters*, 72, 3458-3460

Yu, J.Y., Chung, S.W., Heath, J.R. (2000) *The Journal of Physi**cal** Chemistry B,* 104, 11864-11870.

Yu, L., Alet, P.J., Picardi, G., Maurin, I., Cabarrocas, P.R. (2008) *Nanotechnology*, 19, 485605–485610.

Yu, L., O'Donnell, B., Foldyna, M., Cabarrocas, P.R.I. (2012) *Nanotechnology*, 23, 194011-194016.

Yu, L., Odonnell, B., Alet, P., Boj, S., Peiro, F., Arbiol, J., Cabarrocas, P.R.I. (2009) *Nanotechnology*, 20, 225604–225609.

Yu, L., O'Donnell, B., Alet, P.J., Cabarrocas, P.R.I, (2010) *Solar Energy Materials and Solar Cells*, 94, 1855-1859.

Zhai, T., Yao, J. (2012) *John Wiley & Sons, Inc. USA*.

Zhang, B.Z., Shimizu, T., Chen, L., Senz, S.,Gösele, U. (2009a) *Advanced Materials*, 21, 4701–4705.

Zhang, J.Z. 2009. *Optical properties and spectroscopy of nanomaterials in, World Scientific Publishing Co. Pte. LTd., USA*

Zhang, Y.F., Tang, Y.H., Peng, H.Y.,Wang, N., Lee, C.S., Bello, I., Lees, S.T. (1999) *Applied Physics Letters*, 75, 1842-1844

Zhao, Q., Xu, X., Zhang, H., Chen, Y., Xu, J.,Yu, D. (2004) *Appl Phys A*, 79, 1721-1724.

Zhao, Y., Zhou, J., Zheng, L., Zhong, C.,Wrensford, L.V., Chan, K. (2013) *Materials Research Bulletin*, 48, 89–91.

Zhou, G., Zhang, Z., Yu, D. (1999) *Journal of Crystal Growth*, 197, 129-135.